X-RAY STUDY ON PLASMA OUTFLOWS FROM THE GALACTIC CENTER

by

Shinya Nakashima

Department of Physics, Graduate School of Science, Kyoto University
Kitashirakawa Oiwake-cho, Sakyo-ku, Kyoto, 606-8502, Japan
`shinya@cr.scphys.kyoto-u.ac.jp`

A dissertation submitted to the Department of Physics,
Graduate School of Science, Kyoto university
in partial fulfillment of the requirements
for the degree of Doctor of Philosophy in physics

January, 2014

Abstract

The center of our Galaxy (Galactic center; GC) has a lower activity than that of active galactic nuclei or starburst galaxies at present. The current luminosity of the central supermassive black hole, Sagittarius (Sgr) A*, is eight orders of magnitude lower than its Eddington luminosity of 10^{44} erg s^{-1}. Moreover, on-going explosive star formation is not found. However, signatures of past GC activities have been reported recently. For instance, X-ray observations have discovered fluorescent lines of neutral iron from dense molecular clouds in the GC. They are likely to be caused by reflections of past Sgr A* flares occurring 100–1000 yr ago. The luminosity of the flares are estimated as $\sim 10^{39}$ erg s^{-1}. Gamma-ray observations also revealed the giant bubbles, which suggest another Sgr A* flare or a nuclear starburst 10^6–10^7 yr ago. Such observational evidence of past GC activities is still limited, so that there is a large gap in the activity history between 10^3 and 10^6 yr ago. Our aim is to find other relics of GC activities and to clarify the history of them.

Previous X-ray observations have concentrated on the Galactic plane region. Contrastingly, we focused on the Galactic bulge region because it is less contaminated by the strong GC background emission and is more suitable to detect phenomena associated with the GC activities. We performed the survey of the off-plane region with *Suzaku*, and found the large diffuse plasma to the south and north of the GC, which are referred to as GC South and GC North, respectively.

From the spectral analysis of GC South, we discovered strong radiative recombination continua of highly ionized Si and S. We suggest that the plasma is in a recombining phase, which is not expected in the standard shock-heating scenario. Indeed, a recombining plasma (RP) model well represents the spectrum, and gave us the electron temperature of 0.5 keV, the initial ionization temperature of 1.6 keV. The recombination timescale of 10^5 yr indicates that GC South was generated $\sim 10^5$ yr ago. The spectrum suffers from strong interstellar absorption with $N_{\mathrm{H}} \sim 1 \times 10^{22}$ H cm^{-2}, which is consistent with the GC distance. Then the mass and thermal energy of the plasma reaches 3000 $M_{\odot}$ and 8×10^{51} erg, respectively, which is two orders of magnitude higher than that of a typical Galactic supernova remnant. We also investigated the spatial variation of the plasma parameters, and found that the electron temperature and density decrease as the distance from the GC becomes large, changing from 0.4 keV to 0.8 keV, and from 0.06 to 0.12 cm3, respectively. The plasma become a collisional

ionization equilibrium (CIE) state near the GC.

The spectra of GC North is represented by a CIE plasma with the electron temperature of 0.7 keV. The absorption column densities of $N_{\mathrm{H}} \sim 3 \times 10^{22}$ H cm^{-2} indicates that GC North is also located at the GC distance. The mass and thermal energy are found to be 900 $\mathrm{M}_{\odot}$ and 3×10^{51} erg, respectively. The dynamical time scale of the plasma is estimated as $\sim 10^{5}$ yr. These parameters are comparable to those of GC South.

We consider that a past GC activity $\sim 10^{5}$ yr ago generated GC South/North on the basis of large thermal energies in both the plasma and the RP in GC South.

Contents

List of Figures

List of Tables

Chapter 1

Introduction

Feeding and feedback of activities in the center of a galaxy, including a supermassive black hole (SMBH), are considered to play important roles in the context of evolution of galaxies. For its proximity, the center of our Galaxy (Galactic center; GC), is the best laboratory to investigate the details of these mechanisms. The GC has a lower activity than that of active galactic nuclei (AGNs) or starburst galaxies at present. The current luminosity of the central SMBH, Sagittarius (Sgr) A*, is eight orders of magnitude lower than its Eddington luminosity of 10^{44} erg s^{-1} (e.g., Baganoff et al. 2003). Moreover, on-going explosive star formation is not found (e.g., Longmore et al. 2013). However, evidence of past GC activities have been reported recently. For instance, X-ray observations discovered fluorescent lines of neutral iron from dense molecular clouds in the GC (Koyama et al. 1996). They are likely to be caused by reflections of past Sgr A* flares occurring 100–1000 yr ago, which should have the luminosity of 10^{39} erg s^{-1} (Ryu et al. 2013). Gamma-ray observations also revealed the giant bubbles, which suggest another Sgr A* flare or a nuclear starburst 10^{6}–10^{7} yr ago (Su et al. 2010). Such observational evidence of past GC activities is still limited, so that there is a large gap in the activity history between 10^{3} and 10^{6} yr ago. Is there any other evidence in the GC region?

In order to approach this subject, we focused on the Galactic bulge region, which is less contaminated by the strong GC background emission and is more suitable to detect phenomena associated with the GC activities. We performed the survey of this region with *Suzaku*, and found the large diffuse plasma to the south and north of the GC, possible relics of a past GC activity. In this thesis, we analyzed these emissions.

In Chapter 2, we review the specific environment of the GC and evidence of past GC activities. Performances of the instruments onboard *Suzaku* are summarized in Chapter 3. We show the GC image taken by the *Suzaku* survey and clearfy the diffuse X-ray emissions extending to the north and south of the GC in Chapter 4. Then, the results of spectral analyses on these emissions are descrived in Chapter 5 and Chapter 6. Using these results, we discuss the possible origins in Chapter 7. Finally, we described the summary and conclusion of this thesis in Chapter 8.

Throughout this thesis, we mainly use the Galactic coordinates, where the horizontal and vertical axes are the Galactic longitude (l) and latitude (b), respectively. We refer to the positive directions of l and b as east and north, respectively. We adopt the distance to the GC to be 8 kpc. Errors are quoted at the 90% confidence level otherwise noted.

Chapter 2

Review

In this chapter, we review the specific environment of the GC including the central SMBH, and evidence of past GC activities to clarify the subject of this thesis.

Contents

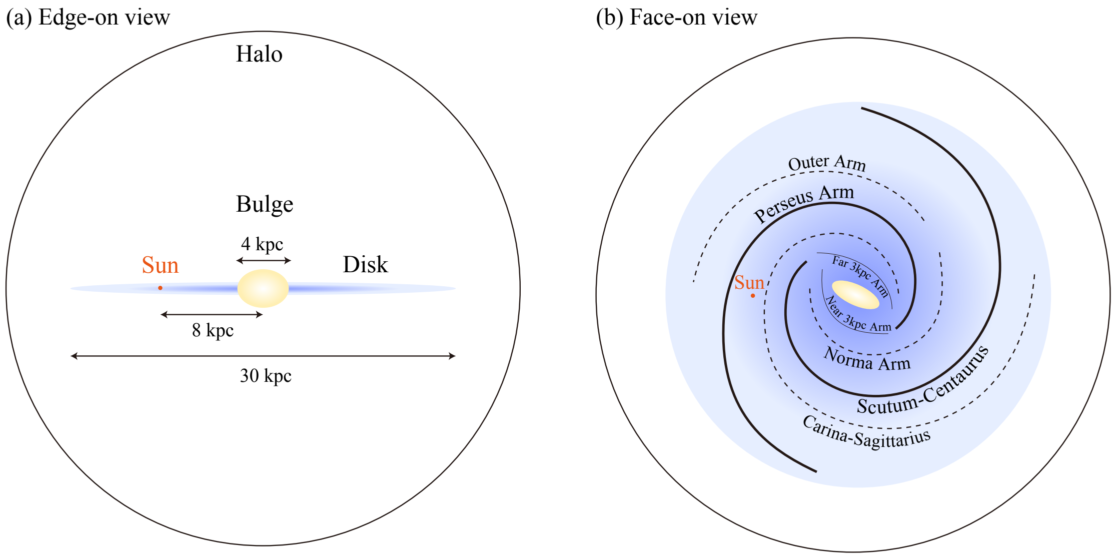

Figure 2.1. Schematic illustration showing the structure of the Galaxy in (a) the edge-on view and (b) the face-on view.

2.1 Overview of the Milky Way Galaxy

The Milky Way Galaxy (the Galaxy), harboring our solar system, is a typical barred spiral galaxy belonging to the Local Group, where three large (the Galaxy, M31 and M33) and over 30 small galaxies are contained. Since the solar system is situated within the Galaxy, we are not able to directly see its overall morphology. Multi-wavelength observations, especially using the 21 cm and ^{12}CO line, enable us to know the dynamics of the interstellar medium (ISM) and the structure of the Galaxy.

As shown in Figure 2.1(a), the Galaxy consists of the disk, the bulge, and the halo. The solar system is located at the 8 kpc distance from the GC and 40 pc above the plane of the disk. The disk is the main component of the Galaxy containing the most of Population I stars. It has the 30 kpc diameter and the 1 kpc thickness with the mass of $\sim 10^{11}\ M_{\odot}$. The bulge is the spheroid located at the center of the disk with the major and minor axes of 4 kpc and 3 kpc, respectively. In the face-on view (Figure 2.1(b)), the bulge is flattened like a bar with the 25°orientation angle to the line of sight. The mass of the bulge is estimated to be $\sim 10^{10}\ M_{\odot}$. The disk and the bulge are surrounded by the ellipsoidal halo with the radius of 20 kpc. Its mass is found to be $\sim 4 \times 10^{11}\ M_{\odot}$ from the rotation curve (therefore including dark matter). Population II stars dominate in the bulge and halo.

Figure 2.1(b) shows the spiral arms in the disk, which have been traced by doppler shifts of the emission lines from H I and ^{12}CO. Figure 2.2 shows the l-v diagram of the ^{12}CO line

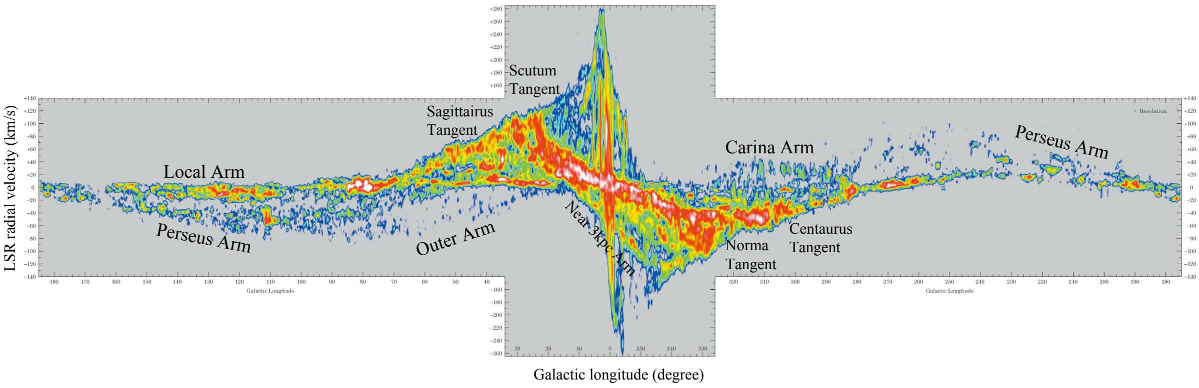

Figure 2.2. Longitude-velocity map of the ^{12}CO emission. The horizontal and vertical axes are the Galactic longitude and the local standard of rest (LSR) radial velocity, respectively. The center of the figure is $(l,\, v) = (0.^\circ 0,\ 0.0\ \mathrm{km\ s^{-1}})$ The upper and lower half of the panel indicates positive and negative LSR velocities, respectively. (From Dame et al. 2001.)

survey covering the entire Galactic plane. Its symmetrical shape to the center of the image ($l = 0,\ v = 0$) reflects the rotation of the Galaxy. The arc structures correspond to spiral arms, and are named after the constellations. The arms in the first and third quadrants and the second and fourth quadrants are within and beyond the solar circle, respectively. The GC direction shows very large velocity dispersion, which suggests distinctive condition in the GC.

2.2 Galactic Center Environment

2.2.1 Characteristics of the interstellar medium

The ISM in the central hundreds parsecs of the Galaxy has different physical characteristics from that in the disk. Table 2.1 shows typical parameters of the ISM in the GC and the disk. In general, the GC ISM is dense and high temperature. The H I-to-H_2 ratio in the GC is also extremely smaller (~0.05) than that in the disk (~1) (Ferrière et al. 2007).

The predominant medium in the GC is dense molecular clouds (MCs), the so-called central molecular zone (CMZ; see Morris & Serabyn 1996 for a review), which contains ~5% mass of the total MCs in the Galaxy. Its temperature and density reach 70 K and 10^4 cm^{-3}, respectively. Such a extremely warm and dense molecular is hardly seen in the disk except for molecular cores. Moreover, the velocity dispersion of the CMZ is 15–50 km s^{-1}. The large turbulent pressure might be in equilibrium with those of the magnetic fields and the hot plasmas.

Table 2.1. Typical ISM characteristics in the Galactic center and the Disk

	Molecular (H_2)		Neutral (H I)	Warm (H II)	Hot (H II)
			Galactic center		
	(Dense)	(Diffuse)			
T (K)	70	150	100	10^4	10^7–10^8
n (cm^{-3})	10^4	10^2	10	10	0.1
M ($M_\odot$)	5×10^7	10^7	10^6	10^5	10^3
			Disk region		
T (K)	10		100	10^4	10^7
n (cm^{-3})	10^2		0.3	0.1	10^{-3}
M ($M_\odot$)	10^9		10^9	10^8	10^7

Notes:
Molecular: Oka et al. (1998); Tsuboi et al. (1999) for the GC. Dame (1993) for the disk.
Neutral: Ferrière et al. (2007) for the GC. Rohlfs & Kreitschmann (1987) for the disk.
Warm: Roy (2013) for the GC. Haffner et al. (2009) for the disk. Not including $\mathrm{H_{II}}$ regions.
Hot: Uchiyama et al. (2013) for the GC. Snowden et al. (1997) for the disk. Not including SNRs

Another distinctive component in the GC is the very hot plasma. Its mass is very small ($\sim 10^3\ M_\odot$) but its thermal pressure is comparable to that of the CMZ, and thus it has a considerable effect on the GC environment. Details of its nature are described in Section 2.2.2.

The spatial distribution of the ISM in the GC region was modeled by Ferrière et al. (2007). Figure 2.3 shows the density profile along the Galactic latitude at just the GC. The cold matters (H_2 and H I) are highly concentrated within 100 pc from the Galactic plane while the ionized medium is sparse and extended.

2.2.2 X-ray emitting diffuse plasma

Early X-ray observations detected not only a number of luminous X-ray binaries but also unresolved emissions on the Galactic plane. From the *EXOSAT* observations, Warwick et al. (1985) reported that this unresolved emission extends within $|l| < 40^\circ$, and thus referred to it as the Galactic ridge X-ray emission (GRXE). Koyama et al. (1986) discovered the intense 6.7 keV (Fe XXV) line from the GRXE spectrum, and suggested the origin of an optically-thin plasma with the temperature of 5–10 keV. Subsequently, Koyama et al. (1989) found that the 6.7 keV line is smoothly distributed within $|l| < 60^\circ$ and has a strong peak at $|l| < 1^\circ$. The peak intensity is 10 times larger than that of the outer region. This intense

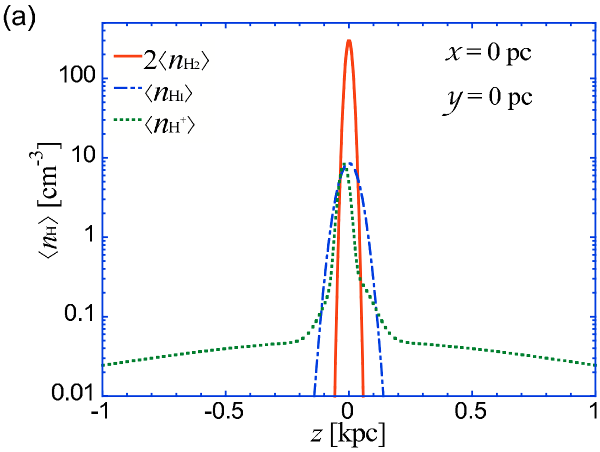

Figure 2.3. Density profile of the ISM along the Galactic latitude at just the GC. The red, blue, and green lines show the molecular, neutral, and ionized phase. (From Ferrière et al. 2007.)

GC emission is referred to as the Galactic center X-ray emission (GCXE) to distinguish it from the GRXE.

An extensive study on the GCXE was carried out by *ASCA*, which is the first satellite using X-ray CCDs with the imaging capability up to 10 keV. As shown in Figure 2.4(a), *ASCA* resolved the ∼6.7 keV line seen in the *Tenma* and *Ginga* spectrum into the composition of three lines: 6.4 keV (Fe I), 6.7 keV (Fe XXV), and 6.9 keV (Fe XXVI) lines (Koyama et al. 1996). The 6.7 keV and 6.9 keV lines likely come from a thermal plasma with $kT = 7$ keV as suggested in the previous studies, whereas the 6.4 keV line should be emitted from neutral cold matters by another mechanism. The nature and origin of the 6.4 keV line is discussed in Section 2.3.3.

As shown in Figure 2.5(a), the 6.7 keV emission is smoothly distributed over the hundreds parsecs of the GC. If it is of a diffuse plasma origin, its density and total thermal energy is found to be 0.05 cm^{-3} and 10^{53} erg s^{-1}, respectively (Uchiyama et al. 2013). The sound velocity of the 7 keV plasma ($\sim$ 1500 km s^{-1}) exceeds the escape velocity of the GC region, so that the plasma leaves from the GC in $\sim 2 \times 10^4$ yr. Therefore, one supernova (SN) per 200 yr (equivalent to 10^{41} erg s^{-1}) is required to sustain the plasma. However, this SN rate is unreasonably high because one SN per 1000 yr is expected in this region scaling the Galactic SN rate (one SN per 50 yr) by the mass ratio (5%). This is the most serious problem for the GCXE.

In order to solve this energy problem, other scenarios have been proposed. One is the superposition of unresolved point sources consisting of intermediate polars or active stars, which emit the 6.4 keV, 6.7 keV, and 6.9 keV lines. Indeed, Revnivtsev et al. (2009) argued that more than 80% of the 6–7 keV emission in the bulge region ($l = 0\overset{\circ}{.}0$, $b = -1\overset{\circ}{.}4$) is resolved into discrete sources by *Chandra*. However, *Chandra* resolved only 30% of the total flux into discrete sources near Sgr A* (Muno et al. 2004). Moreover, Nishiyama et al. (2013) compared the spatial distribution between the X-ray surface brightness and stellar mass density, and found ∼50% discrepancy between them at the GC.

Another scenario, the origin of charge exchange recombination, was claimed by Tanaka et al. (2000). In this scenario, interaction between neutral hydrogen and Fe XXV or Fe XXVI in cosmic-rays causes electron capture into a excited state of Fe ions, and then de-excitation of this electron emits the 6.7 keV or 6.9 keV lines. The 6.7 keV line mainly consists of the forbidden line (6636 eV) and the resonance line (6700 eV), which are predominantly due to recombination and collisional excitation, respectively. In a collisional ionization equilibrium plasma, the resonance line dominates and hence center energy of the Fe XXV line is ∼6700 eV. If the charge exchange recombination is the case, the forbidden line is enhanced and center energy of the Fe XXV line is close to the 6636 eV. Using the *Suzaku* high-quality spectrum (Figure 2.4(b)), Koyama et al. (2007b) found a centroid of the 6.7 keV line is 6680 ± 1 eV, which suggests that the 6.7 keV line is not due to charge exchange but collisional excitation. Therefore, the charge exchange scenario is no favored. The origin of the 7 keV thermal plasma is still an open question.

In addition, K-shell emission lines from highly-ionized Si, S, Ar, and Ca are also detected in the GCXE spectrum (see Figure 2.4(a)), which are typical features of the thin thermal plasma with $kT \sim 1$ keV. As shown in Figure 2.5(b), the spatial distribution of the S line is patchy in contrast to the 7 keV plasma. Some of them are X-ray SNRs reported by many authors (Koyama et al. 2007a; Nobukawa et al. 2008; Tsuru et al. 2009; Mori et al. 2009; Sawada et al. 2009; Nakashima et al. 2010; Ohnishi et al. 2011). The mean density and total thermal energy of the 1 keV plasma are 0.07 cm^{-3} and 10^{52} erg s^{-1}, respectively. Since the dynamical timescale of the1 keV plasma is $\sim 10^5$ yr, one SN per 10^4 yr is required to sustain the plasma. It is consistent with the expected SN rate in this region. The total flux and luminosity in the 2–10 keV band from the 1° square field are $\sim 10^{-9}$ erg s^{-1} cm^{-2} and $\sim 10^{37}$ erg s^{-1}, respectively.

2.2.3 Magnetic field

As shown in Figure 2.6, radio continuum observations have revealed numerous filamentary structures in the GC region (see Morris 2007 for a review). Their radio polarization indicates that the emissions are synchrotron radiation from the magnetic flux tube filled with non-thermal electrons. In addition, the position angles of the polarization shows that

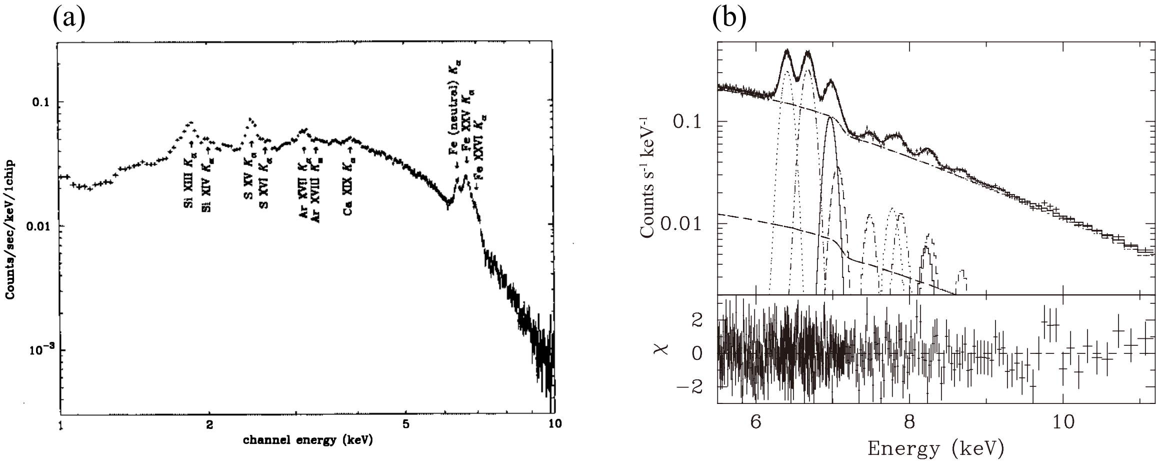

Figure 2.4. (a) *ASCA* spectrum of GCXE in the 1–10 keV band. (From Koyama et al. 1996.) (b) *Suzaku* spectrum of GCXE in the 5.5–12 keV band with the phenomenological model (Gaussians plus power-law functions). (From Koyama et al. 2007b.)

the magnetic filed along the filaments. Most of the filaments elongated from north to south with < 0.5 pc in width and tens of parsecs in length. Therefore, globally poloidal magnetic fields in the GC is suggested.

The most outstanding feature located at $l = 0\overset{\circ}{.}15$ is referred to as the "Arc". The Arc seemed to interact with nearby molecular cloud, whose density is $\sim 10^3$ cm^{-3} with the velocity dispersion of $\sim$15 km s^{-1} (Yusef-Zadeh & Morris 1987). The Arc shows almost invariant curvature and absence of distortion against the large turbulent pressure of the cloud (10^{-8} erg cm^{-3}). Therefore, Yusef-Zadeh & Morris (1987) argued that the magnetic filed of the Arc should be $\gtrsim$1 mG to overcome the turbulent pressure. The cooling time of the synchrotron radiation is described as

$$t_{\rm sync} = 1.3 \times 10^4 \left(\frac{E_{\rm e}}{1~{\rm GeV}}\right)^{-1} \left(\frac{B}{1~{\rm mG}}\right)^{-2}~{\rm yr}, \tag{2.1}$$

where $E_{\rm e}$ and B is the electron energy and the magnetic flux density. Assuming the electrons diffuse along the magnetic field with Alfvèn speed of

$$v_A = 2200 \left(\frac{B}{1~{\rm mG}}\right) \left(\frac{n_{\rm e}}{1~{\rm cm}^{-3}}\right)^{-0.5}~{\rm km~s}^{-1}, \tag{2.2}$$

where $n_{\rm e}$ is the electron density, 1 GeV electrons can travel $v_A t_{\rm sync} \sim 30$ pc before losing their energy. It is the same order of magnitude as the observed Arc length (60 pc).

LaRosa et al. (2005) found a diffuse synchrotron emission without filamentary structures in the low frequency band (74 MHz). Assuming equipartition of the energy between the

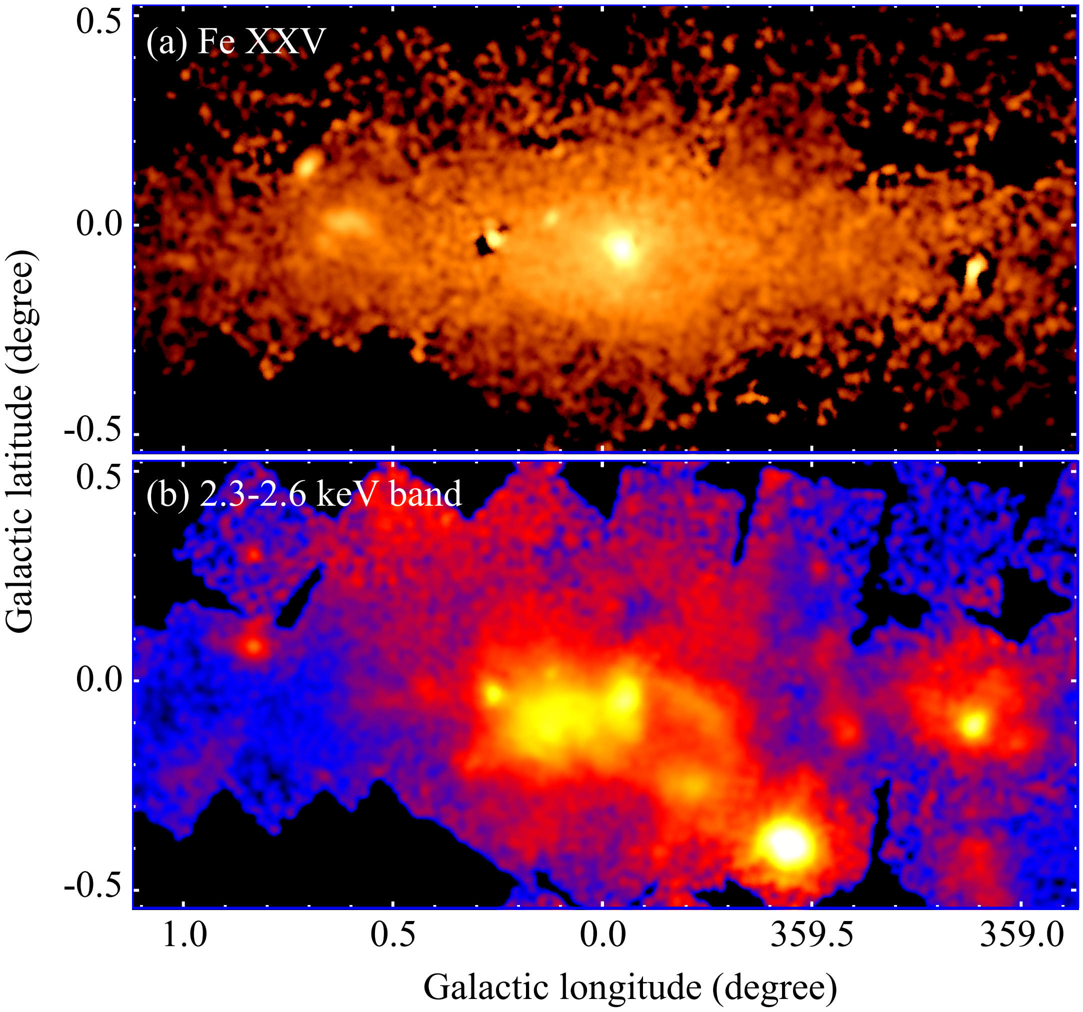

Figure 2.5. X-ray images in the 2° × 1° field taken by *Suzaku*. (a) Continuum subtracted 6.7 keV line (Fe XXV) image. (b) 2.3-2.6 keV, including S XIII line, band image.

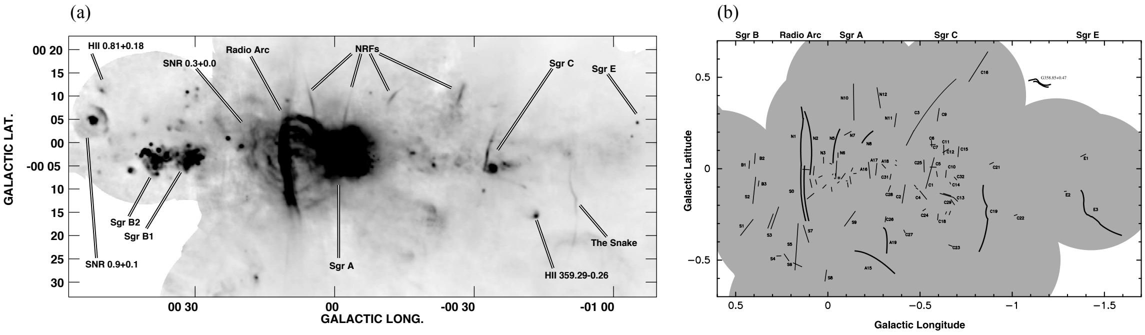

Figure 2.6. (a) Radio image of the 2° × 1° GC region in the 20 cm band. Significant features are labeled. (b) Schematic diagram of the distribution of non-thermal filaments in the GC. (Both from Yusef-Zadeh et al. 2004.)

magnetic filed and the cosmic-rays, the authors obtained the magnetic filed of 6 μG, which is extremely lower than that obtained from the non-thermal filament. On the other hand, Crocker et al. (2010) combined the gamma-ray upper limit taken by *EGRET* with the low frequency radio data, and derived the lower limit of 50 μG for the inner 400 pc region. They argued that the GC magnetic filed is not in equipartition.

Not only the poloidal structures seen in the non-thermal filaments but also toroidal configuration is shown in near-infrared polarization (Nishiyama et al. 2010). Such toroidal magnetic fields are also found in the dense molecular clouds (Novak et al. 2003). Therefore, global configuration of the magnetic fields are under debate.

2.2.4 Star formation in the GC

From the observations of massive stars, Immer et al. (2012) estimated the star formation rate (SFR) in the CMZ (450 pc region) to be 0.08 $M_\odot$ yr^{-1} over the last 10^6 yr, which is ∼8% of the SFR in the entire Galaxy (∼1 $M_\odot$ yr^{-1}, Robitaille & Whitney 2010) and is consistent with the mass ratio of the CMZ to the entire Galaxy. This value is consistent with the mass ratio of the CMZ to the molecular gas in the entire Galaxy. However, Longmore et al. (2013) claimed that this SFR is too small considering the correlation between density of MC and an SFR; much higher SFR is expected in the GC because the CMZ is denser than the disk (see Section 2.2.1). One possible explanation is that the large turbulent pressure of the CMZ suppresses the star formation (Longmore et al. 2013).

In the inner 30 pc of the GC, there are three young star clusters, the so-called central, Quintuplet, and Arches clusters, whose total mass is 5×10^4 $M_\odot$. Since the age of these clusters are in the range of 2–7 Myr, star formation late at that time is estimated to be

5×10^4 $M_\odot$/5 Myr = 0.01 $M_\odot$ yr^{-1} (Figer et al. 2004). The authors also investigated the stellar luminosity function including intermediate and old stars in the central 30 pc of the Galaxy, and found that continuos star formation rate of 0.02 $M_\odot$ yr^{-1} between 10^7 and 10^{10} year ago represents the obtained luminosity function.

In contrast to the above continuous star formation rate, Yusef-Zadeh et al. (2009) investigated various SFR indicators in the GC, and reported that the SFR 10^5–10^7 yr ago is ∼0.1 $M_\odot$ yr^{-1} while it decreases to ∼0.01 $M_\odot$ yr^{-1} in the last 10^5 yr. Yasuda et al. (2008) also claimed that the current star-formation activity is lower than in past based on the infrared spectroscopy. Therefore, the star formation history in the GC is still controversial.

2.3 Supermassive Black Hole Sagittarius A*

2.3.1 Evidence for the central supermassive black hole

Based on the discovery of quasars in the 1960s, it is predicted that nearby galaxies, including the Galaxy, have SMBHs in their center (Lynden-Bell 1969; Lynden-Bell & Rees 1971). Radio observations detected the compact (sub-arcsecond) and high brightness temperature (10^7 K) source at the dynamical center of the Galaxy (Balick & Brown 1974). Such a source is not seen in other part of the Galaxy. This peculiar object was suspected to be a SMBH in our Galaxy, and has been referred to as Sgr A* (Brown 1982). However, there is little signature of the SMBH in other-wavelength emissions. (see Section 2.3.2).

Gas and stellar dynamics near Sgr A* is a powerful tool to identify the Galactic SMBH. The most plausible evidence of the central SMBH is provided by the measurements of the proper motions for the "S-stars" in the central cluster, which are located within 0.5″ of Sgr A* (Figure 2.7(a); Ghez et al. 2005). High-resolution near-infrared observations with laser guide-star adaptive optics revealed the precise Kepler orbits of S-stars as shown in Figure 2.7(b) (Schödel et al. 2002; Ghez et al. 2005). In order to explain the observed orbits, there should be a mass of ∼4×10^6 $M_\odot$ within 0.01 pc at a distance of 8 kpc from the Sun (Ghez et al. 2008).

2.3.2 Emissions from Sgr A*

Radio

After the discovery of Sgr A*, many radio observations have been performed. The GHz band flux of Sgr A* is variable by a few tens of percent on the time scales of years to days, and the slope of its spectrum ($S_\nu \propto \nu^\alpha$) also varies between $\alpha = 0.1$ and 0.6 (Brown &

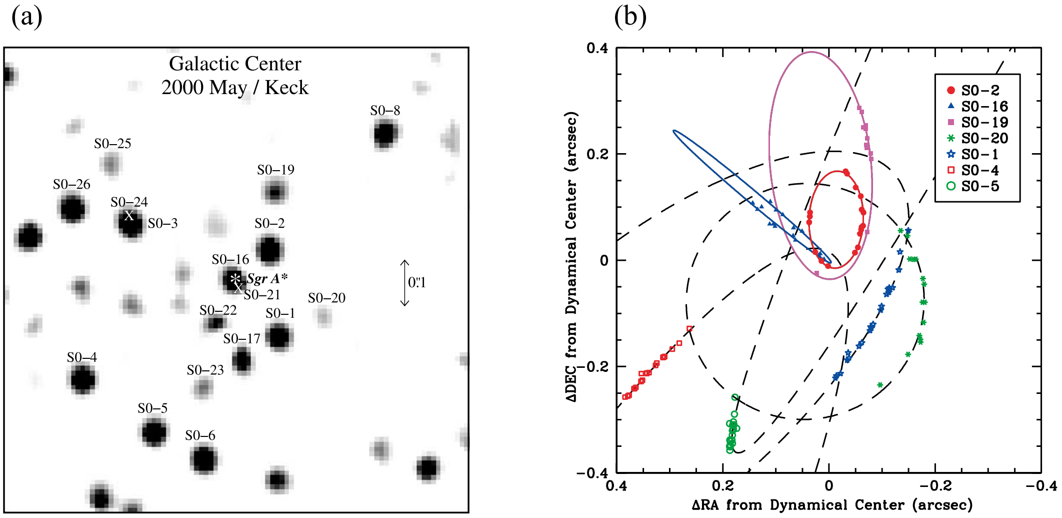

Figure 2.7. (a) Central $1'' \times 1''$ K-band (2.2 μm) image taken by the W. M Keck I 10 m telescope. Detected S-stars and the position of Sgr A* are lebeld. (b) Astrometric positions and orbital fits of S-stars as a result of eight-year observations between 1995 and 2003. (From Ghez et al. 2005.)

Lo 1982). In the <1 GHz regime, turnover of the spectrum slope is suggested, but the entire Sgr A* region suffers from free-free absorption and no signal is detected at 330 MHz (Pedlar et al. 1989). Duschl & Lesch (1994) claimed that a time-averaged spectrum in the 1–1000 GHz band shows $\alpha \sim 1/3$, which indicates synchrotron emission from mono-energetic electron distribution (Figure 2.8(a)). However, a simultaneous observation using VLA, BIMA, Nobeyama, and IRAM revealed the excess in the millimeter to sub-millimeter band (Falcke et al. 1998; Melia & Falcke 2001). Figure 2.8(b) shows a spectrum including infrared upper limits. We can see a hump structure, the so-called "submillimeter bump".

Superior spatial resolution ($<$0.1 mas $= 1 \times 10^{13}$ cm) of radio interferometers enable us to investigate the intrinsic size of Sgr A*, altough an observed size suffer from scattering by ionized electrons in the ISM. The red points in Figure 2.9 shows the observed sizes of Sgr A* as a function of wavelength. The black solid line is the λ^2 scattering law derived by Bower et al. (2006). The scattering effect dominates in the $\lambda > 1$ cm band while a source size appears in the $\lambda < 1$ cm band. After correcting the scattering effect (green points), the intrinsic size of Sgr A* at 1.3 mm is 37 μas, which corresponds to a few of Schwarzschild radius ($2GM/c^2 \sim 2 \times 10^{12}$ cm ~ 10 μas) for Sgr A* (Doeleman et al. 2008). The authors also confirmed the $\lambda^{1.4}$ dependence of the intrinsic size and suggested the stratified emission region.

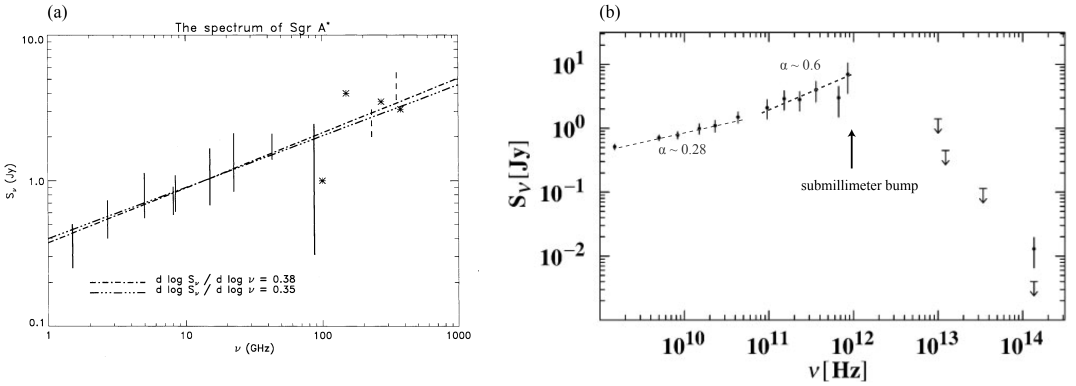

Figure 2.8. Radio spectra of Sgr A*. (a) Adopted from Duschl & Lesch (1994). The vertical bars show the range of time variability. The dashed-dotted line represents the best-fit power-law function with the index of ~1/3. (b) Adopted from Melia & Falcke (2001). The data between 1–300 GHz were taken simultaneously (Falcke et al. 1998). There are the remarkable breaks of the spectrum at ~60 GHz and ~1000 GHz.

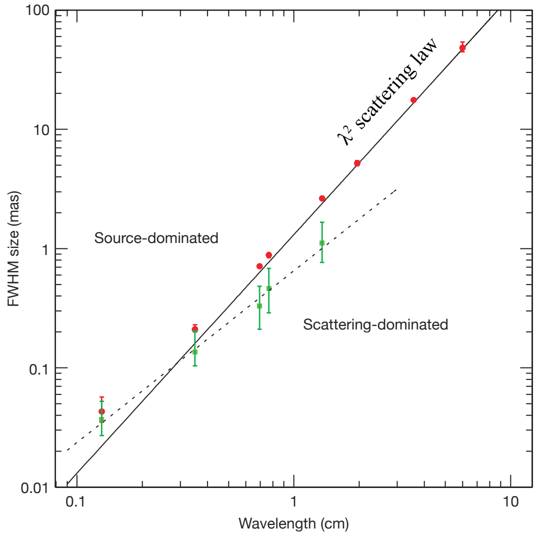

Figure 2.9. The angular sizes of the major axis of Sgr A*. The solid line shows the λ^2 scattering law. The scattering effect dominates below this line. The red and green points are observed and scattering-corrected sizes, respectively. (From Doeleman et al. 2008.)

X-ray

X-ray observatories had been expected to detect a loud activity, like AGNs, from Sgr A*. However, *Einstein*, *ROSAT*, *ASCA*, and *BeppoSAX* reported the upper limit of $<10^{36}$ erg s^{-1}, contrary to the expectation (e.g., Watson et al. 1981; Predehl & Truemper 1994; Koyama et al. 1996). Limited spatial resolution at most $\sim 10''$ of *ROSAT*/PSPC makes it difficult to eliminate contamination from nearby X-ray sources, and hence X-ray characteristics of Sgr A* bad been veiled for a long time.

Chandra firstly resolved the X-rays from Sgr A* within $0.3''$ and found the surprisingly low luminosity of 10^{33} erg s^{-1}, which is comparable to or even lower than other X-ray binaries (Baganoff et al. 2003, Figure 2.10(a)). The detected angular size is significantly larger than the instrumental response with the intrinsic size of $1\overset{''}{.}4$ (FWHM), which is consistent with the estimated Bondi-Hoyle accretion radius of $1''$–$2''$ (see Eq.2.3). The X-ray spectrum reported by Baganoff et al. (2003) is represented by either a power-law function with the photon index (Γ) of 2.7 or an optically thin thermal plasma model with $kT = 1.9$ keV (Figure 2.10(b)). The absorption column density is found to be 1×10^{23} H cm^{-2} .

Subsequent X-ray observations by *Chandra* and *XMM-Newton* have detected flares of Sgr A*, but it reached at most 10^{35} erg s^{-1} (Porquet et al. 2003; Nowak et al. 2012). The spectrum became harder ($\Gamma \sim 2$) in the flare state, although the photon index is strongly coupled with the absorption column density. The 3 Ms *Chandra* observation performed during 2012 revealed that flares occurred every one day with the luminosity range of 10^{34}–10^{35} erg s^{-1} and lasted from a few hundred to eight kilo secounds (Neilsen et al. 2013). There is no difference in spectral hardness ratios between the faint and bright flares. All of the X-ray flares associate with infrared flares (Markoff 2010).

Infrared

The identification of Sgr A* in the infrared band had been difficult because of confusion with stellar sources or thermal dust emissions. We can only obtain upper limit in the mid-infrared band (e.g., Serabyn et al. 1997; Cotera et al. 1999). In the near-infrared band, recent development of adaptive optics enables us to resolve the Sgr A* emission. Ghez et al. (2004) detected a variable point source within 18 mas of Sgr A* in the L' (3.8 μm) band. The observed luminosity varied in the range of 4–17 mJy on four separate nights. No other sources in this region show such large (factor of 4) and fast variation. The short timescale of the flux variation indicates that the emission comes from close to Sgr A* within 5 AU ($\sim 8 \times 10^{13}$ cm).

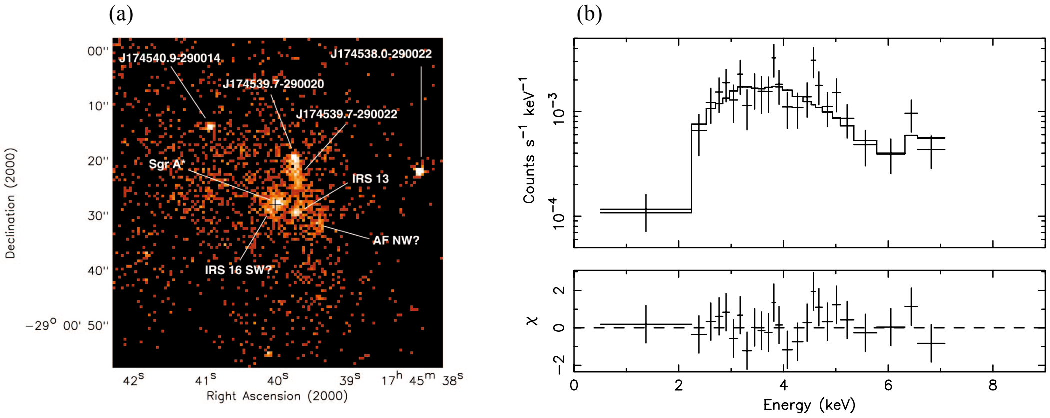

Figure 2.10. (a) *Chandra* 0.5–7 keV X-ray image of the central $1' \times 1'$ field of the GC. The position of Sgr A* is marked with the cross points. (b) X-ray spectrum of Sgr A* with the best-fit thin thermal plasma model, where temperature and absorption column density are 1.9 keV and 1.2×10^{23} H cm^{-2}, respectively. (Both from Baganoff et al. 2003)

Emission mechanism

Figure 2.11 shows the spectrum energy distribution (SED) of Sgr A*. The observed bolometric luminosity of Sgr A* is $\sim 10^{36}$ erg s^{-1}, which is eight orders of magnitude lower than its Eddington luminosity of 10^{44} erg s^{-1} (Figure 2.11; Genzel et al. 2010; Markoff 2010. This Eddington ratio of 10^{-8} is even four orders of magnitude lower than that of a typical low-luminosity AGN (LLAGN). What causes the extremely low activity of Sgr A*?

One possibility is a low accretion rate to Sgr A*. The IR observations discovered many early-type stars in the inner parsec of the GC (Krabbe et al. 1991; Najarro et al. 1994; Krabbe et al. 1995). The total mass-loss rate of the stars is $\sim 10^{-3}\ M_\odot$ yr^{-1} with the wind velocity (v_w) and density (n_w) of 500–2000 km s^{-1} and 10^3–10^4 cm^{-3}, respectively (e.g., Martins et al. 2007). The simple Bondi-Hoyle accretion flow model predicts the accretion rate of $\dot{M}_{\rm BH} = \pi R_A^2 m_{\rm H} n_w v_w$, where $R_A \equiv 2GM/v_w^2$ is the accretion radius and $m_{\rm H}$ is the hydrogen mass (Ruffert & Melia 1994; Coker et al. 1999). Therefor, the accretion rate from the stellar winds is

$$R_A = 0.04 \left(\frac{M}{4.5 \times 10^6\ M_\odot}\right) \left(\frac{v_w}{1000\ \mathrm{km\ s^{-1}}}\right)^{-2} \mathrm{pc}\ (\sim 1'') \tag{2.3}$$

$$\dot{M} = 1.3 \times 10^{-4} \left(\frac{R_A}{0.04\ \mathrm{pc}}\right)^2 \left(\frac{n_w}{10^3\ \mathrm{cm^{-3}}}\right) \left(\frac{v_w}{1000\ \mathrm{km\ s^{-1}}}\right) M_\odot\ \mathrm{yr^{-1}}. \tag{2.4}$$

Then, assuming the radiative efficiency $\eta = 0.1$ as the standard accretion disk, we find the luminosity of Sgr A* to be

$$L = \eta \dot{M} c^2 = 5.6 \times 10^{42} \left(\frac{\dot{M}}{10^{-4}\ M_\odot\ \mathrm{yr}^{-1}} \right)\ \mathrm{erg\ s}^{-1}, \tag{2.5}$$

which is 6–7 orders of magnitude higher than the observed bolometric luminosity. Therefore, the low luminosity of Sgr A* is not explained by the estimated accretion rate.

Another possible cause is extremely low radiative efficiency ($\eta = 10^{-7}$). Such a radiatively inefficient model is proposed by many authors, the so-called "advection-dominated accretion flow (ADAF)" (see Narayan & McClintock 2008 for a review). Figure 2.11(a) shows the model spectrum of the ADAF. Narayan et al. (1995) firstly proposed the ADAF model to explain both the submillimeter bump and the low X-ray luminosity. The submillimeter bump is explained by synchrotron emission from thermal plasma in the inner accretion flow, while X-rays come from bremsstrahlung of thermal plasma in the outer region. This model marginally represents the observed SED, but underestimates the emissions in the GHz band and the infrared band. Yuan et al. (2003) added the small fraction ($\sim$1.5%) of non-thermal electrons as a tail of the thermal electron distribution. They argued that synchrotron emission from the non-thermal electrons successfully represents low-frequency radio and infrared emissions.

Motivated by the discoveries of weak jets in the nearby LLAGNs, another model, where jet is the predominant radiative source, is also proposed (see Markoff 2010 for a review). This model well represents the radio to infrared SED including the GHz inverted spectrum by synchrotron emission from non-thermal electrons in a jet. X-ray emission in this model is considered to be synchrotron self-Compton.

Thses models are not excluded by the observational data at this time, and hence the emission mechanism for Sgr A* is still controversial.

2.3.3 Evidence of past activity

As shown in the previous section, Sgr A* is very quiescent now. However, recent observations have discovered relics of past Sgr A* activities. We introduce these observational evidence in this section.

X-ray reflection nebula

The X-ray observation by *ASCA* discovered strong 6.4 keV (Fe I) line in the GC region (Figure 2.4; Koyama et al. 1996). As shown in Figure 2.12, spatial distribution of the 6.4 keV lines is clumpy and coincides with the dense MCs found by the CS (J=1–0) line observation

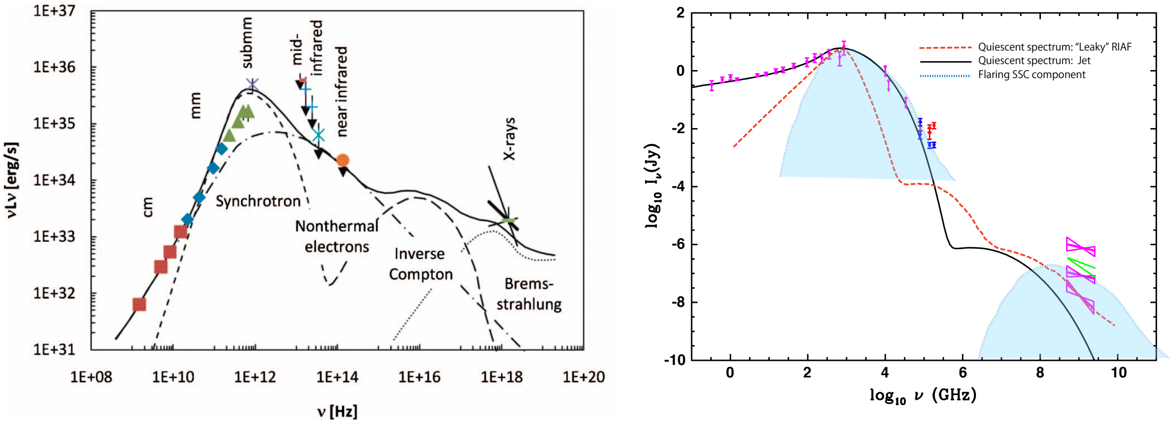

Figure 2.11. (a) Spectral energy distribution of Sgr A* with the ADAF model constructed by Yuan et al. (2003). The dashed, dotted, dashed-doted lines represent individual emission mechanisms, and the solid line shows the total emissions. (from Genzel et al. 2010.) (b) The same as (a) but with the jet model. You should note that the vertical axis is not νF_ν but F_ν. (from Markoff 2010.)

(Tsuboi et al. 1999). Since MCs are too cold to emit X-rays, they should be irradiated with high energy photons or cosmic-rays.

The particles exciting the cold MCs had been debated for a long time. Figure 2.13 shows the typical spectrum of the 6.4 keV clump derived from the Sgr A region. The equivalent width (EW) of the 6.4 keV line with respect to the associated hard continuum is ~1 keV. It is consistent with the predicted EW of the photon or proton origin (~1 keV) rather than that of electron origin (~400 eV). The strong Fe absorption edge in the hard-continuum indicates the photon origin rather than the proton origin. Nobukawa et al. (2010) found not only the 6.4 keV line but also the neutral Ar, Ca, Cr, Mn, and Ni lines (Figure 2.13). The EWs of all the lines are consistent with the photon origin. In addition to the spectrum shape, Inui et al. (2009) discovered that the flux and morphology of 6.4 keV lines in the Sgr B2 molecular cloud, whose spatial scale is a few parsec (~10 light yr), changed in 10 yr. This rapid variation is only achieved by photon irradiation, because charged particles which mainly contribute to excitation of neutral Fe (~10 keV for electrons and ~10 MeV for protons) have significantly lower velocity than the light speed. Nobukawa et al. (2011) also confirmed that the 6.4 keV flux and associated hard-continuum in Sgr B2 deceased by half in between 2005 and 2009, while no time variation on the 6.7 keV line flux was found (see Figure 2.14). Therefore, the photon irradiation is favor for the 6.4 keV clumps. We refer to the clumps as the X-ray reflection nebula (XRN).

From the intensity of 6.4 keV lines, the required luminosity for X-ray sources illuminating the MCs is estimated to be $\sim 10^{37} \times (D/10~\mathrm{pc})^{-2}$ erg s^{-1}, where D is the distance between

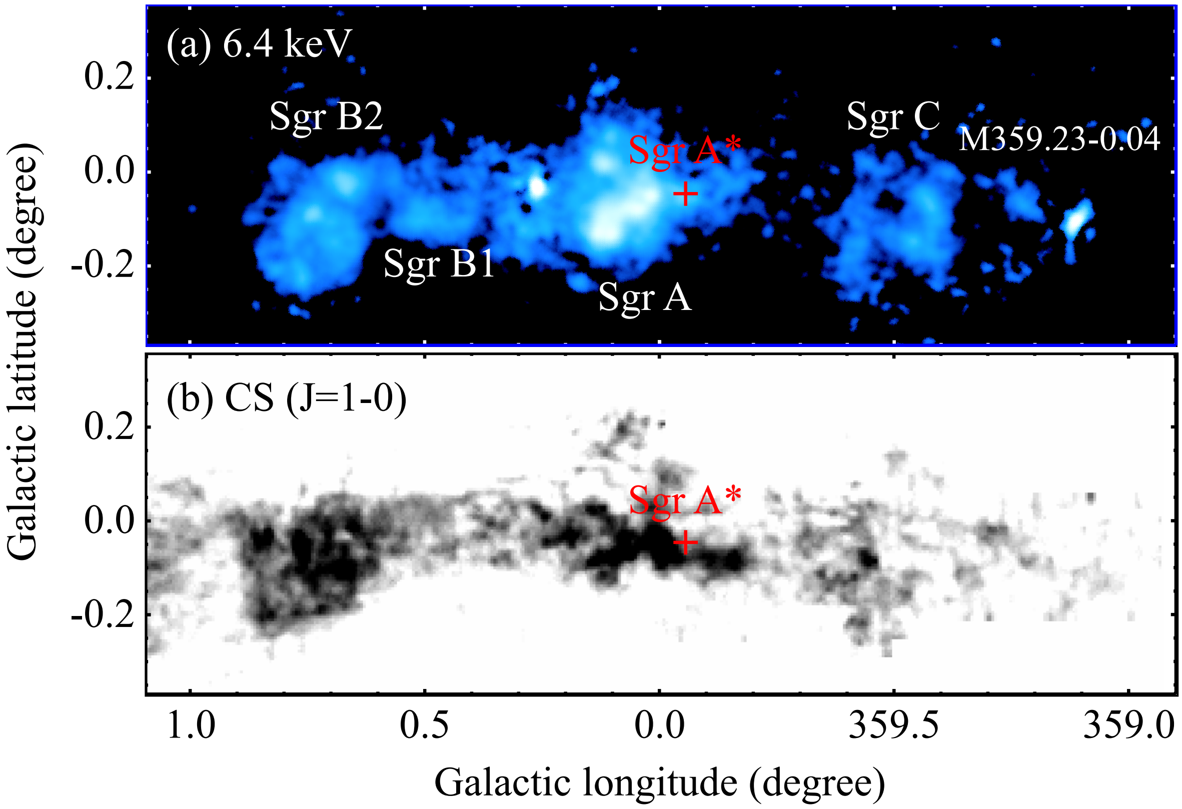

Figure 2.12. (a) *Suzaku* 6.4 keV image of the 2° × 0.8° field of the GC. (b) Image of CS (J=1–0), which traces dense MCs. (From Tsuboi et al. 1999.)

the XRN and the illuminating source. One of the XRNe, M359.23−0.04, can be illuminated by the nearby low-mass X-ray binary 1E 1740.7−2942 (Nakashima et al. 2010). However, the other XRNe have no bright nearby sources providing this luminosity. A remaining possibility is past Sgr A* flare of $>10^{39}$ erg s^{-1}.

When we have a line-of-sight distance toward an XRN and a distance between the XRN and Sgr A*, we can derive a period of past Sgr A* flare. In order to estimate the line-of-sight position of the XRNe, Ryu et al. (2009) developed a new method using the partial absorption of the 1 keV plasma in the GCXE. Applying this method to some 6.4 keV clumps, the authors determined the line-of-sight position the XRNe (Figure 2.15(a)). Based on this results, past light curve of Sgr A* is derived as shown in Figure 2.15(b); Sgr A* had been continuously active with 10^{39} erg s^{-1} 100-1000 yr ago.

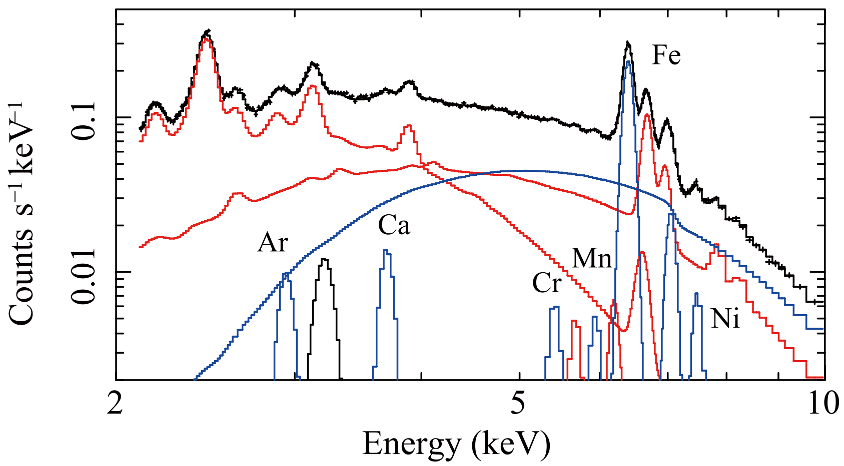

Figure 2.13. Spectrum of the 6.4 keV clump in the Sgr A region. The red lines represent the contamination of the 1 keV and 7 keV plasmas in the GCXE (see Section 2.2.2). The blue lines are the emissions from neutral atoms and the associated continuum emission. (From Nobukawa et al. 2010.)

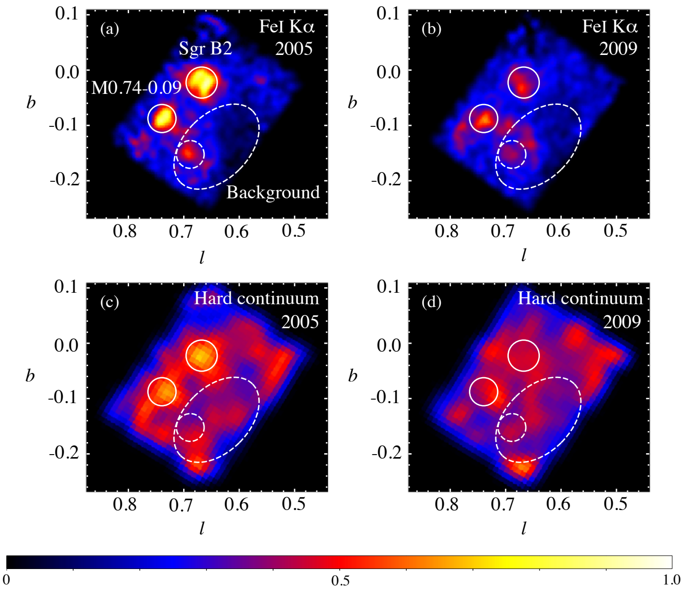

Figure 2.14. *Suzaku* X-ray images of the Sgr B2 region. The upper panels shows the 6.4 keV band image in (a) 2005 and (b) 2009. The lower panels shows the hard-continuum band image in (c) 2005 and (d) 2009. (From Nobukawa et al. 2011.)

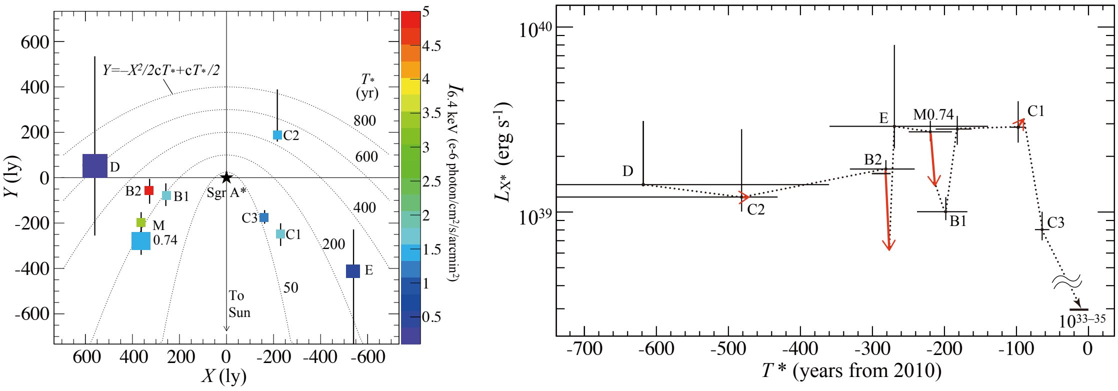

Figure 2.15. (a) Map of the XRN positions in the face-on-view constructed by Ryu et al. (2013). (b)Light curve of the past Sgr A* flares. (From Ryu et al. 2013.)

Fermi bubbles

All-sky survey performed by the *Fermi* gamma-ray observatory discovered large bipolar emissions, which has a bubble-like morphology extending 50°north and south of the GC with the width of 40°(Figure 2.16(a)). Therefore, they are referred to as the "*Fermi* bubbles". Surface brightness in the bubbles is nearly uniform, so that bubble shape is neither simple shell nor sphere. As shown in Figure 2.17, Gamma-ray spectrum of the bubbles has spectral photon index of ∼2, which is harder than that of the disk region. No significant spatial variation of the spectrum in both of the north and south bubbles is found. Although it is difficult to determine the accurate distance toward the *Fermi* bubbles, their considerably symmetric morphology to the GC strongly suggests that the a past GC activity formed the *Fermi* bubbles.

There are some features possibly associated with the *Fermi* bubble in other wavelength. The North polar spur, which is seen in the low-frequency radio image (Figure 2.16(b)) and the X-ray image (Figure 2.16(c)), is located eastern edge of the northern *Fermi* bubble. Kataoka et al. (2013) proposed that the North polar spur was formed by a weak shock driven by the bubble. On the other hand, the Loop I , which is also seen in the radio and X-ray images, is less associated with the gamma-ray emissions. The GHz band radio image (Figure 2.16(d)) shows the biconical features above and below the GC, the so-called "*WMAP* haze". It coincides with the foot points of the *Fermi* bubbles. The *WMAP* haze exhibits hard spectrum probably due to synchrotron emission from harder electron distribution (Figure 2.17(b)). Assumed the Combined spectrum of the *Fermi* bubbles and the *WMAP* haze is marginally represetned by single power law electron energy distribution with the index of 2.0–2.5 (Figure 2.17): the gamma-rays are emitted by inverse Compton with the Galactic radiation fields and radio continuum is emitted by synchrotron with the magnetic filed of

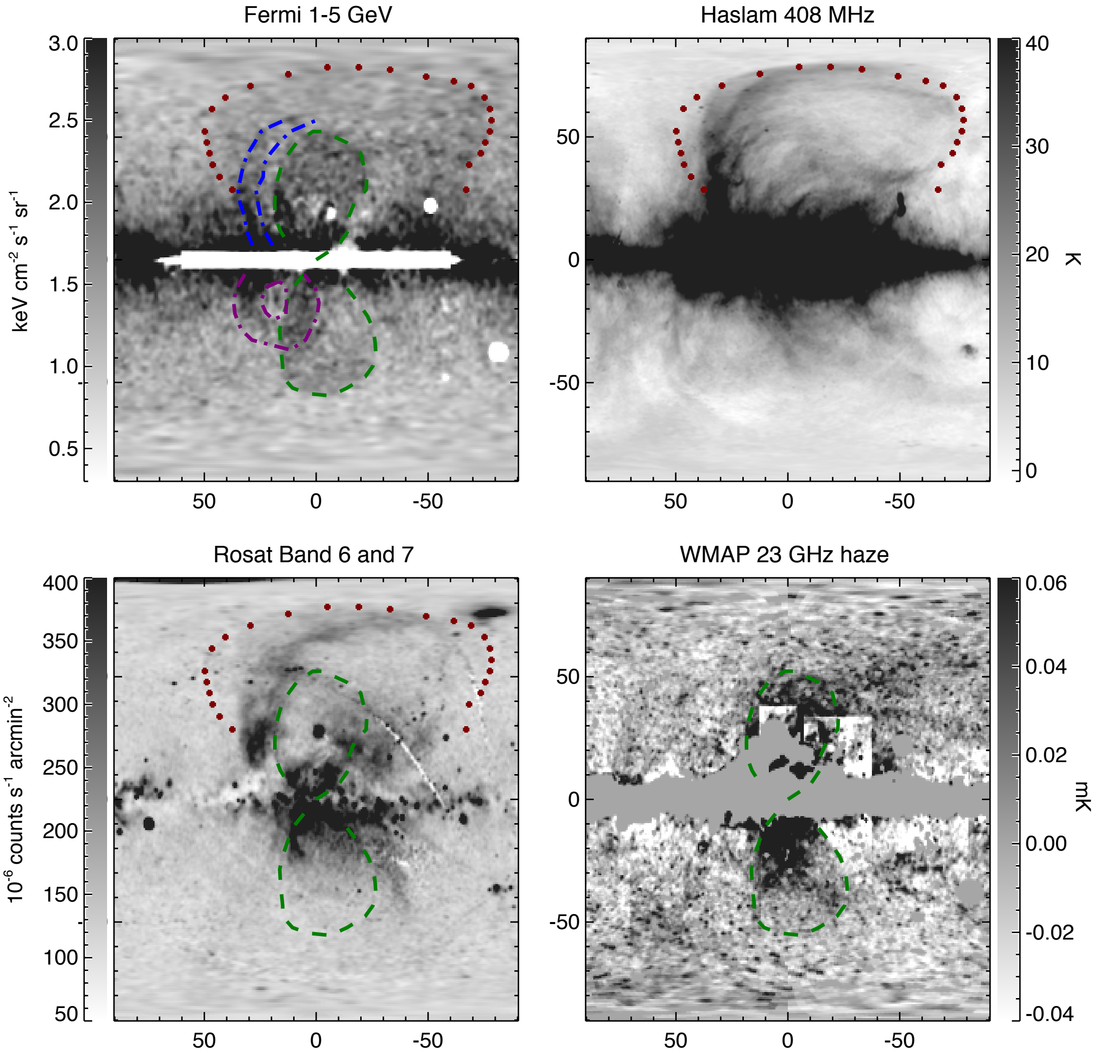

Figure 2.16. Images of the *Fermi* bubbles and possibly associated features in other wavelength. (a) *Fermi* image in the 1–5 GeV band. The dotted green, blue, and red curves show the bubble features, the North polar spur, and Loop I, respectively. (b) *Haslam* 408 MHz band image. (c) *ROSAT* 1–2 keV band image. (d) *WMAP* 23 GHz band image. (From Su et al. 2010.)

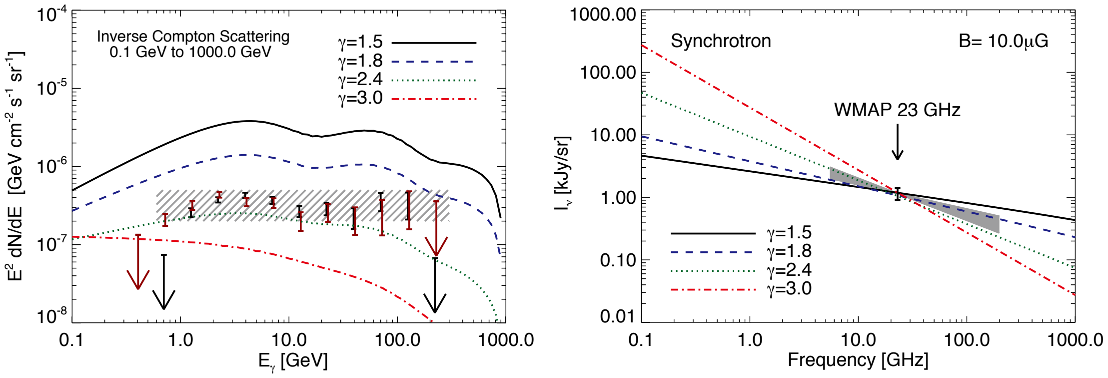

Figure 2.17. (a) Spectrum of *Fermi* bubbles. (b) Spectrum of *WMAP* haze. (From Su et al. 2010).

∼10 μG. This model implies the total energy of the bubbles reaches 10^{55}–10^{56} erg (Carretti et al. 2013; Kataoka et al. 2013).

The origin of the *Fermi* bubble is still under debate. Two possible scenario is suggested at present: a Sgr A* jet or a star-formation-driven outflow. In the context of a Sgr A* jet, a flare of sub-Eddington luminosity (10^{42} erg s^{-1}) a few Myr ago is proposed (Su et al. 2010; Zubovas et al. 2011). In the scenario of a star-formation-driven outflow, a wind velocity is estimated to be 1000 km s^{-1}, and then the dynamical timescale is 10 Myr (Su et al. 2010; Carretti et al. 2013). If this is the case, energy injection of 10^{41} erg s^{-1} is required to form the *Fermi* bubbles.

2.4 Subject of This Thesis

As shown Section 2.3.3, recent high-energy observations have been unveiled the past GC activities. However, the samples are still limited and there is a large gap in the activity history between 10^3 and 10^6 years ago (see Figure 2.18). Our aim is to find other relics of GC activities and to reveal the history of them.

Past X-ray studies of the GC are mostly concentrated on the Galactic plane region as reviewed in this chapter. However, a signature of past GC activity may be conceal by the strong GCXE in the on-plane region. Therefore, We focused on the Galactic bulge region, which is less contaminated by the GCXE and is more suitable to extract pure phenomena associated with the GC activities. We performed the survey of this region with the X-ray observatory of *Suzaku*, whose details are represented in Chapter 3.

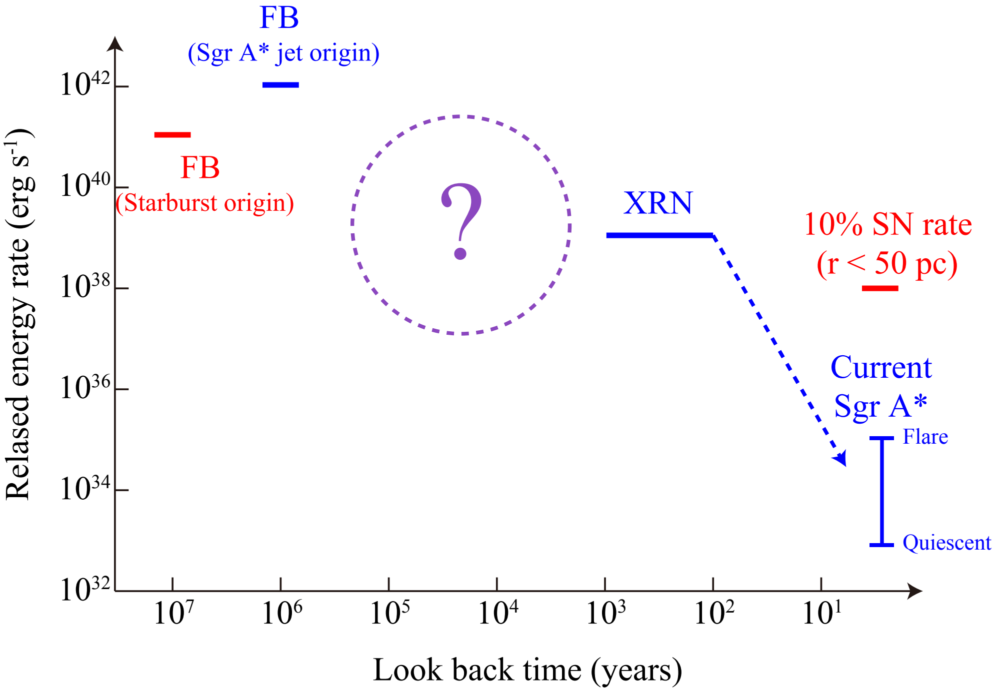

Figure 2.18. Schematic diagram of past GC activities.

Chapter 3

Instruments

In this chapter, we review *Suzaku* and its onboard instruments, which were used for the observations of the Galactic center.

Contents

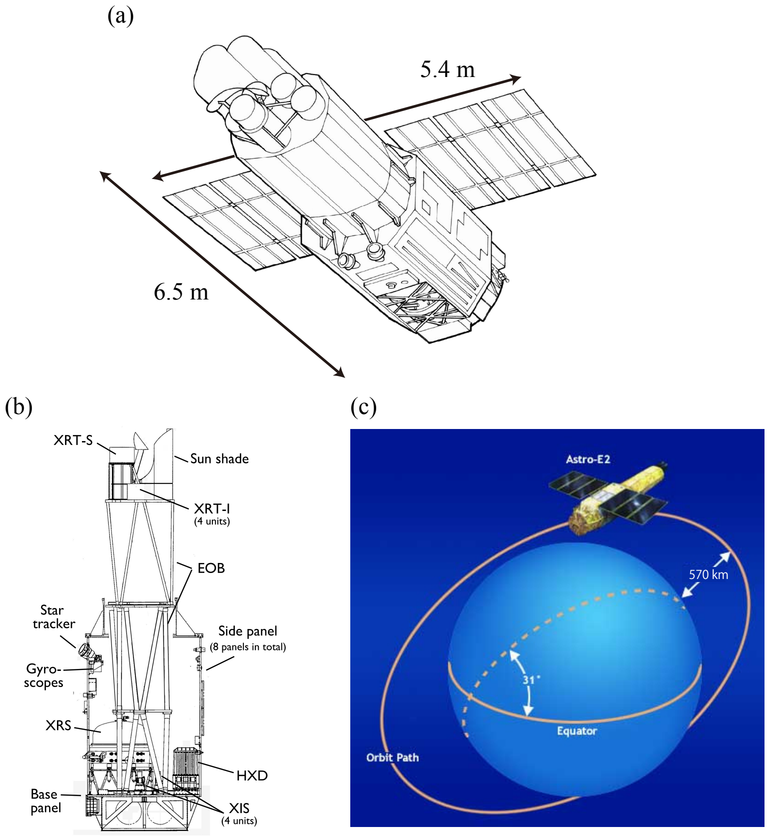

Figure 3.1. (a) Appearance of *Suzaku* in the orbit. (b) Schematic view of the configuration of instruments and satellite systems. (c) The *Suzaku* orbit.

3.1 Overview of *Suzaku*

Suzaku is the fifth japanese X-ray astronomy satellite lunched in 2005 July 10 from the Uchinoura Space Center (USC) by Japan Aerospace Exploration Agency (Mitsuda et al. 2007). Figure 3.1 shows a schematic view of *Suzaku* and its orbit. The length of the spacecraft is 6.5 m after extending the extensible optical bench (EOB). The total weight is ~1700 kg. It was put into a near-circular orbit at 570 km altitude with an inclination angle of 31 (Figure 3.1(c)). An orbital period is 96 minuets. The low earth orbit has a merit in less exposure of cosmic-rays, while celestial targets are occulted by the Earth for one third of each orbit except for targets near the orbital poles. Tracking and data down-link are managed in the USC. The satellite passes over the USC 4–5 times a day for ~10 minutes per pass. Attitude of the satellite is controlled by two star tracker systems, and ~10 minuets are required to direct the satellite toward a target.

Suzaku has a capability of high-sensitivity and wide-band spectroscopy. It carries two distinct scientific instruments: the X-ray Imaging Spectrometer (XIS; Koyama et al. 2007c) and the Hard X-ray Detector (HXD; Takahashi et al. 2007). The XIS is imaging-spectrometer using a X-ray CCD camera, which is mounted on the focal plane of a dedicated X-ray Telescope (XRT; Serlemitsos et al. 2007). The XIS has a large effective area and moderate energy resolution in the 0.2–12 keV band. The HXD is non-imaging collimated detector for hard X-rays covering the bandpass of 10–600 keV. The XIS and the HXD work in complementary and covers the wide bandpass. *Suzaku* has also carried the micro-calorimeter system, named the X-ray Spectrometer (XRS), but the XRS unfortunately failed to work on 2005 August 8 because of liquid helium loss. In the following sections, we described details of the XRT and the XIS, which were mainly used in this thesis.

3.2 X-ray Telescope (XRT)

3.2.1 X-ray optics

To focus visible light, we usually use refraction by lenses whose refraction index is much larger than 1. However, a refraction index depends on wavelength, and it becomes nearly 1 (and smaller than 1) in the X-ray band. It is because that we are not able to use lenses for focusing X-rays. Therefore, X-ray optics used either reflection, diffraction or interference.

X-ray telescopes commonly use the reflection by mirrors at very shallow angles of $<1^\circ$ (grazing incidence reflection). Based on this idea, Wolter (1952) proposed the some designs composed of two-stage reflection mirrors realizing a wide filed-of-view (FOV). The most popular design for X-ray astronomy is the Wolter type I telescope, where primary and secondary mirrors are aligned with paraboloid and confocal hyperboloid, respectively as shown in Figure 3.2. Since one grazing incidence mirror has very small collecting area, a nesting technique of thin mirrors is necessary to increase a photon-collecting capability. However, nesting causes degradation of angular resolution because accurate alignment of all nested mirrors is difficult. There is a tradeoff between an effective area and angular resolution.

3.2.2 Telescope design

The *Suzaku* XRT is an Wolter type I X-ray telescope consisting of closely nested thin-foil reflectors, which realize a light telescope with a large effective area. In the XRT, the shapes of the primary and secondary reflectors, which are originally a paraboloid and hyperboloid, respectively, are both approximated by cones. This approximation limits the spatial resolution as $l \tan\theta$, where l and θ are the axial length and the grazing angle, respectively. For the

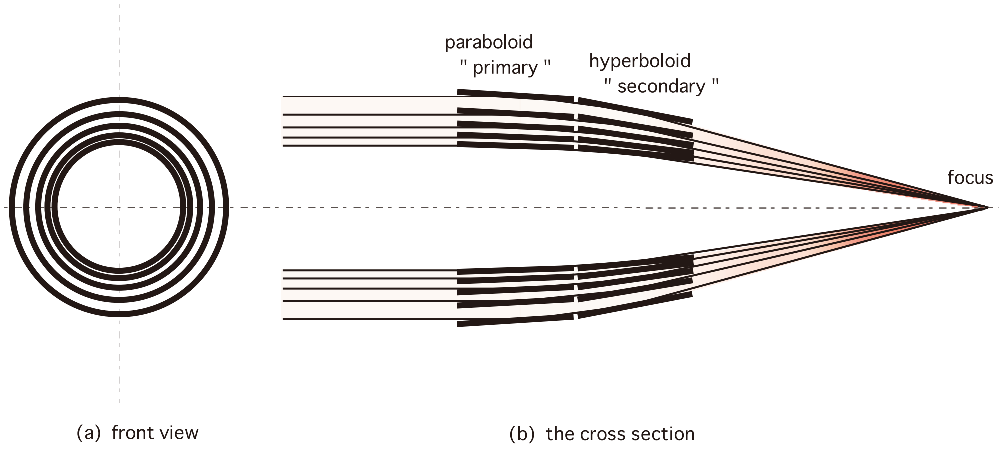

Figure 3.2. (a) Schematic view of an Wolter type I telescope consisting of nested thin-foil reflectors: (a) front view and (b) the cross section of the telescope (Mori et al. 2005).

Suzaku configuration, it is calculated as 18″ in half power diameter (HPD). This degradation is negligible compared to other degradation factors such as the alignment of mirrors.

Figure 3.3(a) is a photo of one XRT module, which contains 1400 reflectors with 175 nested shells. The telescope has a weight of 19.7 kg, a height of 279 mm, a geometrical area of 873 cm^2, and a focal length of 4.75 m. An innermost and an outermost diameters of the nested shells are 118 mm and 399 mm, respectively. An incident angle of each reflector is between $0\overset{\circ}{.}18$–$0\overset{\circ}{.}60$. Each reflector was produced through a replication method in which a thin ($\sim$0.1 μm) gold layer sputtered on a highly smooth glass tube was transferred to an aluminum substrate (152 μm thickness and 101.6 mm axial length) with an epoxy adhesive (25 μm thickness). Figure 3.3(b) shows a photo of reflectors.

In a incident side of the telescope, a pre-collimator to mitigate stray light (see following section) is mounted on, and covered by a thermal shield to isolate the XRT thermally from space and to reflect infrared radiation from the interior of the spacecraft. The XRT temperature is kept at $\sim$20 °C.

3.2.3 In-flight performance

Effective Area

Figure 3.4(a) shows the simulated effective area of the one XRT module as a function of incident X-ray energy. Strong absorption edges in the 0.2–2 keV band comes from transmittance of the thermal shield, which consists of a 0.24 μm polyethylene terephthalate film (C10H8O4) coated with an 30 nm aluminum layer. Other absorption edges in the 2–3 keV

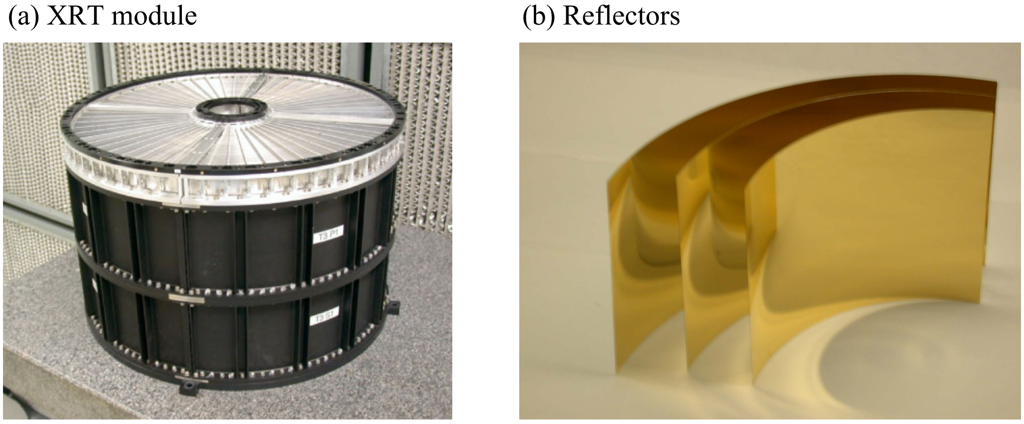

Figure 3.3. Photos of (a) one XRT module and (b) reflectors nested in the XRT.

band and at 12 keV are due to Au coated on the reflectors. Using a observation of the Crab nebula, the absolute photon flux, photon index, and absorption column densities were checked. The results are consistent with the standard value compiled by Toor & Seward (1974).

The effective are of the XRT decreases with increasing the off-axis angle because incident X-ray are partially obscured by the backside of the neighbor reflectors. This effect is more sever at higher energies. It is called the "vignetting" effect. The amount of vignetting effect is also calibrated by the observations of the Crab nebula with various off-axis angles. The resultant curve is shown in Figure 3.4(b). We can see steeper degradation for higher energy X-rays. At the $8'$ off-axis angle, which corresponds to the edge of the XIS detector, the effective area is half of that at the on-axis. The effective are is calibrated within $\sim 5\%$ over the FOV.

Angular resolution

The imaging capability of the XRT was investigated by the observation of SS Cygni, which is a moderately bright point source suitable for this calibration. Figure 3.5(a) shows the observation image. The shape of the image is asymmetric compared with the ray-trace simulation shown in Figure 3.5(b), even if the ray-trace simulation is fine-tuned for each quadrant. The spiky structures in the observation image is due to shadows of the supporting bars and misalignments of the reflectors.

Figure 3.5(c) and Figure 3.5(d) show the point spread function (PSF) and encircled energy function (EEF) derived from the observational result, respectively. The large difference

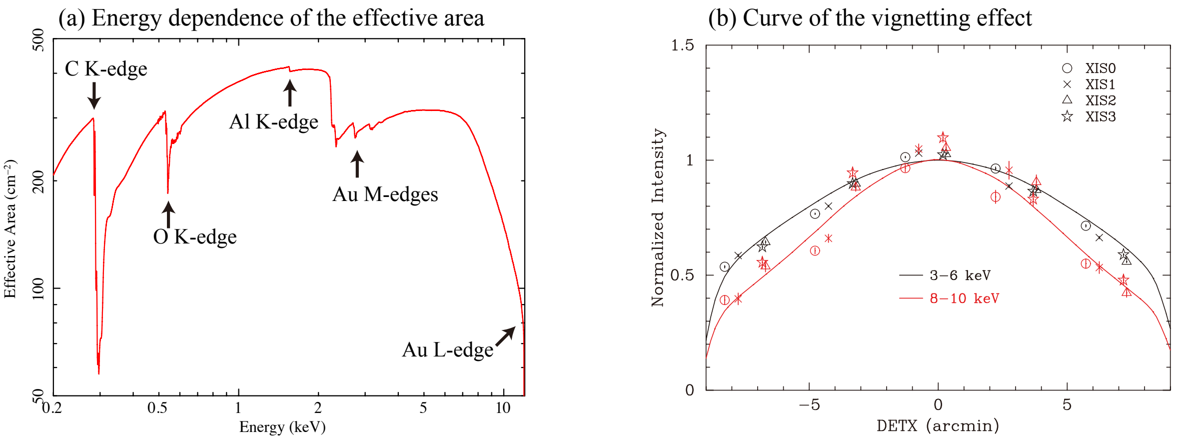

Figure 3.4. (a) Simulated on-axis effective are of one XRT module as a function of X-ray energy. Obvious absorption edges are labeled. (b) Curves of the vignetting effect. The count rate derived from the Crab nebular observations are shown in symbols, and the results of ray-trace simulations are shown in the solid lines.

between the observation and the simulation nearby the image center is due to the attitude error of the satellite control Uchiyama et al. (2008). The EEF in the range of $1'$–$6'$ is calibrated within 4%. The half power diameter of the XRT is $\sim 2'.0$

Stray light

The closely nested structure causes unexpected reflections of X-rays coming from the off-axis angle, the so-called "stray light". As shown in Figure 3.6, the two passes are possible. One is the secondary reflection where incident photons are not reflected by a primary mirror but only by a secondary mirror, and another is the backside reflection where photons are reflected by the backside of a primary mirror. The stray light become serious problem when we observe a weak emission with a bright point source out of FOV.

For the *Suzaku* XRT, the pre-collimator is installed on the incident side, and then the stay light is remarkably suppressed compared to the *ASCA* X-ray telescope, which has the basically same structure except for the pre-collimator Serlemitsos et al. (1995). As shown in Figure 3.7, the stray light due to the secondary reflection is fairly reduced with pre-collimator, but still remains at $20'$ and $60'$ off-axis angles (Mori et al. 2005).

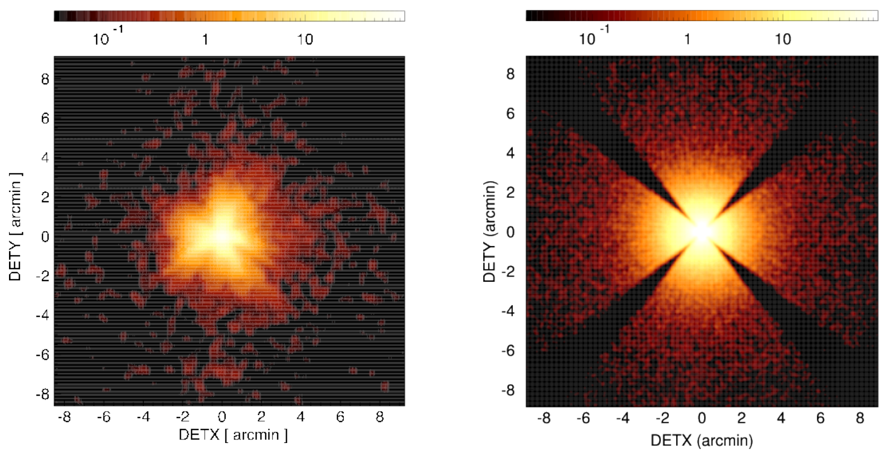

(a) Observation image

(b) Ray-trace simulation image

(c) Point spread function

(d) Encircled energy function

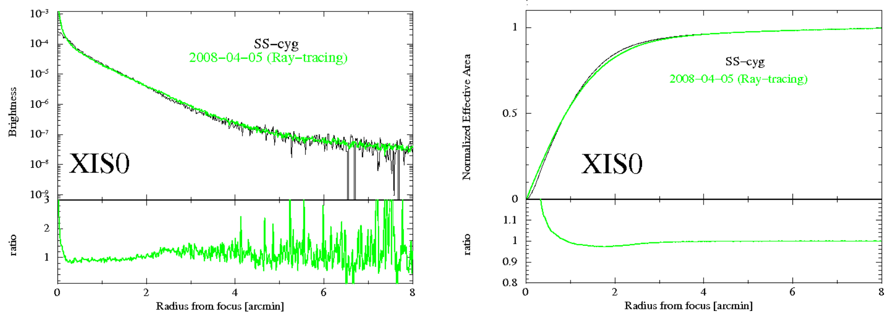

Figure 3.5. (a) XIS image taken from the observation of SS Cygni. (b) Ideal image obtained from a ray-trace simulation. (b) Point spread function and (d) encircled energy function. For both the figures, black and green lines are the observational results and simulated results, respectively. The lower panels show the residuals between the observation data and the simulation data.

3.3 X-ray Imaging Spectrometer (XIS)

3.3.1 Overview of the XIS system

The XIS is X-ray imaging-spectrometers consisting of four set of CCD camera systems. The system has been developed and maintained by a collaboration of Japan (ISAS/JAXA, the University of Kyoto, Osaka, Miyazaki, and Kogakuin) and the United States (the Massachusetts Institute of Technology (MIT)).

Figure 3.8 is a photo and a schematic view of one camera system. The system has a weight of 48.7 kg and consumes 67 W at a bus voltage of 50 V during normal operations. The CCD cameras are cooled at −90 °C by thermoelectric coolers to reduce dark current.

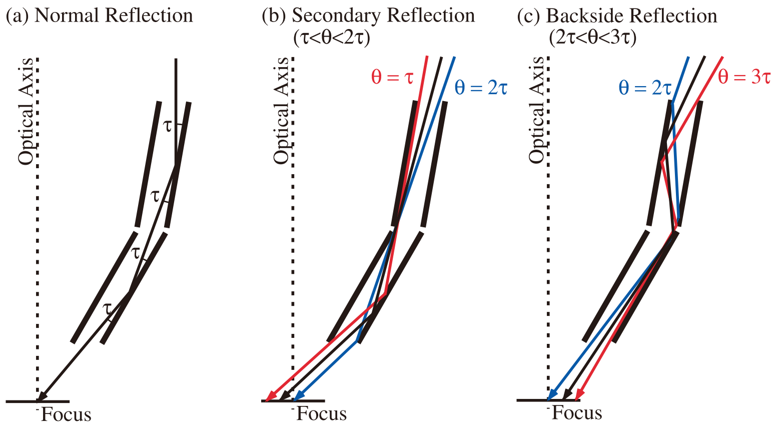

Figure 3.6. Schematic view of the incident X-ray passes. (a) normal double reflection, (b) secondary reflection, and (c) backside reflection are illustrated. The stray light is formed by the passes of (b) and (c).

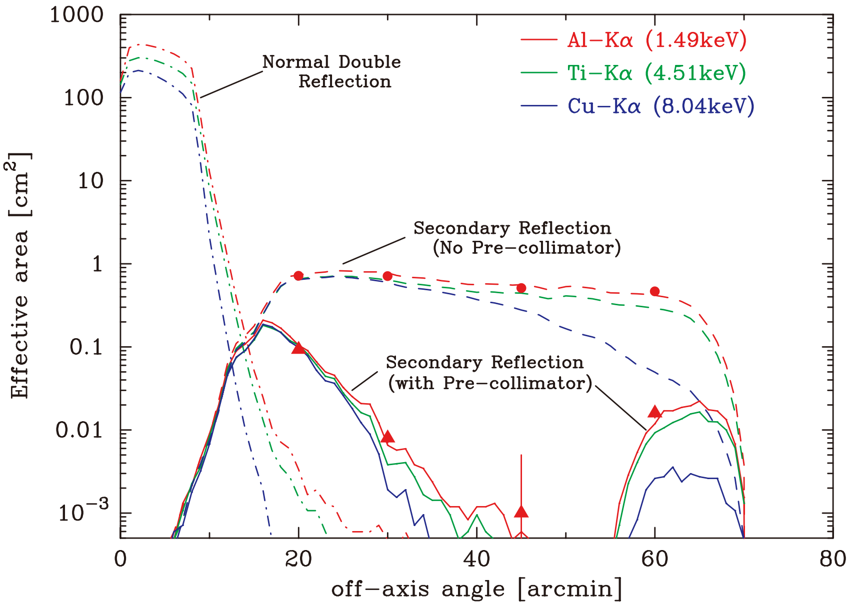

Figure 3.7. Ground measurement of the stray light with and without the pre-collimator (Mori et al. 2005).

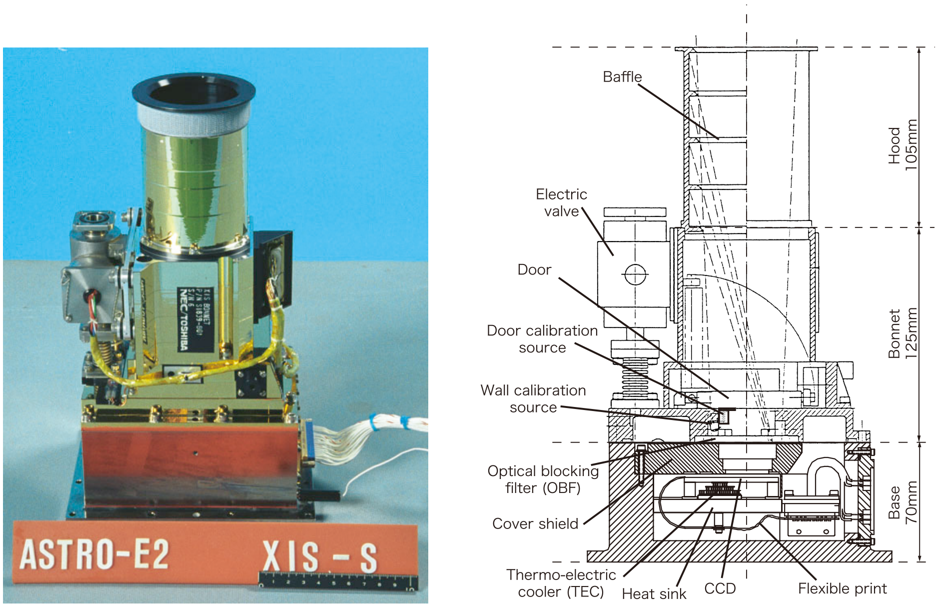

Figure 3.8. Photo (left) and a schematic view (right) of one camera system of the XIS.

The incidence of optical and UV photons are prevented by an optical blocking filter (OBF), which is installed on the surface of the CCDs. Calibration sources of ^{55}Fe, whose half life is 2.73 years, are located above the CCDs and illuminate corners of them to monitor in-flight performance.

The CCD is clocked by the analog electronics (AE) system, which supplies the various voltages in the CCD. Obtained analog X-ray signals are also transferred to the AE and converted to digital signals. The digitized signals are then transferred to the digital electronics (DE) system, where raw pixel data are temporally stored, event detection is carried out, telemetry packets are made, and finally sends to the main digital processor of the satellite.

3.3.2 Device description of the CCD camera

X-ray CCDs have two-dimensional array of photo sensitive sells (pixels) which produce a number of electron-hole pairs proportional to the energy of incident X-ray photons. After exposure, signal charges are transferred to the readout gates clocking the gate voltage. Since CCDs achieve the fine pixel pitch ($\sim$20 μm) and the fano-limited energy resolution ($\sim$130 eV at FWHM for 6 keV X-rays), they are widely used in the modern X-ray observatories: *Suzaku*, *Chandra*, *XMM-Newton*, and *Swift*.

The XIS used a MOS-type frame transfer CCD fabricated by the MIT Lincoln Laboratory. Transfer clocking is three phase operation. It a format of 1024 × 1024 pixels with a pixels pitch of 24 μm (Figure 3.9). Combined with the XRT, the XIS has a $17'.8 \times 17'.8$ field-of-view.

The frame-store area is divided into four segments, which have own readout gates. The charge transfer rate is fixed at 24.4 μs pixel^{-1}. In the normal mode, $24.4 \times 1024 \times (256+20) \sim$ 6.9 s (including under- and over-clocked pixels) is required to readout the stored signals from a gate in each segment. The timing resolution is limited by this charge transfer time. In order to increase the timing resolution, XIS CCD has window options (1/4 and 1/8) and a P-sum mode. In the window options, effective pixels are limited to 1/4 or 1/8 of the entire area in order to reduce the charge transfer time. In the P-sum mode, signals in a column is summed in one pixel, so that the charge transfer time is fairly reduced while imaging capability is lost.

Three CCDs are front-illuminated (FI) type (XIS0, 2, and 3) and the other one is back-illuminated (BI) type (XIS1). The quantum efficiency (QE) of both type of CCDs is shown in Figure 3.10(a) The FI CCD is superior in the high energy band for a thick depletion layer of $\sim$65 μm, but its entrance window has a MOS gate structures made of 0.28 μm Si and 0.44 μm SiO_2, which severely degrades the QE below 1 keV. On the other hand, the BI CCD has very thin entrance window (5 nm HfO_2, 1 nm Ag, and 3 nm SiO_2), which is made by the chemisorption charging process, and realizes high QE for low energy X-rays. However, back-thinning process to achieve the full-depletion reduce the thickness of effective layer to $\sim$42 μm. Therefore, the FI and BI CCDs work complementary. Effective areas combined with the XRT are also shown in Figure 3.10(b). The chemisorption charging process also improved the charge correction efficiency for low energy X-rays, which are absorbed at the surface of the CCD. Therefore, spectral shape of the XIS BI CCD is fairly better than that of Chandra/ACIS and XMM-Newton/EPIC (Burke et al. 2004).

In the space environment, charge transfer inefficiency (CTI) in a CCD gradually increases, because charge traps are made due to bombardment of high energy cosmic-rays (e.g., Yamashita et al. 1997). In order to mitigate the radiation damage, the XIS CCD is equipped with function to inject artificial charges. A charge injection gate is located at the opposite side of the readout gate. Before an exposure, an arbitrary amount of charges ($\sim$1000 e^-) are injected into every 54th rows. These artificial charges fill traps in charge transfer, and prevent signal charges to be captured by the traps. This technic called the "spaced-raw charge injection (SCI)".

XIS2 suddenly showed anomaly at 1:03 UT on Nov 9, 2006. About 2/3 of the image was flooded with a large amount of charge, which was leaked somewhere in the imaging region. It is probably caused by a micro-meteorite impact. Thus, entire XIS2 have not been functional for scientific observations. A possible micro-meteorite impact also occurred at 2:00 UT on June 23, 2009, and a part of segment A of XIS0 have not been functional. Since the other segment of XIS0 was not affected by this anomaly, we used the 3/4 of XIS0 for analysis in this thesis.

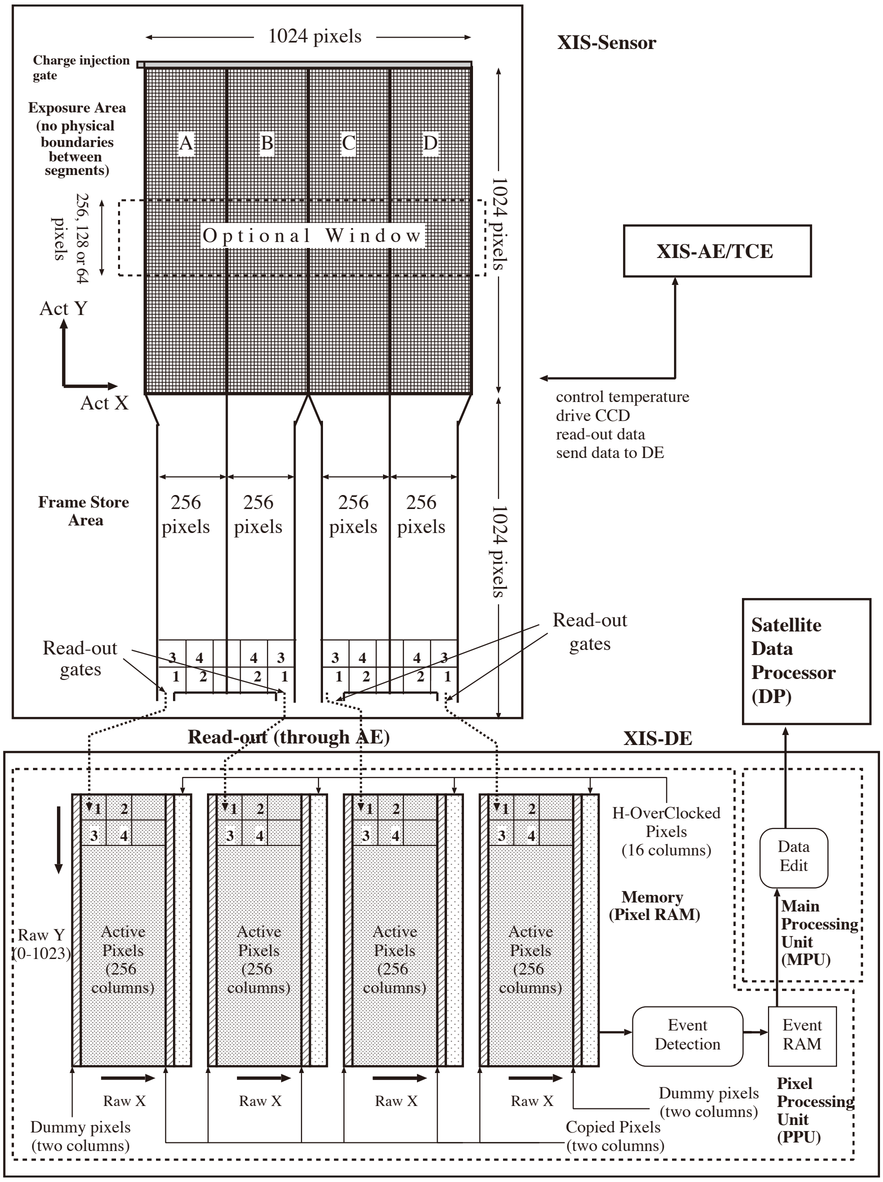

Figure 3.9. Schematic overview of the XIS system.

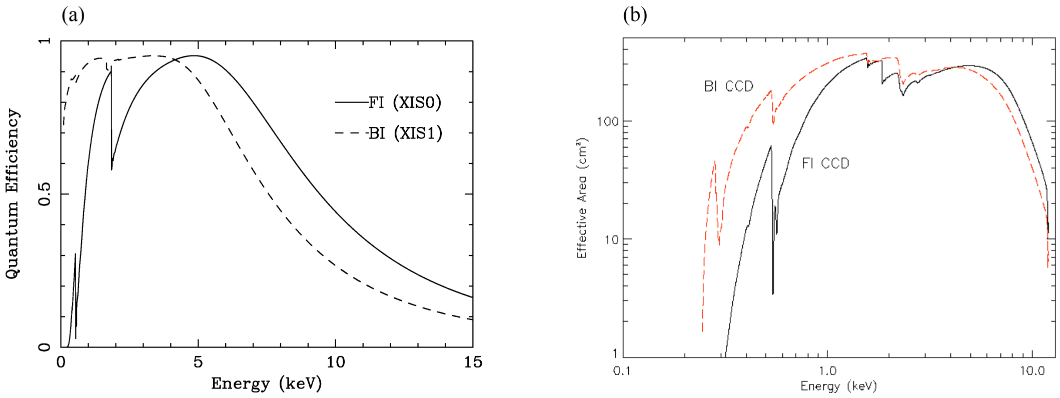

Figure 3.10. (a) The QE as a function of incident energy, calculated using best estimate values of the thickness of dead layers and depletion layer. The solid line represents the FI CCD (XIS 0) and the broken line is for the BI CCD (XIS 1). (b) The effective are of the XIS combined with the XRT. The black and red lines represents the FI CCD and BI CCD, respectively.

3.3.3 In-flight performance and calibration

SCI operation

Increasing CTI degrade the signal pulse hight. Since the amount of the degradation varies from pixel to pixel, the width of the pulse hight also increase. Figure 3.11 shows the time history of the pulse hight and its width monitored by the ^{55}Fe calibration source. Just after the launch, the signal pulse hight of the calibration source is calibrated to be 5894 eV (Mn Kα line), and the energy resolution is $\sim$130 eV. However, both degrade rapidly between the launch and the mid 2006.

The SCI technique has been applied since August 2006, and the gain and the energy resolution are successfully recovered to the performance of nearly just after the launch. Although performance gradually degrades even in the SCI mode, its slope is considerably small compared to the operation without the SCI. The slopes are different among FIs (XIS0 and XIS3) and BI (XIS1) from the mid 2006 to the late 2010. It is due to the difference of the amount of injected charges: $\sim$1640 e$^-$ (equivalent to 6 keV signal) for the FIs and $\sim$550 e$^-$ (equivalent to 2 keV signal) for the BI. Increasing charge traps increase the CTI. For the BI sensor since 2011, the amount of injected charges increase to the same amount for the FI sensors, and then the performance became comparable to the FIs.

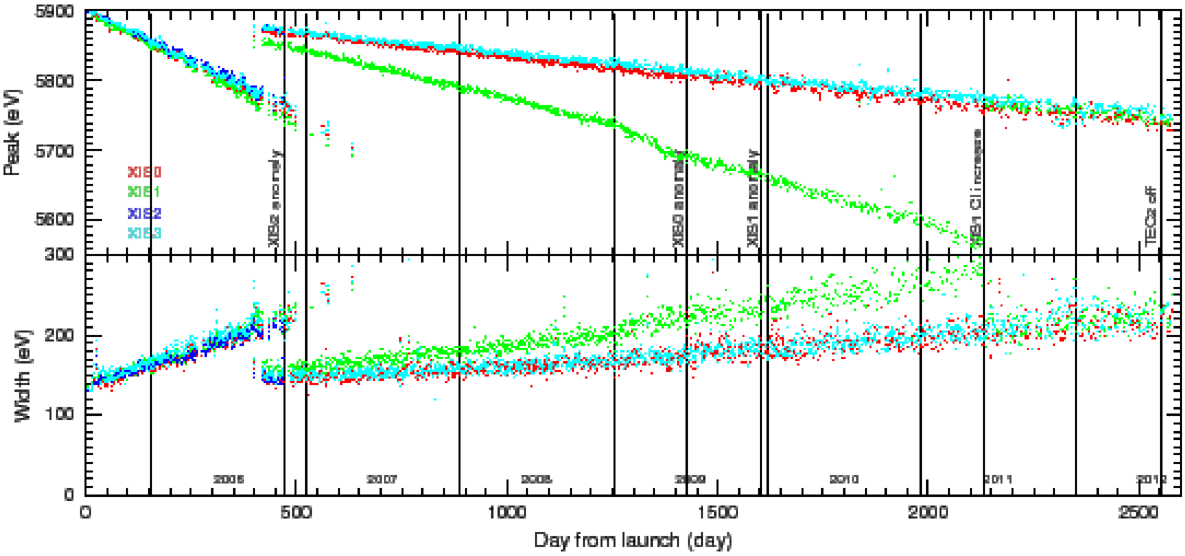

Figure 3.11. Long term trend of ^{55}Fe centroid energy and width before trail and CTI correction. The data after calibration are shown in Figure 3.13.

CTI correction

As shown in Figure 3.11 pulse hight degradation occurs even applying the SCI technic, and hence the energy scale calibration from pixel to pixel is necessary to bring out the best performance of the XIS. Figure 3.12 shows a pulse hight profile along the charge transfer number (row pixel number) shows the saw-tooth like shape at 54 pixel intervals. It is because that trapped artificial charges are detrappted in a certain time, and the efficiency of the charge injection decreases with increasing the distance from the injected row.

In order to correct the CTI including the saw-tooth like profile, Uchiyama et al. (2009) composed a model of the observed pulse hight (PH) as a function of the elapsed time (t), row pixel number (k), and intrinsic pulse hight (PH_0):

$$\begin{aligned} PH(t,i,PH_0) &= [1-c_1(t,i,PH_0)]^i\,[1-c_2(t,PH_0)]^{1024}\,PH_0 && (3.1)\\ &\simeq [1-i\times c_1(t,i,PH_0)]\,[1-1024\times c_2(t,PH_0)]\,PH_0 && (3.2)\end{aligned}$$

where c_1 and c_2 are the CTI per one transfer due to the slow and the fast transfer, respectively. Assuming c_1 and c_2 is $\ll 1$, Eq.3.1 is approximated by Eq.3.2. Then, c_1 and c_2 are represented as below:

$$\begin{aligned} c_1(t,i,PH_0) &= \left[c_{1t}(t)+\frac{c_{1b}(t)-c_{1t}(t)}{54}(i \bmod 54)\right]PH_0^{-\beta} && (3.3)\\ c_2(t,PH_0) &= c_2'(t)PH_0^{-\beta} && (3.4)\end{aligned}$$

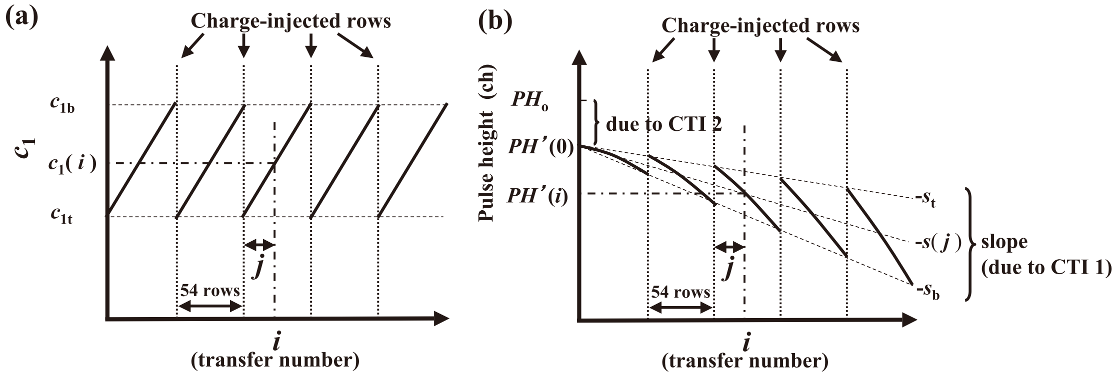

Figure 3.12. Schematic view of (a) CTI1 and (b) observed pulse hight as a function of the charge transfer number.

where c_{1t}, c_{1b} are c_1 values at the peak and valley of the sawtooth normalized by a certain PH_0, $c'_2(t)$ is c_2 values for a certain PH_0, and β is a parameter showing dependence of the CTI on PH_0 . Sawada et al. (2012) improved this model introducing the time-variable β and the discontinuous slope of c_{1t} and c_{1b}. Figure 3.13 shows the the center of emission lines after the correction of the CTI using the above model. The data well agree with the reference values.

As shown in Figure 3.14, the energy resolution is considerably improved after the energy scale correction compared with Figure 3.11. The observed width of $FWHM$ is given by

$$FWHM \quad = \quad \sqrt{FWHM_{\rm init}^2 + FWHM_{\rm add}^2} \tag{3.5}$$

where $FWHM_{\rm init}$ is the width at the launch and $FWHM_{\rm add}$ is the additional width due to the CTI degradation. $FWHM_{\rm add}$ is then modeled as a function of the X-ray energy (E) and the time after launch (t) as below.

$$FWHM_{\rm add} \quad = \quad \sqrt{c_0^2 + \{c_{\rm 1s}(t-t_0) + c_{\rm 1o}\}^2 E + \{c_{\rm 2s}(t-t_0) + c_{\rm 2o}\} E^2} \tag{3.6}$$

where t_0 is the time at the launch and c_0, $c_{\rm 1s}$, $c_{\rm 1o}$, $c_{\rm 2s}$, $c_{\rm 2o}$ are parameters larger than 0. The obtained model is also shown in Figure 3.14 by the solid line.

Contamination

Figure 3.15 shows spectra of RX J1856.5−3754 observed in every six months. We can see significant degradation of the detection efficiency below 1 keV. It is caused by the absorption due to contaminating materials accumulated on the OBF, which is cooler than the other part

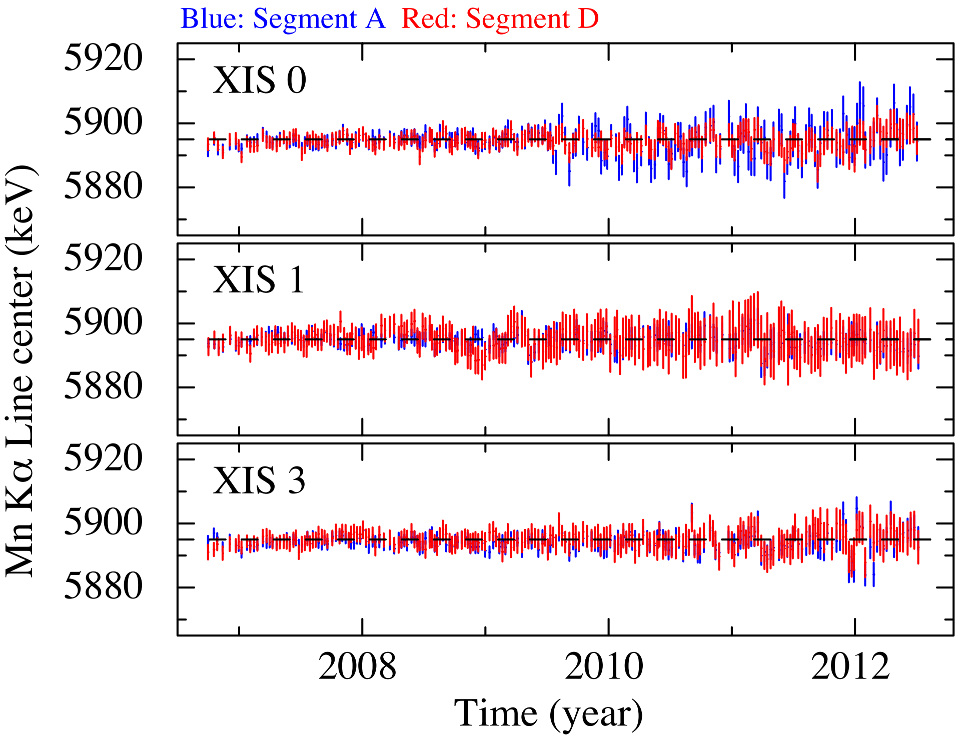

Figure 3.13. Time variability for the line center of the Mn Kα line (^{55}Fe calibration source) after the CTI correction. The top, middle, and bottom panels indicates XIS0, XIS1, and XIS3, respectively.

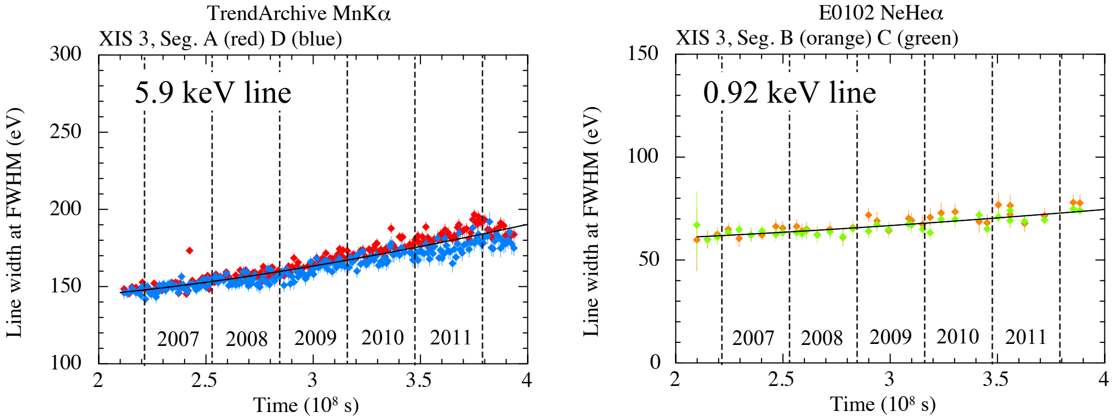

Figure 3.14. Time variability for the line width of (a) Mn Kα line and (b) He-like Ne Kα line after the CTI correction. The solid lines show models of the line width.

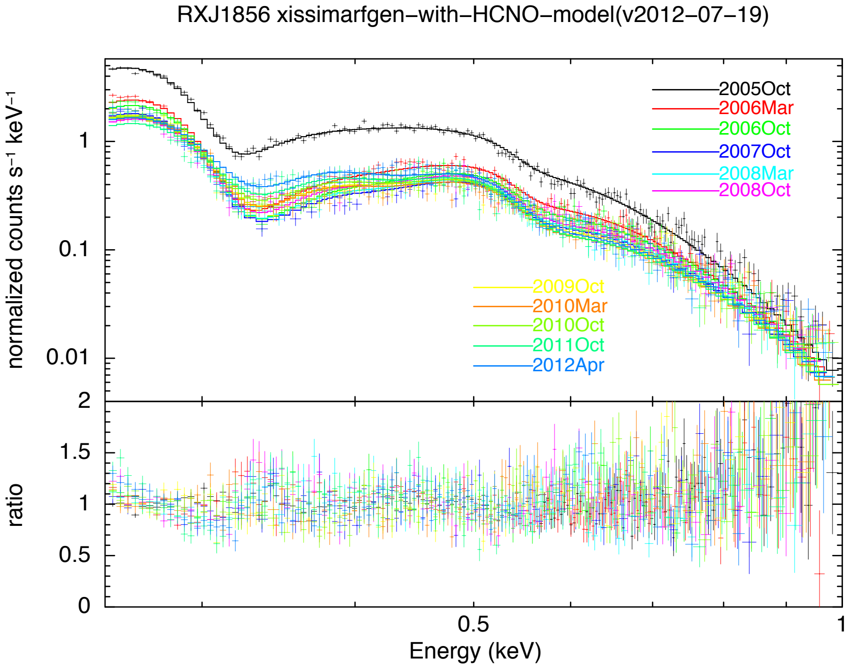

Figure 3.15. XIS spectra of RX J1856.5−3754 observed from 2005 Oct. to 2012 Apr.

of the satellite. Therefore, absorption column density and chemical composition of the contamination are measured using the observation data of RX J1856.5−3754, PKS 2155−304, and 1E 0102.2−7219. The resultant optical depth as a function of time is shown in Figure 3.16. For 0.65 keV X-rays, the detection efficiency is 0.25 times of that at just after launch.

Non X-ray background

In the orbit, comic-rays produce background signals, the so-called the non X-ray background (NXB). Most of the NXB is due to direct ionization loss of cosmic-rays. Such events make long tailed images, and thus they are eliminated by the imaging analysis referred to as the grade selection. However, fluorescence X-rays generated by the interaction between cosmic-rays and the camera body of the XIS are not distinguished from the celestial X-rays.

Figure 3.17 shows the NXB spectra after the grade selection. We can see fluorescence X-rays of Al, Si, Ni, and Au, which are used for the camera components. There are also Mn K shell emission lines coming from the ^{55}Fe calibration source. The constant components are due to Compton events. The large bump-like feature is also seen in the XIS1 spectrum. It is due to low-energy comic-rays.

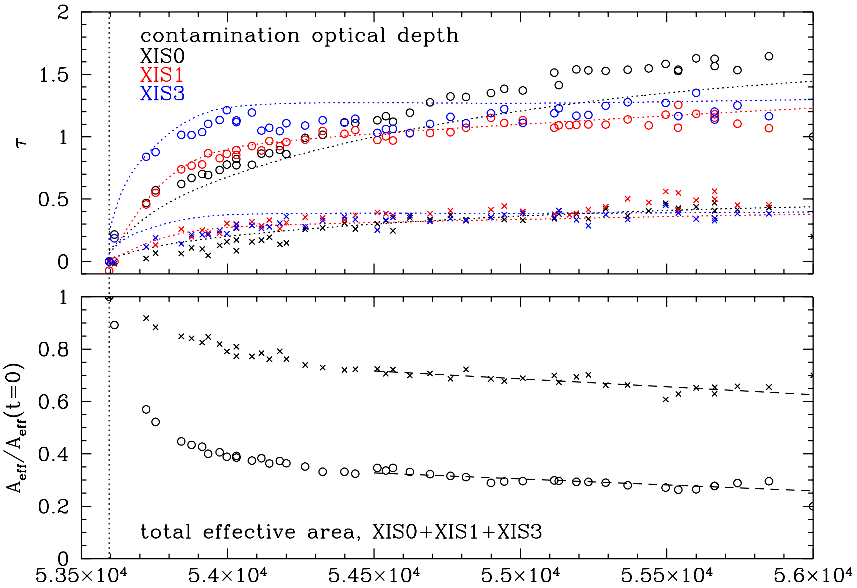

Figure 3.16. Optical depth of the contamination material measured by the calibration observations.

3.4 Advantage of *Suzaku* in the GC survey

The main advantage of the XIS in *Suzaku* is the several factors smaller and more stable NXB than the ACIS in *Chandra* (Garmire et al. 2003) or the EPIC in *XMM-Newton* (Turner et al. 2001). Combined with its large effective area and good energy resolution, the XIS has a unprecedented capability to detect diffuse and faint X-ray emissions. Therefore, *Suzaku* is the most suitable to explore a relics of past GC activity which is concealed by the GCXE or GRXE.

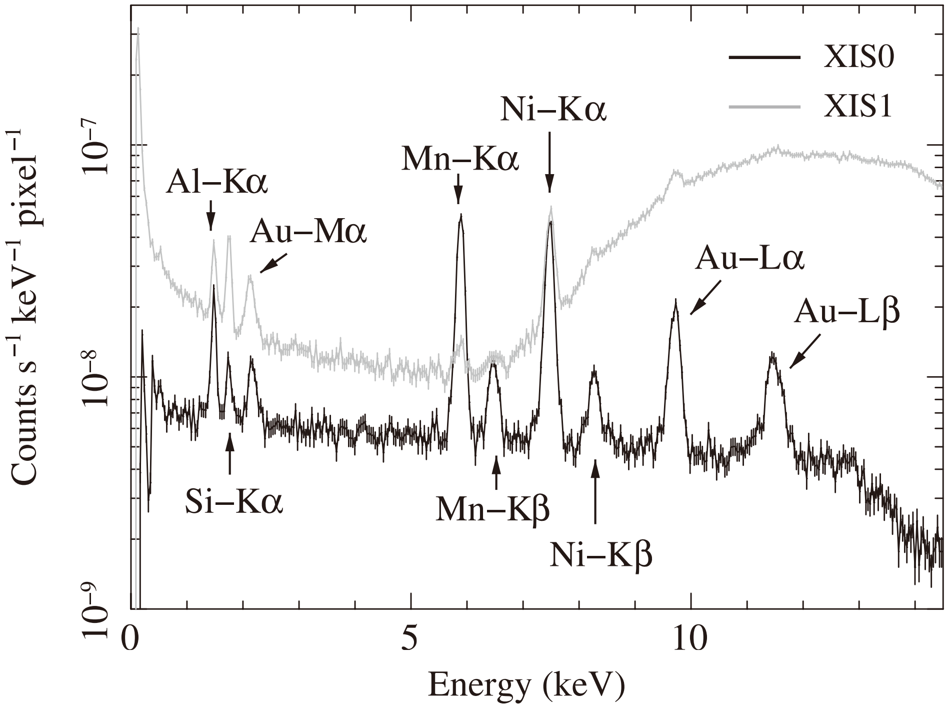

Figure 3.17. Spectra of the non X-ray background derived from XIS0 (the thick line) and XIS1 (the thin line).

Chapter 4

X-ray Images of the South and North of the GC

As described in Chapter 2, previous X-ray studies on the GC have predominantly focused on the Galactic plane region ($|b| < 0^\circ\!.5$), and paid less attention to the off-plane region ($|b| > 0^\circ\!.5$). In order to open up this frontier, we performed *Suzaku* observations of the off-plane region. Using the obtained data, we constructed X-ray images covering a few hundreds parsecs of the GC region (Section 4.1). Since some regions have not been observed by *Suzaku* yet, we also analyzed archival survey data taken by *ASCA* for a supplement (Section 4.2).

Contents

4.1 *Suzaku* X-ray Images of the Galactic Center

4.1.1 Observations and data reduction

We observed the GC region with *Suzaku* from 2005 to 2012. The XIS was operated in the normal clocking mode without either the window nor burst options. The SCI technic was applied for observations taken after 2006 October.

We used the software package HEASoft version 6.12 for data reduction. After reprocessing the data with the calibration database released in 2011 October 10, we removed events taken during the South Atlantic Anomaly passages, night-Earth elevation angles below 5°, and day-Earth elevation angles below 20°. The entire region of XIS2 and the Segment A of XIS0 have not been functional because of anomalies in 2006 November and 2009 June, respectively. These disabled regions were eliminated in the following analysis.

4.1.2 Construction of X-ray images

We made mosaic images of the GC region using the XIS data. A raw-data image in the selected energy band was derived from each observational data. The NXB images were compiled by `xisnxbgen`. In order to correct difference of a exposure time and the vignetting effect, we constructed a exposure map of each observation using the ray-trace simulator, `xissim`. We then reprojected the assembled raw images, NXB images, and exposure maps of all the observations on a reference frame centered at $(l,\ b) = (0\overset{\circ}{.}0,\ -1\overset{\circ}{.}0)$, individually. After subtracting the tiled NXB image from the tiled raw image, we divided it by the tiled exposure map. The data of all CCDs were co-added to increase photon statistics. Image pixels were binned with 12×12 and smoothed with a Gaussian kernel of $\sigma = 48''$.

Figure 4.1 shows the obtained images in the 0.5–1.0 keV (soft), the 1.0–3.0 keV (middle), and the 5.0–8.0 keV (hard) band. Sgr A* is located at the center of the images, $(l,\ b) = (-0\overset{\circ}{.}056,\ -0\overset{\circ}{.}046)$. In the Galactic plane of the middle and hard bands, we see bright emissions consisting of the GCDX, SNR candidates, and point sources artificially extending due to the PSF of the XRT. Contrastingly in the soft band, on-plane region is dim because of strong interstellar absorption toward the GC direction ($N_{\rm H} \sim 6 \times 10^{22}$ cm^{-2}).

We then focused on the off-plane region in the soft and middle band images. We found large extended emission to the $\sim 1\overset{\circ}{.}5$ south of Sgr A*, which is not seen in the hard band. In order to confirm this excess quantitatively, we made projections of the middle band image along $l = 0\overset{\circ}{.}0$ (source) and along $l = -1\overset{\circ}{.}5$ (reference). The obtained profiles are shown in Figure 4.2. The surface brightness of the source region is about 5 times larger than that of the reference region at $b \sim -1.5$, whereas consistent with the reference region beyond $b = -2\overset{\circ}{.}0$. Therefore, this excess is not apparent due to low extinction in the off-plane

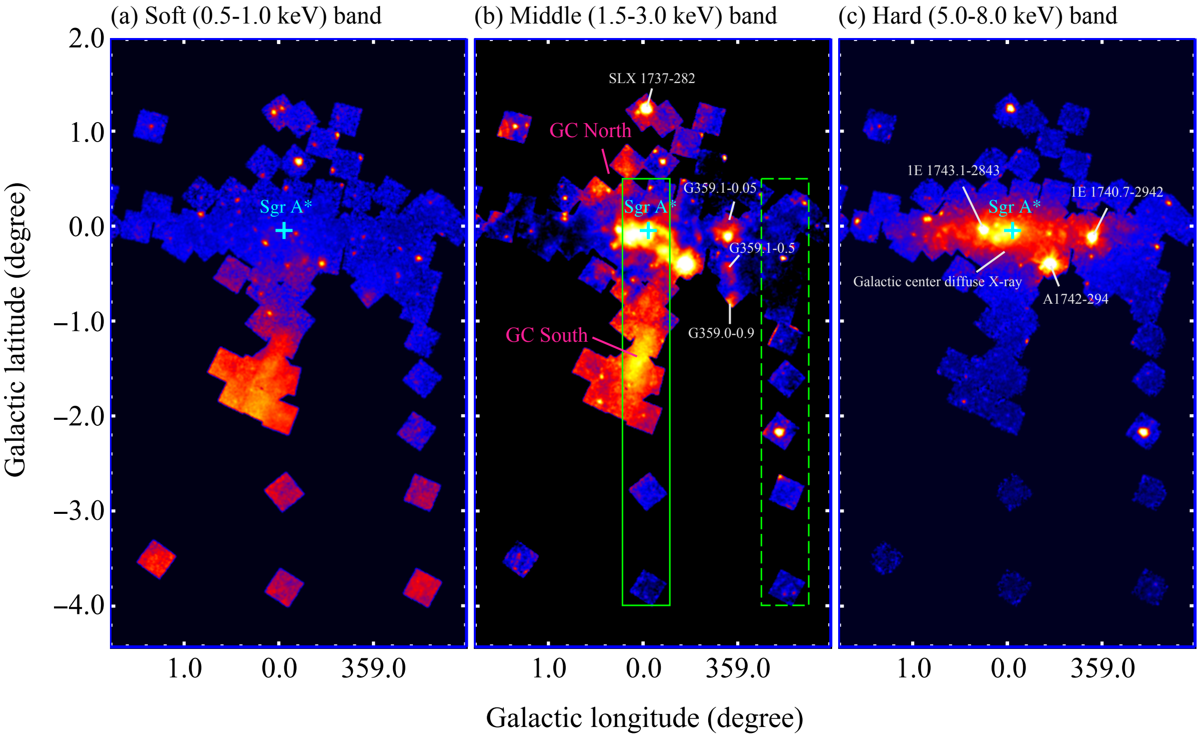

Figure 4.1. *Suzaku* X-ray images of the GC region in the (a) soft (0.5–1.0 keV), (b) middle (1.0–3.0 keV), and (c) hard (5.0–8.0 keV) bands. The projections shown in Figure 4.2 were extracted from the the green solid (source) and dashed (reference) rectangles. Some cataloged sources are labeled in white. The emissions analyzed in the following chapters are labeled in magenta.

region. It is identical with the plume like excess in the *ROSAT* all sky survey reported by Wang (2002). Hereafter, we refer to this emission as "GC South". Detailed spectral analysis of GC South is performed in Chapter 5.

We also found a strong extended emission near $(l,\ b) = (0\overset{\circ}{.}3,\ 0\overset{\circ}{.}5)$ in the middle band. It seems to be a counterpart to GC South, but limited *Suzaku* FOVs make it difficult to identify the overall morphology of the emission. This excess is not seen in either the soft nor hard band.

4.2 *ASCA* X-ray Image of the Galactic Center

The 5° × 5° field in the GC region was surveyed by the Gas Imaging Spectrometers (GIS) onboard *ASCA* (Tanaka et al. 1994) as reported in Sakano et al. (2002). Details of the observations are summarized in that paper. In order to clarify the overall morphology of the off-plane emissions seen in the *Suzaku* images, we reanalyzed the GIS image composed by

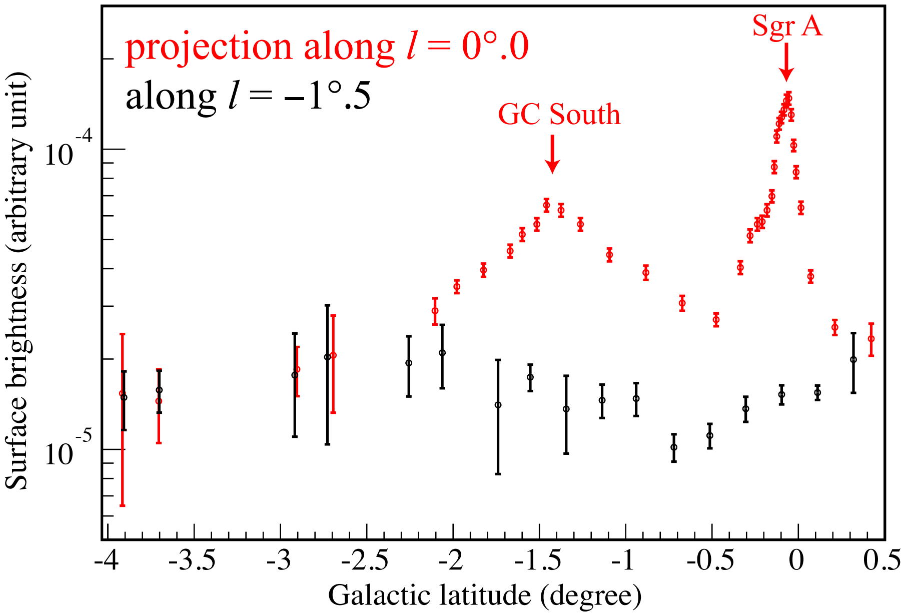

Figure 4.2. Projections of the middle band image extracted from the source (red) and reference (black) regions. The source and background region are along $l = 0\overset{\circ}{.}0$ along $l = -1\overset{\circ}{.}5$, respectively (see Figure 4.1).

Sakano et al. (2002).

Figure 4.3(a) shows the 1.5–3.0 keV band image taken by the GIS/*ASCA*. Although photon statistics and spatial resolution are poorer than the *Suzaku* data, overall features are consistent with that in the *Suzaku* middle band image. We discovered not only GC South but also diffuse emission extending toward the north of Sgr A*, which is partially seen in the *Suzaku* image. These emissions show a S-shaped morphology and seemed to connect near Sgr A*.

In order to quantitatively evaluate this northern excess, we derived projections of the image along $l = 0\overset{\circ}{.}25$ (source) and $l = -0\overset{\circ}{.}75$ (reference) as shown in Figure 4.3(a). The obtained profiles are shown in Figure 4.3(b). We excluded the range of $b = 1\overset{\circ}{.}2$–$1\overset{\circ}{.}3$ in the source projection, because there is a bright point source, SLX 1737−282. We found that surface brightness of source region at $b \sim 0\overset{\circ}{.}5$ is larger than that of the reference region by a factor of 2. Therefore, this excess is also not apparent due to low extinction. Hereafter, we refer to this excess as "GC North". Detailed spectrum analysis of GC North is described in Chapter 6.

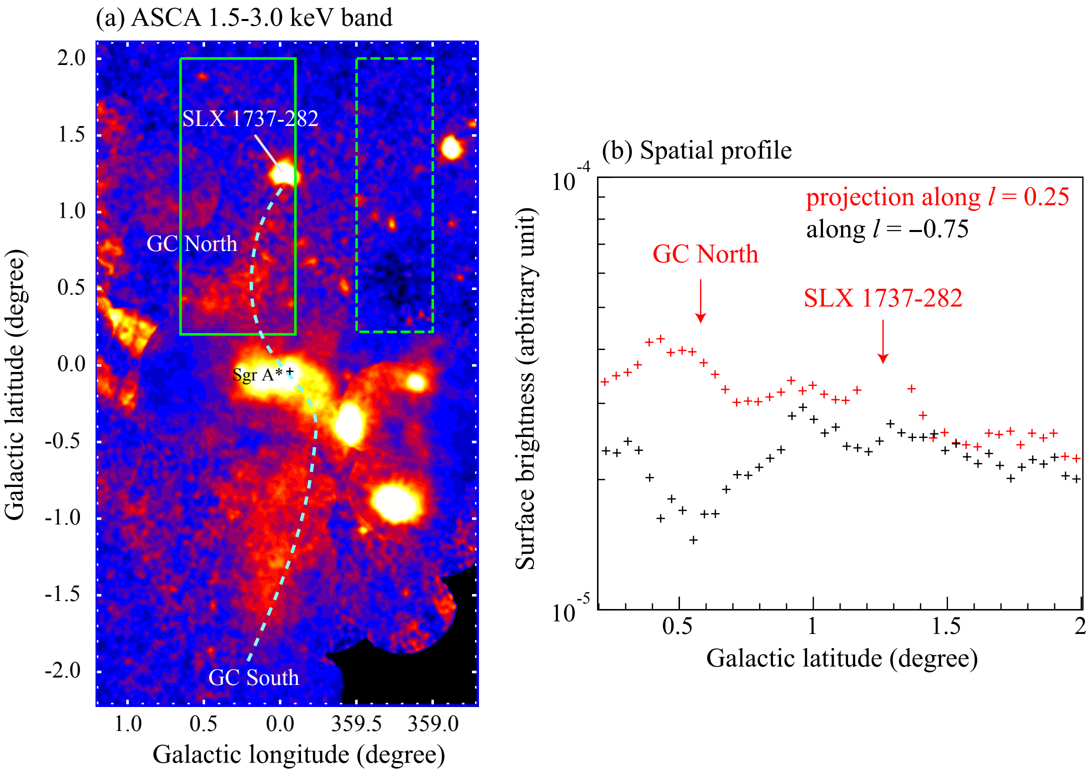

Figure 4.3. (a) *ASCA* X-ray image of the GC region in the 1.5–3.0 keV band. Sgr A* is located at the center of the image and indicated by the cross point. The dotted S-shaped curve is a guide-eye of GC North and GC South. The solid and dotted green rectangles shows the projection extracted regions. (b) Spatial profile of the image. The red data is along $l = 0\overset{\circ}{.}25$ (the solid rectangle in (a)), which includes GC North, and the black data is along $l = -0\overset{\circ}{.}75$ (the dotted rectangle in (a)). The bright point source, SLX 1737−282, is excluded from the red data.

Chapter 5

Analysis on GC South

In the previous chapter, we found the large diffuse emission extending toward the south of Sgr A*. The nature and origin of this emission have not been uncertain. In this chapter, we present the spectral analysis using *Suzaku* data, which provide us sufficient photon statistics to address this question.

Contents

5.1 Analysis Method

The close-up view of the GC South area are shown in Figure 5.1 to declare the analysis region. Spectrum analysis in this section was performed by three steps. We first estimated the Galactic X-ray background (BG) using the reference regions (white squares in Figure 5.1). We then analyzed the brightest region (green rectangle in Figure 5.1(b)) to reduce contamination of the BG and to derive precise physical properties of GC South. Finally, we divided the broad area into ten annuli as shown in Figure 5.1(a), and investigated spatial variations of plasma parameters based on the analysis of the brightest region. Logs of the observations used in this chapter are summarized in Table 5.1.

We used the SPEX software version 2.04.00 (Kaastra et al. 1996) in our spectral analysis. Redistribution matrix files (RMFs) and ancillary response files (ARFs) were generated by `xisrmfgen` and `xissimarfgen`, respectively. Spectral data of XIS0 and XIS3 (FIs) were co-added since they have nearly the same responses. The energy band affected by the contamination (<0.7 keV) and that around the neutral Si K-shell edge (1.7–1.8 keV) were ignored because of calibration uncertainties.

5.2 Background Estimation

X-ray sources in the GC region are affected by the strong Galactic BG, whose X-ray flux depends on position with various components. Thus, careful evaluation of the BG emission is essential. Uchiyama et al. (2011, 2013) extensively studied this emission with *Suzaku*, and determined the spatial distribution along the Galactic latitude and longitude. On the basis of the spatial distribution, the authors divided the BG emission into two components: the GCXE and the GRXE (see Section 2.2.2). Uchiyama et al. (2013) reported that the GCXE is elliptical with a size of $\sim 0\overset{\circ}{.}6 \times 0\overset{\circ}{.}3$ while the GRXE is at least one order of magnitude larger scale. Therefore, GC South is located in the region where contributions from the GRXE are dominant.

We extracted X-ray spectra from the four reference regions shown in Figure 5.1 (Ref 1–4). These spectra exhibit many emission lines of various elements that are typical of the GRXE. We therefore constructed a BG model spectrum based on the GRXE model reported by Uchiyama et al. (2013). The model includes a high temperature plasma component (HP), a low temperature plasma component (LP), and a foreground emission component (FE), all of which are modeled by collisional ionization equilibrium (CIE) plasmas. Although the FE consists of 0.59 keV and 0.09 keV plasmas in the study of Uchiyama et al. (2013), we applied a single ∼0.59 keV plasma because the contribution of the 0.09 keV plasma is negligible in the energy range used in our analysis (0.7–10 keV). Free parameters are the temperatures

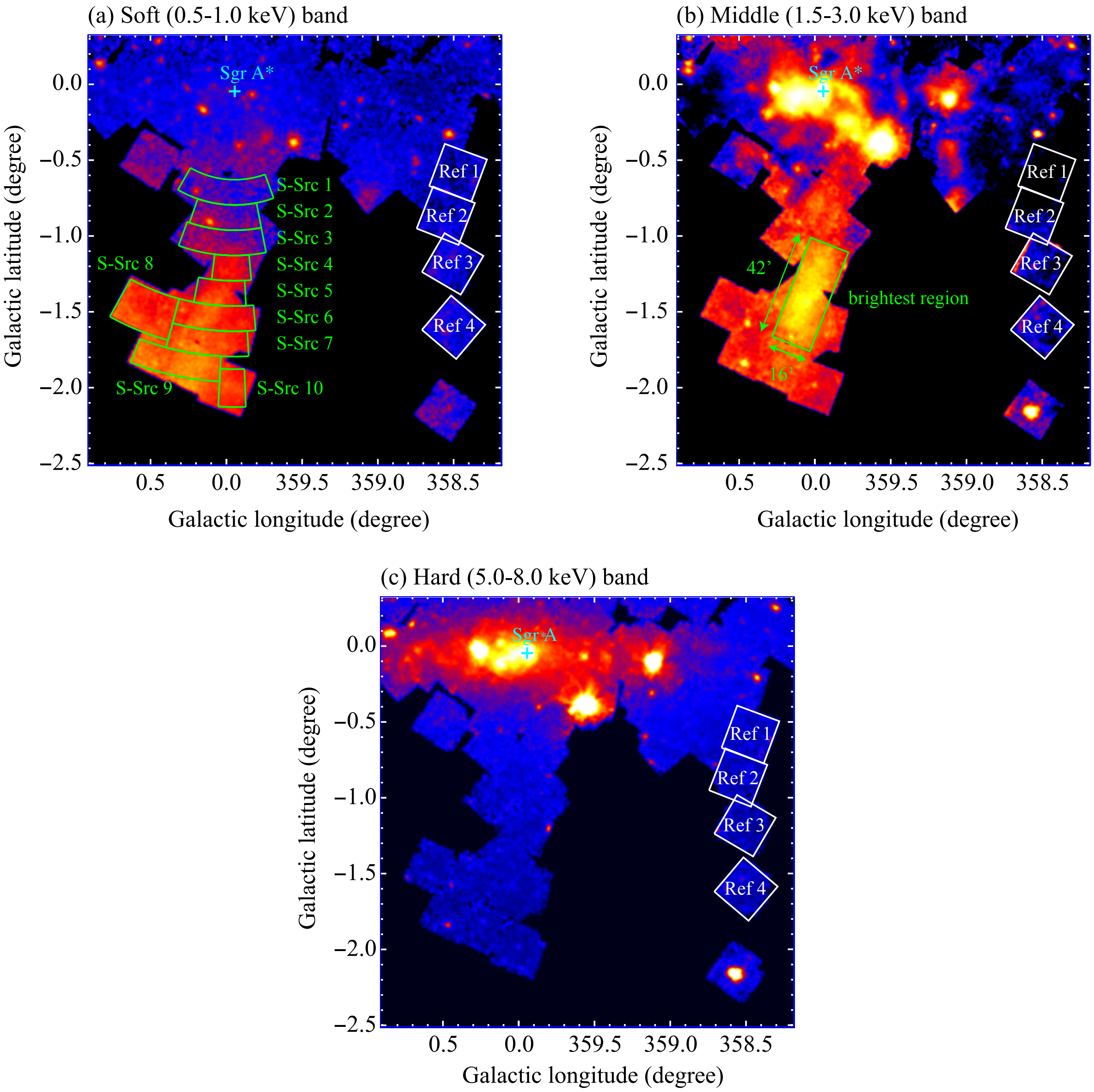

Figure 5.1. X-ray mosaic images of the close-up view of the GC South region. (a) Soft band image. The spectrum extracted regions for the spatially resolved analysis are shown in the green annuli (see Section 5.3.2). (b) Middle band image. The green square shows the brightest part of GC South, where we extracted a spectrum in the analysis of Section 5.3.1. (c) Hard band image. In all the images, the cyan cross indicates the position of Sgr A*, and the white squares are reference regions used to estimate the BG spectrum (see Section 5.2).

Table 5.1. Observation logs of the GC South region.

Sequence #	Aim Point				Obs. Date	Exposure	Obs. Name
	$\alpha_{2000.0}$	$\delta_{2000.0}$	l	b	(yyyy-mm-dd)	(ks)	
			Source regions				
502002010	267.°16	−29.°14	0.°17	−0.°67	2007-10-09	23	GC14
502003010	266.°96	−29.°42	359.°84	−0.°67	2007-10-10	21	GC15
502004010	267.°48	−29.°31	0.°17	−1.°00	2007-10-10	20	GC16
502005010	267.°29	−29.°60	359.°83	−1.°00	2007-10-11	21	GC17
502059010	268.°38	−29.°96	0.°05	−2.°00	2007-09-29	118	GALACTIC BULGE
503081010	268.°05	−29.°76	0.°03	−1.°65	2009-03-09	59	GC(0,-1.6)
504050010	267.°86	−29.°58	359.°21	−1.°95	2010-03-06	100	L,B=0.107,-1.425
504088010	267.°22	−29.°37	0.°00	−0.°83	2009-10-14	47	GALACTIC_BULGE1
504089010	267.°56	−29.°60	359.°95	−1.°21	2009-10-09	55	GALACTIC_BULGE2
505078010	267.°95	−29.°80	359.°95	−1.°60	2011-03-04	51	GALACTIC_BULGE3
507016010	266.°98	−29.°07	0.°15	−0.°50	2012-09-16	103	RADIO_ARC_SOUTH
507017010	267.°19	−28.°77	0.°50	−0.°50	2012-09-29	54	RADIO_ARC_S_E
507018010	266.°77	−29.°37	359.°80	−0.°50	2012-09-30	51	RADIO_ARC_S_W
507028010	268.°10	−29.°48	0.°30	−1.°55	2012-09-20	52	GC_SOUTH_1
507029010	268.°37	−29.°71	0.°22	−1.°87	2012-09-22	52	GC_SOUTH_2
507030010	268.°18	−29.°20	0.°57	−1.°47	2012-10-05	52	GC_SOUTH_3
507031010	268.°41	−29.°45	0.°46	−1.°77	2012-10-06	53	GC_SOUTH_4
			Reference regions				
504002010	266°.06	−30°.55	358.°46	−0.°59	2010-02-27	53	HESSJ1745-303B
504003010	266°.39	−30°.62	358.°56	−0.°87	2010-02-25	51	HESSJ1745-303C
504090010	266°.68	−30°.83	358.°51	−1.°19	2009-10-13	41	GALACTIC_BULGE7
504091010	267°.09	−31°.05	358.°50	−1.°60	2009-09-14	51	GALACTIC_BULGE8

($kT_{\rm HP}$, $kT_{\rm LP}$, $kT_{\rm FE}$) and the emission measures ($EM_{\rm HP}$, $EM_{\rm LP}$, $EM_{\rm FE}$) of the HP, LP, and FE. The metal abundances relative to solar values (Anders & Grevesse 1989) were common between the HP and LP. Those of Mg, Si, S, Ar, Ca, and Fe were free parameters while the Ne and Ni abundances were linked to Mg and Fe, respectively. The other elements were fixed to the solar values. In the FE, the metal abundances of Ne and Mg were free parameters while those of the other elemetns were linked and allowed to vary. In order to reproduce the Fe I Kα emission in the spectra, we also added a Gaussian component with a fixed line centroid of 6.4 keV. The continuum emission associated with the Fe I Kα emission was included in the HP. In addition, we need to include the cosmic X-ray background (CXB) even though its contribution is small. The CXB was represented by a single power-law function with a photon index and surface brightness (2–10 keV) of 1.41 and 6.38×10^{-8} erg cm^{-2} s^{-1} sr^{-1}, respectively (Kushino et al. 2002). The explicit form of our BG model is therefore

$$A_{\rm GC} \times ({\rm HP} + {\rm LP} + {\rm Gaussian}) + A_{\rm FE} \times {\rm FE} + (A_{\rm GC})^2 \times {\rm CXB}, \tag{5.1}$$

where A$_{\rm GC}$ (column density of $N_{\rm H\,GC}$) and A$_{\rm FE}$ (column density of $N_{\rm H\,FE}$) represent the interstellar absorptions toward the GC and for the FE component, respectively. The absorption

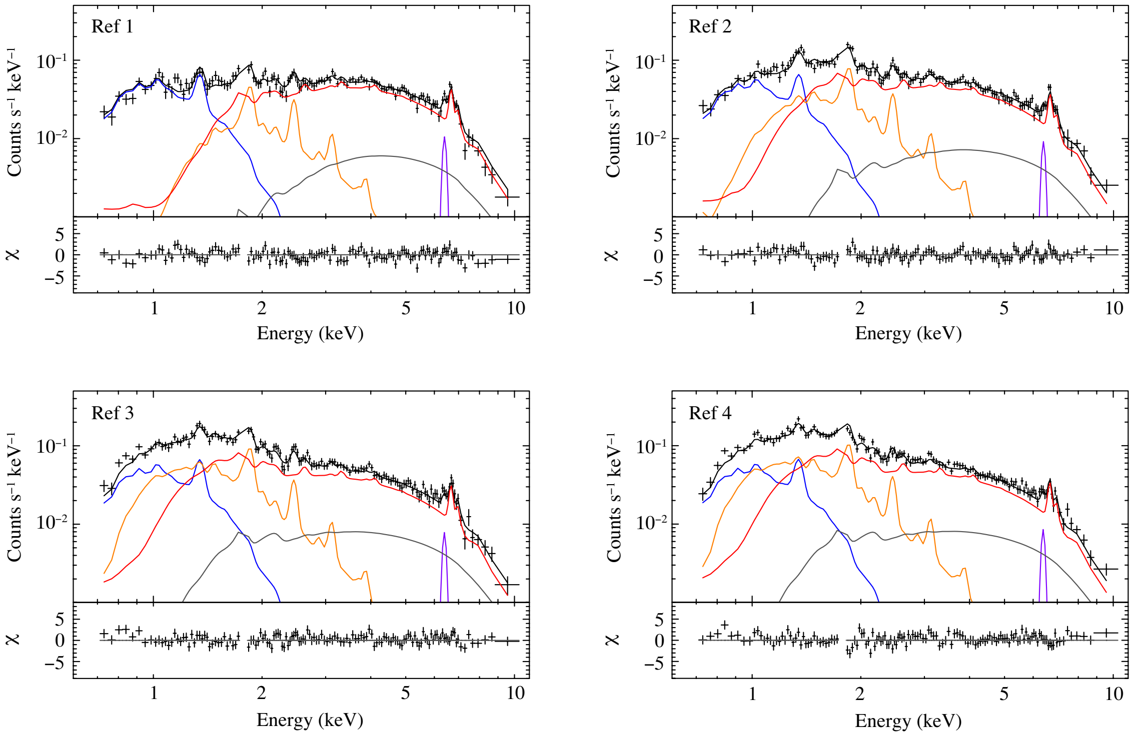

Figure 5.2. Spectra and the best-fit models of reference regions. Only the co-added FI spectra and models are displayed for visibility, although the FI and BI spectra were simultaneously fitted. The red, orange, purple, blue, and gray lines represent the HP, LP, Gaussian, FE, and CXB, respectively (see text).

for the CXB is twice that of $N_{\mathrm{H\,GC}}$, because the CXB is of extragalactic origin behind the GC region.

We simultaneously fitted the reference-region spectra with this model. Since the flux in the term (HP + LP + Gaussian) depends on the position as shown in Uchiyama et al. (2013), we multiplied by a constant factor as

$$A_{\mathrm{GC}} \times (\mathrm{HP} + \mathrm{LP} + \mathrm{Gaussian}) \times factor, \tag{5.2}$$

where $factor$ for Ref 1 was fixed to 1, and those for the other regions were free parameters. The $N_{\mathrm{H\,GC}}$ values were also independently allowed to vary while the other parameters were common among the regions. As a result of our fitting, the spectra were well reconstructed with $\chi^2/\mathrm{d.o.f} = 1415/1107$. The best-fit models and parameters are shown in Figure 5.2 and Table 5.2, respectively. We note that the HP, LP and FE parameters are slightly different from those of Uchiyama et al. (2013). This is due to the difference of the models and selected regions; the GRXE spectrum of Uchiyama et al. (2013) is a composite from the on-plane regions of $|l| > 2^{\circ}\!\!.0$ and $|b| < 0^{\circ}\!\!.5$, while our BG regions are far from the plane of

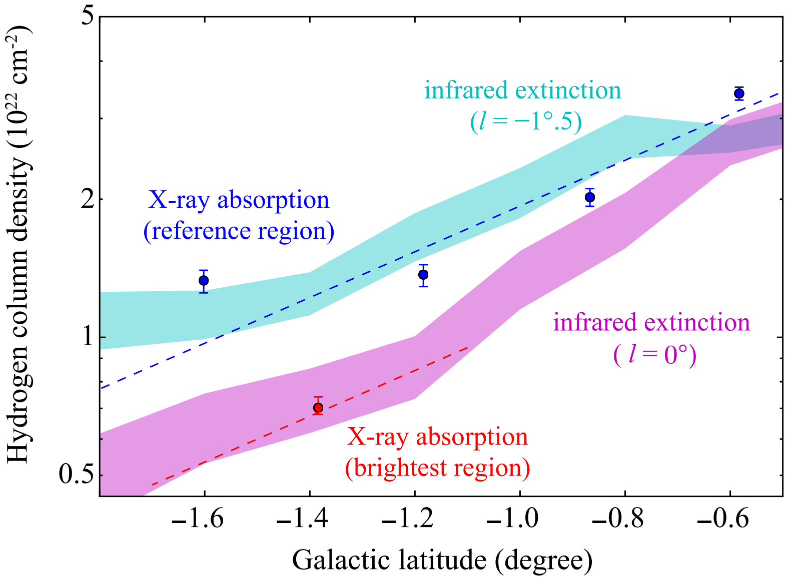

Figure 5.3. Profile of the absorption column density. The blue circles indicate $N_{\mathrm{H\,GC}}$ obtained from the best-fit values of the reference regions. The blue broken line is the exponential-folding model of $N_{\mathrm{H\,GC}}$ (see text). The blue and red shaded areas show the near-infrared extinctions (A_{K_s}) including the errors along $l = -1^{\circ}.5$ and $l = 0^{\circ}$, respectively (Gonzalez et al. 2012). The near-infrared extinctions were converted to N_{H} with a scaling factor of $N_{\mathrm{H}}/A_{K_s} = 1.8 \times 10^{22}$ cm^{-2} mag^{-1}. The red circles indicate the fitting results of the spatially resolved source spectra.

$l = -1^{\circ}\!.4$ and $-1^{\circ}\!.6 < b < -0^{\circ}\!.6$. One might claim that the abundances of some elements are significantly smaller than the solar values. We approximated the BG spectra using simplified plasma models based on the GRXE model near the GC (Uchiyama et al. 2013). In the Galactic bulge regions (our observation fields) however, the possible contribution of unresolved faint point sources (e.g. Revnivtsev et al. 2009), CXB fluctuation (Kushino et al. 2002), or unknown non thermal emissions may not be ignored. These sources increase the continuum flux in the BG spectrum, and hence reduce the apparent abundances. In order to verify this possibility, we fitted the spectra by fixing the abundances of all the elements in the relevant plasma models (LP, HP, and FE) to the solar values, and adding two power-law components; one is convolved with A_{GC}, and the other is convolved with A_{FE}. Then we obtained a reasonable fit (χ^2/d.o.f = 1654/1116) with no significant change for all the parameters in Table 5.2.

The best-fit *factor* values decrease with increasing the Galactic latitude (b) with an exponential-folding scale of $3^{\circ}\!.3 \pm 0^{\circ}\!.8$, which is roughly consistent with those of Uchiyama

Table 5.2. Fitting results of the spectra in the reference regions.

Parameter (Unit)	Ref 1	Ref 2	Ref 3	Ref 4
— HP + LP + Gaussian —				
$N_{\mathrm{H\,GC}}$ (10^{22} cm^{-2})	3.40 ± 0.11	2.02 ± 0.09	1.37 ± 0.08	1.33 ± 0.08
$factor$	1 (fixed)	0.85 ± 0.03	0.71 ± 0.02	0.77 ± 0.02
kT_{HP} (keV)	$7.6^{+0.4}_{-0.3}$			
kT_{LP} (keV)	0.69 ± 0.03			
EM^{*}_{HP} (10^{58} cm^{-3})	0.38 ± 0.01			
EM^{*}_{LP} (10^{58} cm^{-3})	$0.45^{+0.09}_{-0.08}$			
Mg = Ne (solar)	$0.43^{+0.14}_{-0.12}$			
Si (solar)	$0.94^{+0.17}_{-0.14}$			
S (solar)	1.6 ± 0.3			
Ar (solar)	3.5 ± 0.8			
Ca (solar)	2.8 ± 1.0			
Fe = Ni (solar)	0.53 ± 0.04			
Other Elements (solar)	1 (fixed)			
Fe I Kα flux (10^{-6} ph cm^{-2} s^{-1})	6.4 ± 1.2			
— FE —				
$N_{\mathrm{H\,FE}}$ (10^{22} cm^{-2})	0.42 ± 0.01			
kT_{FE} (keV)	0.33 ± 0.04			
EM^{*}_{FE} (10^{58} cm^{-3})	$0.86^{+0.66}_{-0.33}$			
Ne (solar)	0.06 ± 0.02			
Mg (solar)	$0.19^{+0.05}_{-0.04}$			
Other Elements (solar)	$0.022^{+0.014}_{-0.009}$			

Notes:
[*] Emission measure assuming the distance of 8 kpc. $EM = \int n_{\mathrm{e}} n_{\mathrm{p}} dV$, where n_{e}, n_{p}, and V , are the electron density, the proton density, and the emitting volume, respectively.

et al. (2013). The $N_{\mathrm{H\,GC}}$ values also decrease with b, as phenomenologically given by

$$N_{\mathrm{H\,GC}} = 6.1 \pm 0.7 \times 10^{22} \exp\left(-\frac{|b|}{0^{\circ}\!.87 \pm 0^{\circ}\!.10}\right) \mathrm{cm}^{-2}. \tag{5.3}$$

This model and the best-fit $N_{\mathrm{H\,GC}}$ are plotted in Figure 5.3 by the blue broken line and circles, respectively. We compared these data with the near-infrared extinction (A_{K_s}) of the stars located in the GC (Gonzalez et al. 2012). The mean $A_{K_s}$and best-fit $N_{\mathrm{H\,GC}}$ in the region of $-1^{\circ}\!.6 < b < -1^{\circ}\!.2$ are 0.76 mag and 1.35×10^{22} cm^{-2}, respectively. Thus, a conversion factor $N_{\mathrm{H}}/A_{K_{\mathrm{s}}}$ was estimated to be 1.8×10^{22} cm^{-2} mag^{-1}, which is within the range reported in the literature (e.g., van den Berg et al. 2009; Güver & Özel 2009). With this conversion factor, the A_{K_s}profile is superimposed on Figure 5.3 as the blue shaded area. We confirmed that the $N_{\mathrm{H\,GC}}$ model well follows the over-all trend of the A_{K_s}profile.

Figure 5.3 also shows A_{K_s}in the source region ($l = 0^\circ\!.0$) with the red shaded area (Gonzalez et al. 2012). We found that the A_{K_s}in the source region is smaller than that in the reference region by a factor of ∼0.55 in the $-1^\circ\!.6 < b < -1^\circ\!.2$ range. Assuming the same b-dependence as in the reference regions, we estimated $N_{\rm H\,GC}$ in the source region by normalizing Equation (5.3) by a factor of 0.55. This estimated model is shown by the broken red line in Figure 5.3.

5.3 Spectrum Analysis

5.3.1 Brightest region spectrum

We first investigated a spectrum extracted from the brightest region ($42' \times 16'$ rectangular region) in order to increase the signal-to-background ratio and to reveal the precise physical properties. Figure 5.4(a) shows the extracted spectrum. The hard X-ray band above 5 keV is dominated by the BG emission as shown in Figure 5.4(c). In order to subtract these BG components, we applied the BG model with the best-fit values obtained from the reference regions (Section 5.2). Only the surface brightness and $N_{\rm H\,GC}$ for the (HP + LP + Gaussian) component should be different from those in the reference regions. Therefore, $factor$ was treated as a free parameter, and the $N_{\rm H\,GC}$ value was fixed to 0.69×10^{22} cm^{-2}, which is the mean value of the $N_{\rm H\,GC}$ profile in the source regions (the broken red line in Figure 5.3). The parameters for the FE were the same as those in the reference regions.

The BG model with these parameters well reproduced the 5–10 keV band spectrum, but it left a large data excess in the 0.7–5.0 keV band. This excess shows emission lines from highly ionized atoms, and hence is of thermal plasma origin. We then attempted a fitting with a model of combining CIE plasma and the BG model. The free parameters in the CIE plasma were $N_{\rm H}$, kT, and the abundances of the major elements (Ne, S, Si, Ar, and Fe). The abundances of O, Ca, and Ni were linked to those of Ne, Ar, and Fe, respectively. Those of the other elements were fixed to the solar values.

Spectral fitting with the composite model gave a best-fit CIE temperature of $kT =$ 0.62 keV, but failed to reconstruct the data with χ^2/d.o.f = 2617/352 (Figure 5.4(b)). The most prominent residuals in Figure 5.4(b) are the line and bump at 0.8 keV and 1.2–1.3 keV, respectively. These are known to originate from incomplete atomic data for the Fe L-shell complex in the current plasma model. Gu et al. (2007) claimed that the line intensity ratio of 3s→2p (∼0.7 keV) over 3d→2p (∼0.8 keV) for Fe XVIII has an uncertainty. Brickhouse et al. (2000) and Audard et al. (2001) reported that the SPEX plasma code underestimates the flux around 9.6–10.6 Å (1.17–1.29 keV), since some Fe L-shell transitions ($n = 6, 7, 8 \rightarrow 2$ for Fe XVII, $n = 6, 7 \rightarrow 2$ for Fe XVIII, and $n = 6 \rightarrow 2$ for Fe XIX) are missing. We thus

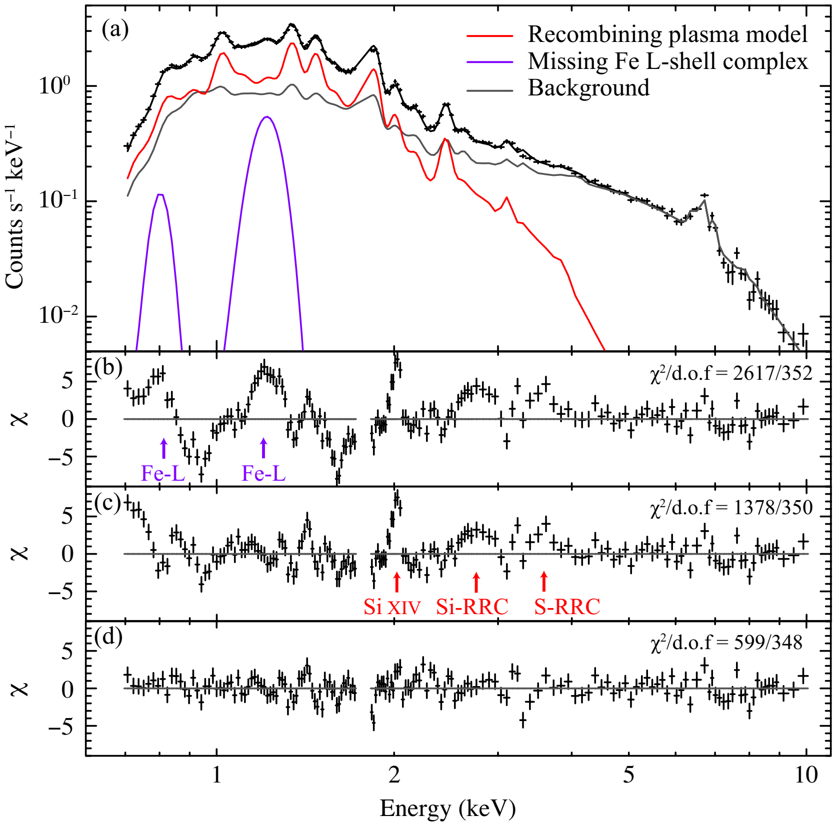

Figure 5.4. (a) Spectrum extracted from the entire source region. Only the co-added FI spectra and the models are displayed for visibility, although the FI and BI spectra were simultaneously fitted. The red, purple, and gray solid lines indicate the best-fit RP model, the missing Fe L-shell lines, and the background model, respectively. The χ^2 values fitted with each model are also shown: (b) CIE plasma model, (c) CIE plasma and additional Fe-L shell transients model, and (d) RP and additional Fe-L shell transients model (best-fit).

phenomenologically added Gaussians at 0.8 keV and 1.2 keV. The FWHM of the 1.2 keV line was fixed to 120 eV to approximate multiple lines. Then, the fit was improved with χ^2/d.o.f = 1378/350, but large residuals still remained (Figure 5.4(c)). We conclude that the CIE model for GC South plasma is invalid.

In Figure 5.4(c), the data excess at 2.0 keV corresponds to Si XIV Kα. This indicates that the CIE model (kT = 0.62 keV) underestimates the ionization state of Si. In addition, we can clearly observe hump-like features around 2.5–3.0 keV and 3.2–3.8 keV. These features are most likely due to the radiative recombination continua (RRCs) of Si and S, which are observed in some Galactic supernova remnants (SNRs; see Sawada & Koyama 2012; Uchida et al. 2012 and references therein). Although the residual of Si XIV Kα can be solved by a multi-temperature CIE model, the RRCs cannot be reproduced.

Table 5.3. Fitting results of the brightest-region spectrum with the `NEIJ` model.

Parameter	Unit	Value
N_{H}	(10^{22} cm^{-2})	0.70 ± 0.03
kT_{e}	(keV)	0.46 ± 0.02
kT_{init}	(keV)	$1.63^{+0.27}_{-0.18}$
nt	(10^{11} s cm^{-3})	5.3 ± 0.5
EM^{*}	(10^{58} cm^{-3})	9.5 ± 1.0
Ne =O	(solar)	$0.39^{+0.05}_{-0.04}$
Mg	(solar)	0.81 ± 0.07
Si	(solar)	0.71 ± 0.05
S	(solar)	$0.79^{+0.09}_{-0.08}$
Ar = Ca	(solar)	$1.9^{+0.6}_{-0.5}$
Fe = Ni	(solar)	0.10 ± 0.02

Notes:
* Emission measure assuming the distance of 8 kpc.

The RRC residuals strongly indicate that the plasma is in the recombining phase. We thus applied a non-equilibrium ionization model (`NEIJ` in SPEX), that successfully reproduces the RRC features observed in the SNRs W44 and G346.6−0.2 (Uchida et al. 2012; Yamauchi et al. 2013). This model traces the evolution of the ionization state when the initial ionization temperature (kT_{init}) and the electron temperature (kT_{e}, assumed to be constant) are given; the following evolution of the ionization state is traced by the relaxation timescale of $n_{\mathrm{e}}t$, where n_{e} and t are the number density of electrons and the elapsed time, respectively. If the best-fit kT_{init} is $\sim$0, then this model describes an ionizing plasma (`NEI` in XSPEC), while if $kT_{\mathrm{init}} > kT_{\mathrm{e}}$, it describes a recombining plasma (RP).

The free parameters in the `NEIJ` model were kT_{init}, kT_{e}, $n_{\mathrm{e}}t$, and the abundances of the major elements (the same as in the CIE fitting). The `NEIJ` model gave a good fit with χ^2/d.o.f = 599/348. The best-fit kT_{init}, kT_{e}, and $n_{\mathrm{e}}t$ are 1.6 keV, 0.46 keV, and 5.3×10^{11} s cm^{-3} , respectively (see Table 5.3). This best-fit model well reproduced the RRC features around 2.5–3.0 keV and 3.2–3.8 keV, as shown in Figure 5.4(d).

For comparison, we list the average charge state of each element in the best-fit `NEIJ` model and that of the CIE at the same electron temperature (Table 5.4). We confirmed that GC South is really an RP.

Table 5.4. Average charge state of each element.

model	Ne	Mg	Si	S	Ar	Fe
best-fit `NEIJ`	9.56	11.1	12.7	14.2	15.7	17.0
CIE ($kT = 0.46$ keV)	9.30	10.3	12.0	13.9	15.6	16.4

Notes: Average charge state of 0 means a neutral atom.

5.3.2 Spatially resolved spectra

We found that the recombining process dominates in the brightest part of the plasma. In order to study the spatial variation of the plasma parameters, we then divided the entire GC South field into ten annual regions as shown in Figure 5.1(a), and extracted their spectra (S-Src 1 to S-Src 10). Bright point sources were excluded to avoid the contamination of them.

The *factor* in the BG model was left free as done in the fitting of the brightest part. The absorption column density ($N_{\rm H\,GC}$) of each region was fixed to the value estimated from A_{K_s}, which is converted by the factor of 1.8×10^{22} cm^{-2} mag^{-1}. We fixed $kT_{\rm init}$ in the `NEIJ` (RP) model to 1.6 keV, while allowed to vary $kT_{\rm e}$ and $n_{\rm e}t$ to study their spatial variation. The elemental abundances were fixed to the best-fit values of the brightest region (Table 5.3). The Fe L-shell lines at ~0.8 keV and ~1.2 keV were not added at first. We individually fitted each spectrum with this model (hereafter the tentative model).

Figure 5.5 shows the fitting results of the S-Src 1–10 spectra with the tentative model. In the S-Src 1-3 spectra, we found large residuals especially in the 0.5-1.0 keV band. One possible cause is the statistical error (~15%) of A_{K_s}, which is used to estimate $N_{\rm H\,GC}$. We attempted to treat $N_{\rm H\,GC}$ as a free parameter in this range but the fits are not improved. Another cause is the spatial fluctuation of the FE flux. Ryu (2013) investigated GCXE spectra in various on-plain regions (Sgr B2, Sgr C, Sgr D, and Sgr E), and reported that the FE fluxes vary within a factor of 2.4. Moreover, we found local excess of Hα emission in this region, which mainly traces the foreground warm matter, from the archival data of *SHASSA* (Gaustad et al. 2001). Therefore, we treated the normalization (emission measure) of the FE component as a free parameter in the fitting of the S-Src 1–3 spectra. Then, the FE fluxes were renormalized by a factor of 2.1–2.6, and spectra in the 0.5–1.0 keV band were represented. These factors are consistent with that reported by Ryu (2013).

In the S-Src 4-10 spectra, we also found Gaussian-like residuals at ~0.8 keV and ~1.2 keV. These are most likely due to the missing Fe L-shell lines as shown in the previous section. Thus, we also added the two Gaussians to the model in the same manner as the fitting of the brightest part (hereafter the modified model).

The modified model fairly improved the fits as shown in Figure 5.6. The obtained parameters and reduced χ statistics are summarized in Table 5.5. The surface brightness in

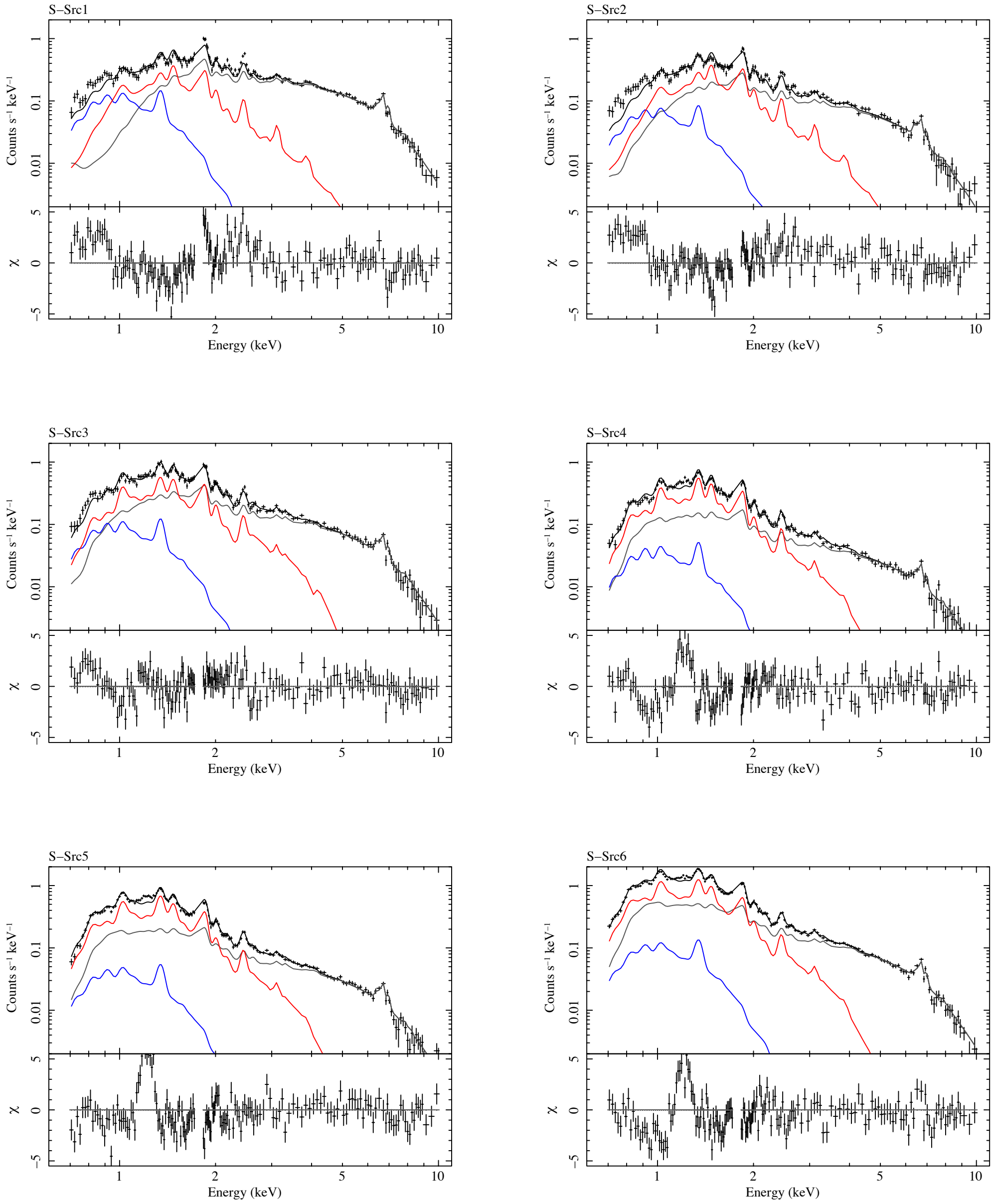

Figure 5.5. Spectra of the S-Src 1–10 regions fitted with the tentative model (see text). Only the co-added FI spectra and models are displayed for visibility, although the FI and BI spectra were simultaneously fitted.

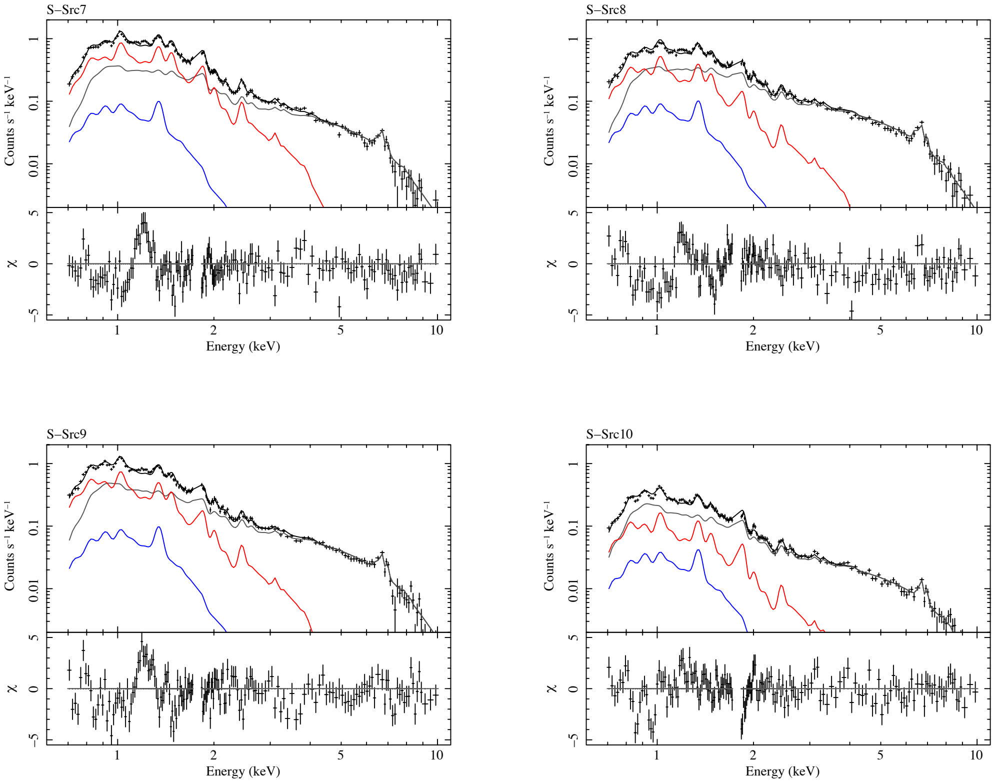

Figure 5.5. *Continued.*

the 5–8 keV band derived from the best-fit of the source and reference regions agrees with the spatial profile composed by Uchiyama et al. (2013). This supports the reliability of our method of the BG estimation and subtraction. In order to investigate the impact of the FE-flux variation on the fitting results of S-Src 4–10, we tried to increase the FE flux by a factor of 2, and confirmed that the best-fit parameters are consistent with that in Table 5.5. Therefore systematic errors due to the spatial variation of the FE flux are negligible in the S-Src 4–10 regions.

We plotted the best-fit $N_{\rm H}$ and estimated $N_{\rm H\,GC}$ on Figure 5.7 as a function of the Galactic latitude, and found that they are reasonably consistent. Figure 5.8(a)–(c) shows spatial distributions of kT, $n_{\rm e}t$, and the surface brightness of the plasma. All these parameters decrease as higher the Galactic latitude. We found that plasmas in S-Src 1–3 are in a CIE state whereas those in S-Src 4–10 are RPs. To evaluate a degree of over-ionization, we calculated the difference of the average ionization state of Si between the best-fit model and the CIE model assuming the obtained kT_e. If the difference becomes a positive value, the plasma is in an over-ionized state (RP). The result is shown in Figure 5.8(d). The degree of over-ionization is marginally increase as higher the Galactic latitude.

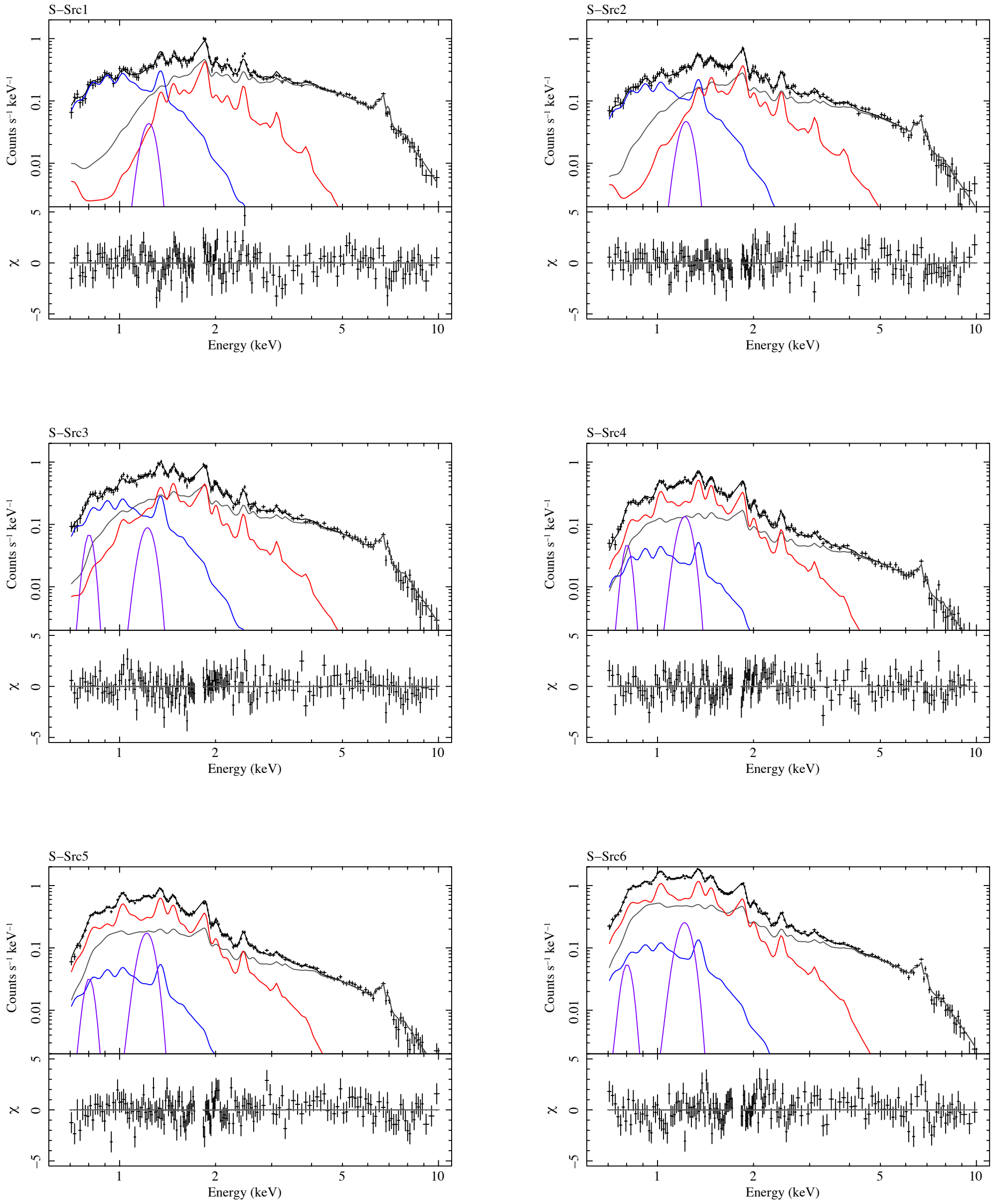

Figure 5.6. Spectra of the S-Src 1–10 regions fitted with the modified model (see text). Only the co-added FI spectra and models are displayed for visibility, although the FI and BI spectra were simultaneously fitted.

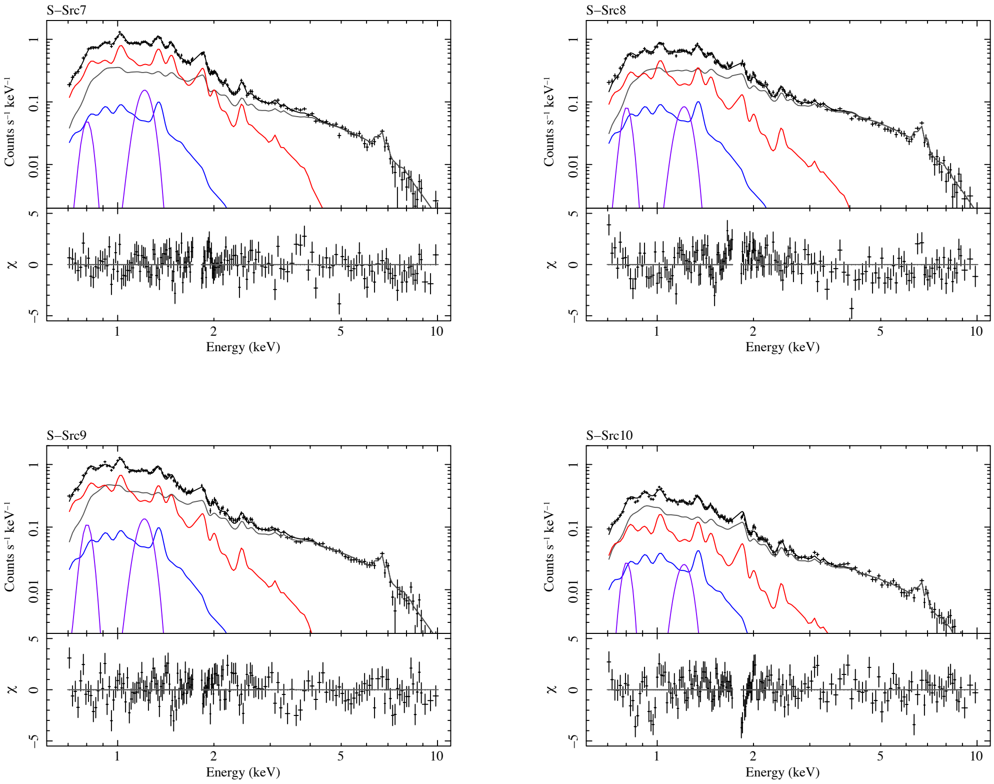

Figure 5.6. *Continued.*

Table 5.5. Fitting results of the spatially resolved spectra with the `NEIJ` model.

Region	$N_{\mathrm{H\,GC}}^{*}$ (10^{22} cm^{-2})	N_{H} (10^{22} cm^{-2})	kT_{e} (keV)	$n_{\mathrm{e}}t$ (10^{11} s cm^{-3})	$EM^{\dagger}$ (10^{58} cm^{-3})	SB‡	FE ratio§	χ^2/dof
S-Src 1	2.31	$3.27^{+0.12}_{-0.16}$	0.63 ± 0.03	> 21	$5.3^{+1.4}_{-0.7}$	$9.0^{+2.4}_{-1.2}$	2.1 ± 0.2	525/328
S-Src 2	1.54	$2.30^{+0.14}_{-0.18}$	0.75 ± 0.04	> 13	$2.3^{+0.4}_{-0.3}$	$6.9^{+1.2}_{-0.9}$	2.6 ± 0.1	399/328
S-Src 3	1.25	$1.53^{+0.17}_{-0.26}$	$0.61^{+0.28}_{-0.12}$	> 4.7	$2.8^{+1.3}_{-1.1}$	$5.4^{+2.5}_{-2.1}$	2.3 ± 0.4	381/328
S-Src 4	0.84	$0.86^{+0.03}_{-0.02}$	$0.50^{+0.02}_{-0.03}$	$6.2^{+0.4}_{-0.5}$	$1.9^{+0.3}_{-0.1}$	$8.3^{+1.3}_{-0.4}$	1 (fix)	415/328
S-Src 5	0.76	0.73 ± 0.02	0.46 ± 0.02	5.8 ± 0.3	2.6 ± 0.2	$8.2^{+0.6}_{-0.6}$	1 (fix)	408/328
S-Src 6	0.65	0.60 ± 0.02	0.48 ± 0.02	5.5 ± 0.3	4.1 ± 0.3	$5.3^{+0.4}_{-0.4}$	1 (fix)	495/328
S-Src 7	0.56	0.48 ± 0.02	0.44 ± 0.02	$4.6^{+0.3}_{-0.2}$	2.5 ± 0.2	$4.1^{+0.3}_{-0.3}$	1 (fix)	417/328
S-Src 8	0.66	$0.36^{+0.04}_{-0.02}$	$0.41^{+0.03}_{-0.06}$	$5.0^{+0.4}_{-0.6}$	$1.1^{+0.36}_{-0.1}$	$1.7^{+0.6}_{-0.1}$	1 (fix)	541/328
S-Src 9	0.46	0.24 ± 0.02	$0.43^{+0.03}_{-0.02}$	4.9 ± 0.4	1.2 ± 0.1	$2.0^{+0.2}_{-0.2}$	1 (fix)	570/328
S-Src 10	0.41	0.36 ± 0.03	0.38 ± 0.03	$5.1\pm^{+0.6}_{-0.5}$	0.39 ± 0.05	$1.4^{+0.2}_{-0.2}$	1 (fix)	552/328

Notes:

kT_{init} and elemental abundances for the `NEIJ` model were fixed to the values listed in Table 5.3.

[*] Absorption column density for the BG emissions that were estimated from the near-infrared extinction investigated by Gonzalez et al. (2012). They were fixed to the listed values.

[†] Emission measure assuming the distance of 8 kpc.

[‡] Absorption-corrected surface brightness in the 0.7–5.0 keV band with a unit of 10^{-14} erg s^{-1} cm^{-2} arcmin^{-2}

[§] Ratio of the FE flux between in the best-fit model and in the original BG model shown in Table 5.2.

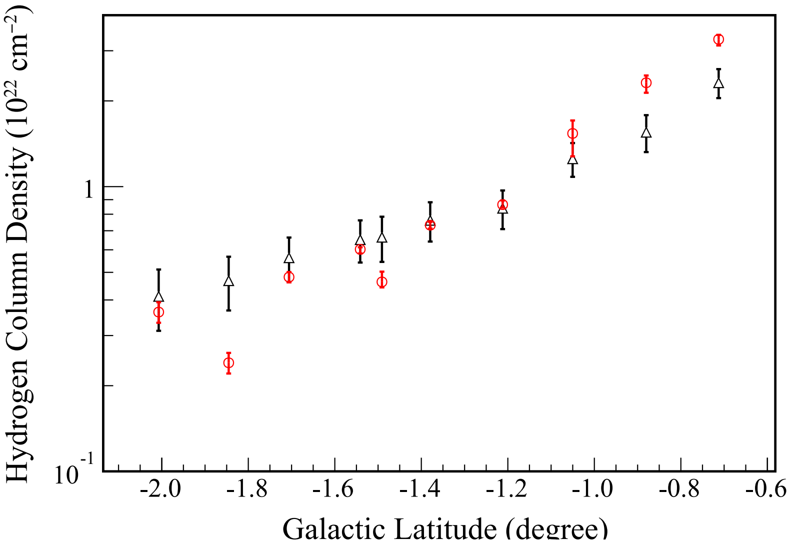

Figure 5.7. Absorption column densities along the Galactic latitude. The black and red data points show the $N_{\mathrm{H\,GC}}$ estimated from the near-infrared extinction and the best-fit N_{H} values obtained from the spatially resolved analysis, respectively.

5.4 Physical Properties of GC South

As shown in Figure 5.7, the absorption column densities for GC south (red) are consistent with those toward the GC region (black). Therefore, GC south is most likely to be located in the GC region (8 kpc distance). Then, the physical size of the plasma is $\sim$ 200 pc $\times$ 70 pc at this distance. Such a large diffuse plasma have not been discovered in the GC region except for the GCDX. Since the sound velocity of the plasma with $kT = 1.6$ keV is 510 km s^{-1}, the dynamical timescale, which takes for the plasma to travel the 200 pc length, is estimated to be $\sim 4 \times 10^5$ yr.

Assuming the depths of the emitting regions are 70 pc, we estimated the volume of each region (S-Src 1–10) as the apparent size $\times$ the depth (see Table 5.6). Then, we calculated the electron density (n_{e}), the pressure (p), the mass (M), and the thermal energy (E_{th}). We also estimated the recombination timescales from the best-fit $n_{\mathrm{e}}t$ and the derived n_{e}. These results are summarized in Table 5.6 and plotted in Figure 5.9. We discovered that n_{e} and p decreases with as higher the Galactic latitude. The recombination timescale is slightly larger as further from the GC and $\sim 3 \times 10^5$ yr, which is consistent with the dynamical timescale. The obtained M and E_{th} reach $\sim$ 3000 $M_{\odot}$ and $\sim 8 \times 10^{51}$ erg, respectively.

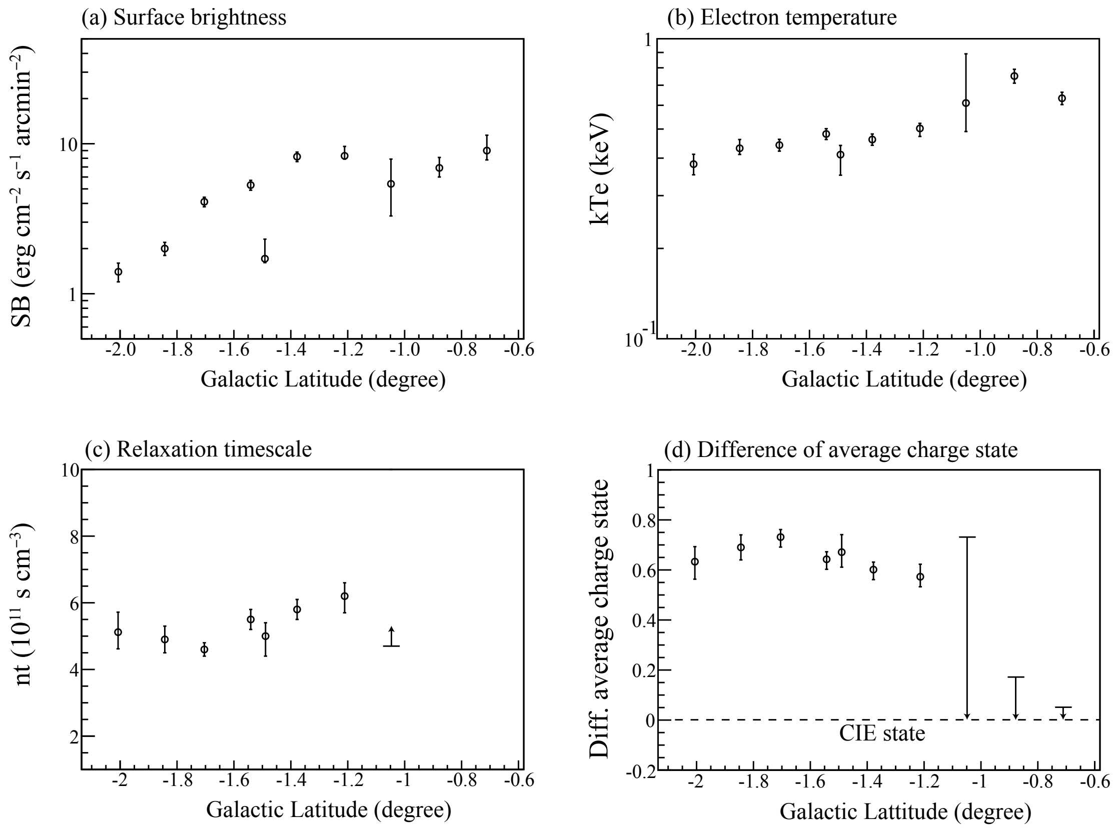

Figure 5.8. Best-fit parameters along the Galactic latitude. (a) surface brightness, (b) kT_e, (c) $n_\mathrm{e}t$, and (d) difference of the average charge state form the CIE model.

Table 5.6. Physical parameters of each region derived from the spatially resolved spectrum fitting.

Region	V^* (10^{60} cm^3)	n_e (10^{-2} cm^{-3})	P (10^{-10} erg cm^{-3})	M (10^2 solar)	E_th (10^{51} erg)	Recombination time (10^5 year)
S-Src 1	4.5	$10.9^{+1.4}_{-0.7}$	$1.6^{+0.2}_{-0.1}$	$5.7^{+0.8}_{-0.4}$	$1.7^{+0.2}_{-0.1}$	—
S-Src 2	2.7	$9.2^{+0.8}_{-0.6}$	$1.6^{+0.2}_{-0.1}$	$3.0^{+0.3}_{-0.3}$	$1.0^{+0.1}_{-0.1}$	—
S-Src 3	3.6	$8.8^{+2.0}_{-1.7}$	$1.3^{+0.7}_{-0.4}$	$3.7^{+0.9}_{-0.7}$	$1.1^{+0.6}_{-0.3}$	> 1.6
S-Src 4	1.4	$11.5^{+0.9}_{-0.3}$	1.4 ± 0.1	$1.9^{+0.2}_{-0.1}$	$0.46^{+0.04}_{-0.03}$	1.7 ± 0.1
S-Src 5	1.8	12.0 ± 0.5	1.3 ± 0.1	$2.5^{+0.1}_{-0.1}$	$0.55^{+0.03}_{-0.03}$	1.5 ± 0.1
S-Src 6	4.5	9.6 ± 0.4	1.1 ± 0.1	$5.0^{+0.2}_{-0.2}$	$1.1^{+0.1}_{-0.1}$	1.8 ± 0.1
S-Src 7	3.4	8.6 ± 0.3	0.91 ± 0.06	$3.4^{+0.1}_{-0.1}$	$0.71^{+0.04}_{-0.04}$	1.7 ± 0.1
S-Src 8	3.3	$5.8^{+0.9}_{-0.2}$	$0.57^{+0.10}_{-0.09}$	$2.2^{+0.4}_{-0.1}$	$0.43^{+0.08}_{-0.07}$	$2.7^{+0.5}_{-0.3}$
S-Src 9	3.0	6.3 ± 0.3	$0.65^{+0.05}_{-0.04}$	$2.2^{+0.1}_{-0.1}$	$0.46^{+0.04}_{-0.03}1$	$2.5^{+0.2}_{-0.2}$
S-Src 10	1.2	5.6 ± 0.4	0.51 ± 0.05	$0.8^{+0.1}_{-0.1}$	$0.15^{+0.02}_{-0.02}$	$2.9^{+0.4}_{-0.3}$

Notes:

Quoted errors include only statistical errors in the spectrum fitting.

* Assumed the line of sight length of 70 pc.

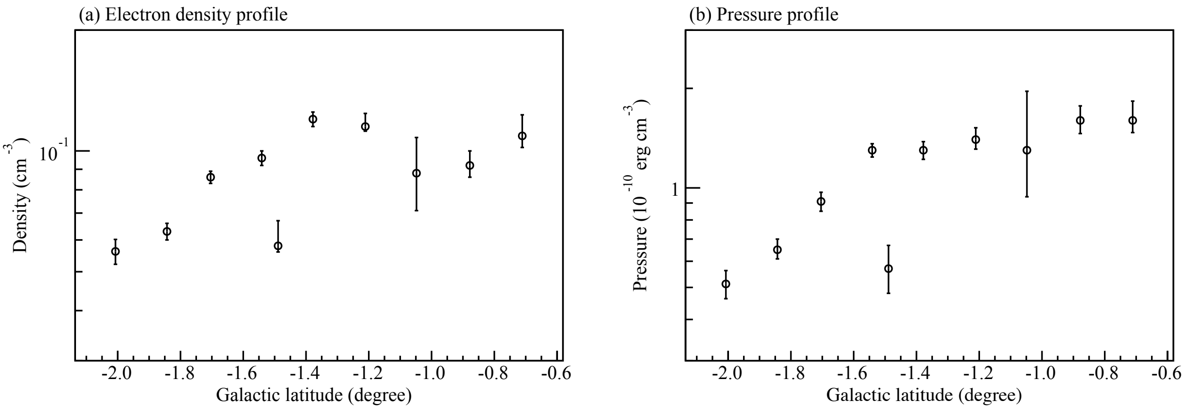

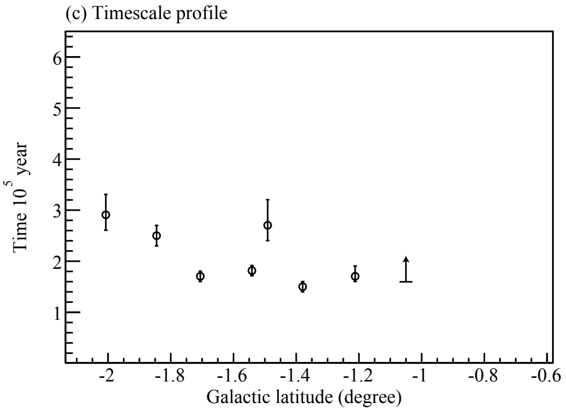

Figure 5.9. Spatial profiles of (a) n_e, (b) P, and (c) recombination timescale of the plasma.

Chapter 6

Analysis on GC North

In this chapter, we present the analysis results of GC North, a possible counterpart to GC South.

Contents

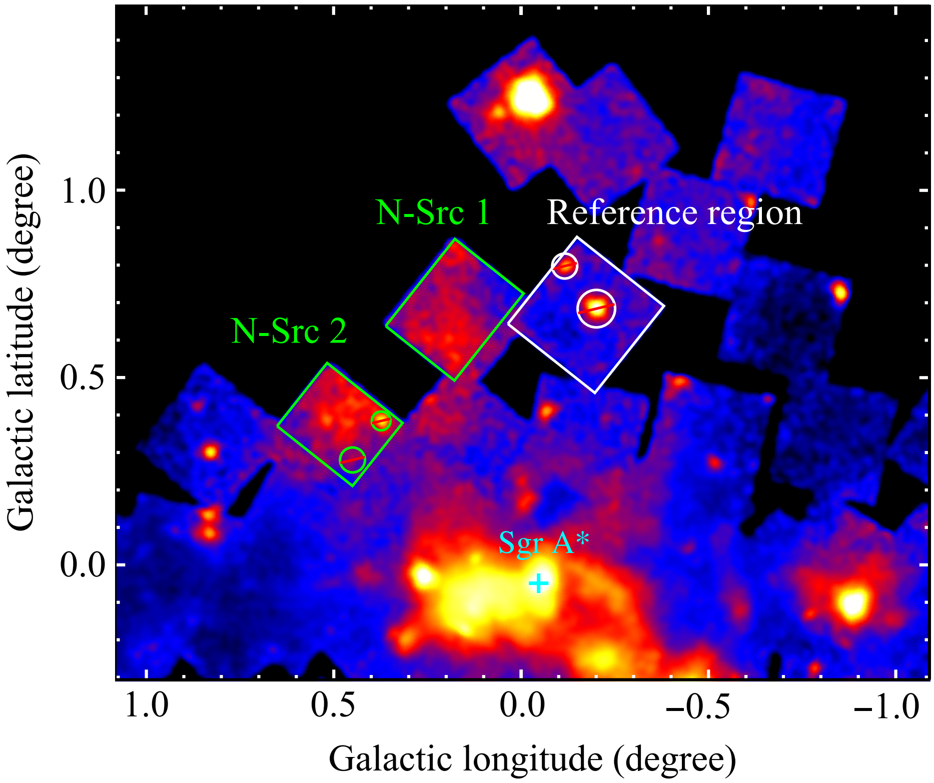

Figure 6.1. Close-up view of the GC North region in the 1.0–3.0 keV band take by *Suzaku*. The green and white squares indicate the source and reference regions, respectively. The cross shows the location of Sgr A*.

6.1 Analysis Method

We found GC North extending ∼1° north of Sgr A* from the *ASCA* image (Figure 4.3). However, photon statistics and energy resolution of the GIS data are not sufficient for spectral investigation. Therefore, we used the *Suzaku* data, although the entire GC North is not covered. Figure 6.1 shows the close-up view of the GC North region in the middle band taken by *Suzaku*. GC North is not seen in the soft and the hard band (see Figure 4.1). We chose the source and reference regions as shown in the green and white rectangles in Figure 6.1, respectively. Observations used in this analysis are listed in Table 6.1. The criteria of the data calibration and screening is the same as described in Section 4.1.1. The RMFs and ARFs were also compiled in the same manner.

Table 6.1. Observation logs of the GC North region.

Sequence #	Aim Point				Obs. Date	Exposure	Obs. Name
	$\alpha_{2000.0}$	$\delta_{2000.0}$	l	b	(yyyy-mm-dd)	(ks)	
				Source regions			
502007010	$265\overset{\circ}{.}86$	$-28\overset{\circ}{.}45$	$0\overset{\circ}{.}16$	$0\overset{\circ}{.}66$	2007-10-11	22	GC19
502010010	$266\overset{\circ}{.}38$	$-28\overset{\circ}{.}34$	$0\overset{\circ}{.}50$	$0\overset{\circ}{.}33$	2007-10-13	22	GC22
				Reference regions			
502008010	$265\overset{\circ}{.}66$	$-28\overset{\circ}{.}73$	$359\overset{\circ}{.}83$	$0\overset{\circ}{.}66$	2007-10-12	24	GC20

6.2 Background Estimation

As same as the case of GC South, precise Galactic BG estimation is crucial for the analysis of GC North. Therefore, we investigated a spectrum in the reference region (white rectangle in Figure 6.1). The obtained spectrum is shown in Figure 6.2. Its spectrum shape is similar to that in the Ref 2 region used in the GC South analysis (see Figure 5.2)

We applied the BG model constructed in Section 5.2. At first, all the parameters were fixed to the values shown in Table 5.2 except for $N_{\mathrm{H\,GC}}$ and $factor$, because the interstellar column density and the intensity of the GRXE are different from position to position. The parameter of $factor$ was treated as a free parameter while the absorption column density was fixed to a value estimated from near-infrared extinction (Gonzalez et al. 2012). The extinction in the reference region ($l \sim 0\overset{\circ}{.}17$, $b \sim 0\overset{\circ}{.}66$) is $A_{K_s} = 1.21$, so that $N_{\mathrm{H\,GC}}$ was estimated to be 2.2×10^{22} H cm^{-2} using the conversion factor of $N_{\mathrm{H}}/A_{K_s} = 1.8 \times 10^{22}$ cm^{-2} mag^{-1} (see Section 5.2). The fitting result is plotted on Figure 6.2(a). This model roughly represents the spectrum, but large residuals remain with χ^2/d.o.f = 541/237.

We then allowed to vary kT_{HP}, kT_{LP}, and EM_{FE} for the fine-tuning of the model. As a result, the fit is considerably improved with χ^2/d.o.f = 344/234, but small residuals still remain at the energy of S XIII Kα line (2.4 keV) and the S XXV Kα line (6.7 keV). We finally varied the abundances of Si and Fe, and obtained the best-fit model shown in Figure 6.2(b) with χ^2/d.o.f = 289/232. The best-fit parameters are listed in Table 6.2.

The obtained kT_{HP}, kT_{LP}, and EM_{FE} are consistent with the original BG model. On the other hand, the abundances of Si and Fe are larger than 70% and 30% from the original BG model, respectively. We confirmed that the flux in the 5–8 keV band is consistent with that of the model composed by Uchiyama et al. (2013). Therefore this model is plausible.

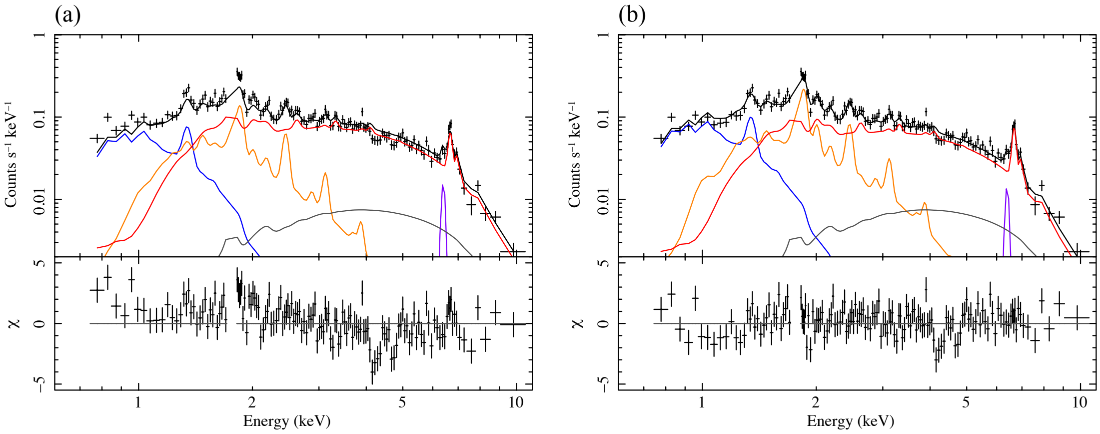

Figure 6.2. Spectra of the reference region. (a) the model which is the same as GC South BG. (b) the model fine-tuned.

Table 6.2. Fitting results of the spectra in the reference regions for GC North.

— HP + LP + Gaussian —		— FE —	
Free parameters			
factor	1.38 ± 0.07	$EM^{*}_{\rm FE}$ (10^{58} cm^{-3})	1.26 ± 0.06
$kT_{\rm HP}$ (keV)	6.7 ± 0.6		
$kT_{\rm LP}$ (keV)	0.81 ± 0.06		
Si (solar)	1.6 ± 0.2		
Fe = Ni (solar)	0.69 ± 0.09		
Fixed parameters			
$N_{\rm H\,GC}$ (10^{22} cm^{-2})	2.2	$N_{\rm H\,FE}$ (10^{22} cm^{-2})	0.42
$EM^{*}_{\rm HP}$ (10^{58} cm^{-3})	0.38	$kT_{\rm FE}$ (keV)	0.33
$EM^{*}_{\rm LP}$ (10^{58} cm^{-3})	0.45	Ne (solar)	0.06
Mg = Ne (solar)	0.43	Mg (solar)	0.19
S (solar)	1.6	Other Elements (solar)	0.022
Ar (solar)	3.5		
Ca (solar)	2.8		
Other Elements (solar)	1		
Fe I Kα flux (10^{-6} ph cm^{-2} s^{-1})	6.4		

Notes:

[*] Emission measure assuming the distance of 8 kpc. $EM = \int n_{\rm e} n_{\rm p} dV$, where $n_{\rm e}$, $n_{\rm p}$, and V , are the electron density, the proton density, and the emitting volume, respectively.

6.3 Spectrum Analysis

6.3.1 Merged spectrum

We extracted the spectra of GC North from the two rectangle regions shown in Figure 6.2 (N-Src 1 and N-Src 2). Firstly, these spectra were co-added to increase the photon statistics (hereafter the merged spectrum). Figure 6.3 shows the merged spectrum. Based on the image analysis in Section 6.1, the emissions below 1 keV and above 5 keV are likely to be the FE and the GRXE, respectively. In order to subtract these component, we used the BG model constructed in the previous section. The absorption column density of the GRXE is evaluated from the infrared extinction in this region, and found to be 2.5× 10^{22} H cm^{-2}. The normalization factor is allowed to vary. Applying this BG model, we found the excess of the data with emission lines of Mg, Si, and S as shown in Figure 6.3.

These emission lines suggest an optically-thin thermal plasma origin, and thus we added a CIE plasma model. Free parameters were N_{H}, kT_{e}, EM, and the abundances of Mg, Si and S. The abundances of the other elements were fixed to the values in GC South (see Table 5.3), because they are not determined due to poor photon statistics and/or strong absorption of GC North. After fitting with this model, we found a Gaussian like residual at 1.2 keV, which is likely the missing Fe-L shell lines (see Section 5.3.1). Therefore, we also added a Gaussian at 1.2 keV in the same manner as done in the GC South. The spectrum is represented by this model with χ^2/d.o.f = 236/185. The best-fit parameters are tabulated in Table 6.3. We also attempted RP and IP models, but no significant improvement was obtained.

6.3.2 Spatially resolved spectra

From the analysis of the merged spectrum, we found that the CIE model is favor in GC North. In order to investigate the spatial variation of the plasma parameters, we then analyzed the spectra of N-Src 1 and N-Src 2 separately. For the BG model, the absorption column density of $N_{\mathrm{H\,GC}}$ in each region is re-estimated from the near-infrared extinction, and listed in Table 6.3.

Their spectra were fitted with the CIE models as same as the merged-spectrum fitting but elemental abundances were fixed to the best-fit value of the merged spectrum. Figure 6.4 and Table 6.3 shows the fitting results and obtained plasma parameters, respectively. We obtained the different electron temperature for each region

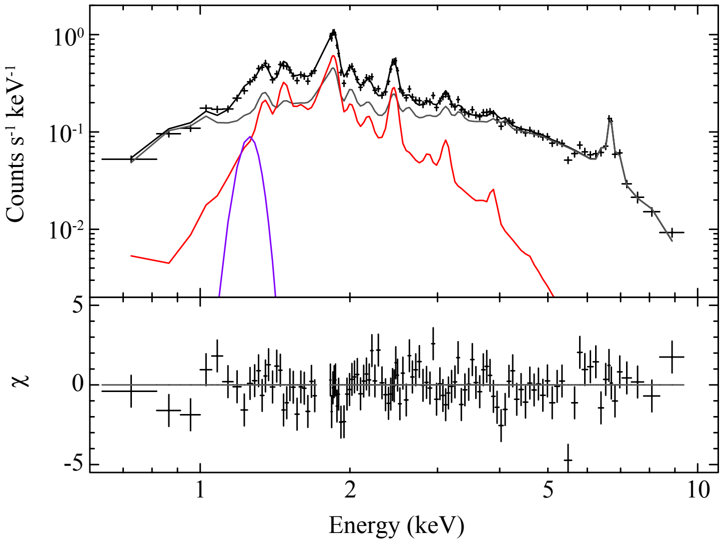

Figure 6.3. Merged Spectra of GC North fitted with the CIE model. The gray, red, and purple lines indicate the BG model, the best-fit CIE model, and the missing Fe L-shell line respectively. Only the co-added FI spectrum and model are displayed for visibility, although the FI and BI spectra were simultaneously fitted.

Table 6.3. Fitting results of the merged spectrum.

Parameter (Unit)	Merged spectrum	N-Src 1	N-Src 2
$N_{\mathrm{H\,GC}}^{*}$ (10^{22} cm^{-2})	2.5 (fix)	2.0 (fix)	2.8 (fix)
N_{H} (10^{22} cm^{-2})	$2.6^{+0.3}_{-0.2}$	2.5 ± 0.2	3.3 ± 0.3
$EM^{\dagger}$ (10^{58} cm^{-3})	$3.4^{+0.8}_{-0.6}$	$2.5^{+0.6}_{-0.5}$	$2.2^{+0.8}_{-0.5}$
kT_{e} (keV)	0.73 ± 0.04	0.61 ± 0.04	0.76 ± 0.06
Mg (solar)	$0.9^{+0.3}_{-0.2}$	0.9 (fixed)	0.9 (fixed)
Si (solar)	0.9 ± 0.1	0.9 (fixed)	0.9 (fixed)
S (solar)	1.2 ± 0.2	1.2 (fixed)	1.2 (fixed)
SB‡	$2.2^{+0.5}_{-0.4}$	$2.3^{+0.6}_{-0.5}$	$2.7^{+1.0}_{-0.6}$
χ^2/dof	236/185	216/185	315/220

Notes:

[*] Absorption column density for the BG emissions that were estimated from the near-infrared extinction investigated by Gonzalez et al. (2012).

[†] Emission measure assuming the distance of 8 kpc.

[‡] Absorption-corrected surface brightness in the 1.5–3.0 keV band with a unit of 10^{-14} erg s^{-1} cm^{-2} arcmin^{-2}

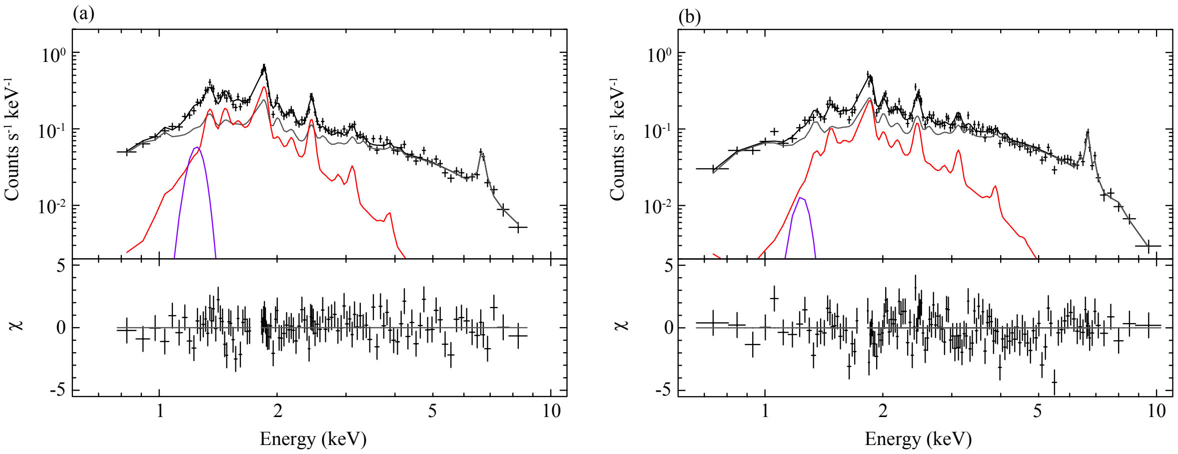

Figure 6.4. Spectra extracted from (a) N-Src 1 and (b) N-Src 2. The gray, red, and purple lines indicate the BG models, the best-fit CIE models, and the missing Fe L-shell lines respectively. Only the co-added FI spectra and models are displayed for visibility, although the FI and BI spectra were simultaneously fitted.

6.4 Physical Properties of GC North

As shown in Table 6.3, the obtained absorption column densities for the N-Src 1 and N-Src 2 regions are consistent with estimated $N_{\rm H\,GC}$, whose typical errors are $\sim$ 15%. We therefore concluded that GC North is truly located at the GC distance (8 kpc). At this distance, apparent size of the N-Src 1 and N-Src 2 regions are 900 pc^2 and 860 pc^2, respectively.

Assuming the length along the line of sight to be 70 pc, we estimated the volume of the plasma, and calculated physical parameters. The results are summarized in Table 6.4. The density and pressure in N-Src 1 is slightly smaller than that in N-Src 2. The total mass and thermal energy are $\sim$460 $M_\odot$ and $\sim$1.5 $\times$ 10^{51} erg, respectively. Since the entire size of GC North seen in the *ASCA* image is about 2 times larger than that of analysis region, total mass and thermal energy probably reach $\sim$900 $M_\odot$ and $\sim$3 $\times$ 10^{51} erg, respectively. The sound velocity of the plasma (kT $\sim$ 0.7 keV) is 400 km s^{-1}. Therefore we have the dynamical timescale of $\sim$4 $\times$ 10^5 yr for crossing the plasma size of $\sim$ 150 pc.

Table 6.4. Physical parameters of the N-Src 1 and N-Src 2.

Region	V^* (10^{60} cm^3)	$n_{\rm e}$ (10^{-1} cm^{-3})	p (10^{-10} erg cm^{-3})	M (10^2 solar)	$E_{\rm th}$ (10^{50} erg)
N-Src 1	1.7	1.2 ± 0.2	1.8 ± 0.2	2.4 ± 0.3	7.0 ± 1.0
N-Src 2	1.6	1.2 ± 0.2	2.1 ± 0.4	2.2 ± 0.4	7.8 ± 1.6

Notes: Quoted errors include only statistical errors in the spectrum fitting.

* Assumed the line of sight length of 70 pc.

Chapter 7

Discussion

In this chapter, we summarize the analysis results in the preceding chapters, and discuss possible origins of GC South and GC North.

Contents

Table 7.1. Typical physical parameters of GC South and GC North

Region	kT_{e} (keV)	n_{e} (cm^{-3})	Ionization state	Abundance* (solar)	E_{th} (erg)	M ($M_\odot$)	$t^\dagger_{\mathrm{rec}}$ (year)	$t^\ddagger_{\mathrm{dyn}}$ (year)
GC South	0.4–0.8	0.06–0.12	RP or CIE	0.7–0.8	8×10^{51}	3000	3×10^5	4×10^5
GC Nouth	0.7	0.12	CIE	0.9–1.2	3×10^{51}	900	—	4×10^5

Notes:
* Abundances of Mg, Si, and S.
† Recombination timescale of the plasma
‡ Dynamical timescale (size/sound velocity) of the plasma.

7.1 Summary of the Obtained Parameters

In the preceding chapters, we derived the physical parameters of GC South and GC North. Typical parameters are tabulated in Table 7.1. We also summarized the spatial variation of the plasma parameters along the Galactic latitude in Figure 7.1 and Figure 7.2.

Figure 7.1 shows the profile of the absorption column density for the GC South/North compared with the near-infrared extinction (Gonzalez et al. 2012). We adopted the conversion factor of $N_{\mathrm{H}}/A_{K_s} = 1.8 \times 10^{22}$ H cm^{-2} mag^{-1} derived in Section 5.2. The absorption column density for the GCDX reported by Uchiyama et al. (2013) is also potted as a reference. There is a ~40% discrepancy between the X-ray absorption and the near-infrared extinction at $b = 0°$. Gonzalez et al. (2012) noted that extinction in the GC region ($A_{K_s} > 2$ or $N_{\mathrm{H}} > 3.6 \times\ 10^{22}$ H cm^{-2}) is underestimated by a few tens of percent because of incompleteness of the sample. Thus, this discrepancy is mainly due to the observational bias. The gradient of the X-ray absorption well agrees with that of the near-infrared extinction, which indicates that GC South and GC North are located at the GC distance.

Figure 7.2 shows the spatial profiles of the surface brightness, temperature, density and pressure. We also plotted those of LP and HP in the GCDX as a reference. We referred to the result reported by Uchiyama et al. (2013) for the surface brightness. Other parameters of the GCDX are derived from Muno et al. (2004), in which the central $17' \times 17'$ filed was investigated. Since the parameters of GC North are determined predominantly in the 1.5–3.0 keV band, absorption-corrected surface brightnesses of all the regions, including GC South and the GCDX, were calculated in this band. We see that all of the parameters decline smoothly from the GC to the high Galactic latitude and are nearly symmetrical about the GC, although the data in the positive latitude is insufficient.

At first, we consider a possible origin of GC South using these information. Then, we discuss the origin of GC North and revealed the connection between GC South and GC North.

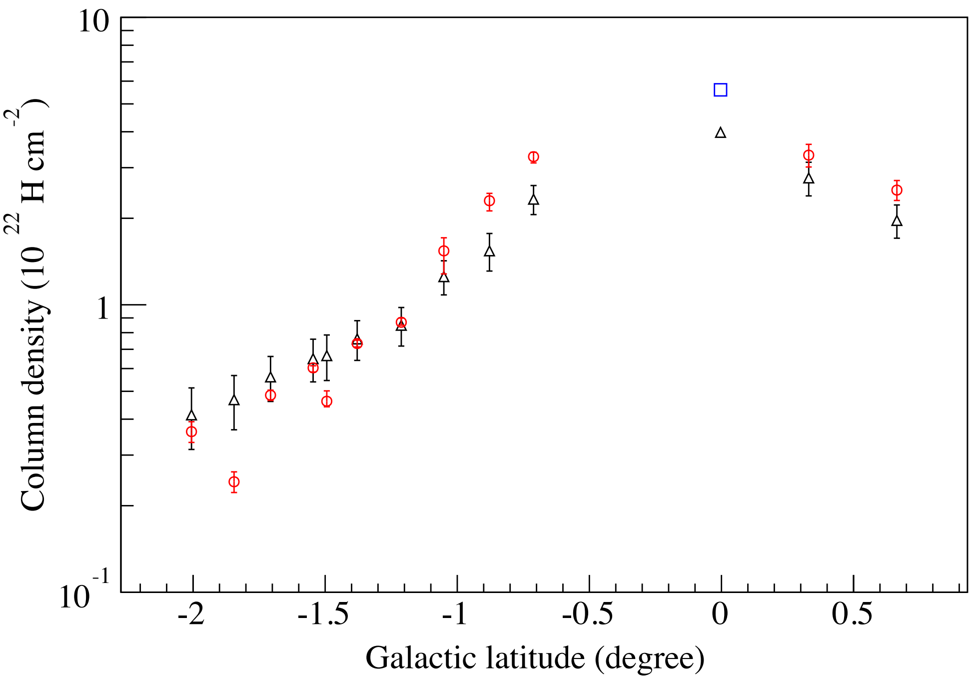

Figure 7.1. Absorption column densities along the Galactic latitude obtained from the GC South and GC North (the red circles), the GCDX (the bule squares; Uchiyama et al. 2013), and the infrared extinction (the black triangles; Gonzalez et al. 2012) converted by the factor of 1.8×10^{22} H cm^{-2} mag^{-1}.

7.2 Origin of GC South

7.2.1 Energy source

Typical thermal energies observed in Galactic X-ray SNRs are $\sim 10^{49-50}$ erg, which is 1–10% of the total energy released by a single SN (10^{51} erg). We found the thermal energy of GC South to be 8×10^{51} erg. Therefore, GC South is about two orders of magnitude more energetic than a single SNR, and hence a single SN origin is rejected. In fact, non-thermal radio shell, which is evidence for an SNR, is not found near GC south (e.g., LaRosa et al. 2000).

As seen in Galactic superbubbles, multiple SNe and stellar winds in an active star-forming region can provide sufficient energy for the formation of GC South. However, there is no active star-forming region at the location of GC South except for the S-Src 1–3 filed (see Section 5.3.2). Since some of the H II regions found in the S-Src 1–3 field are located at the foreground of the GC, they are not associated with the GC South. Moreover, the

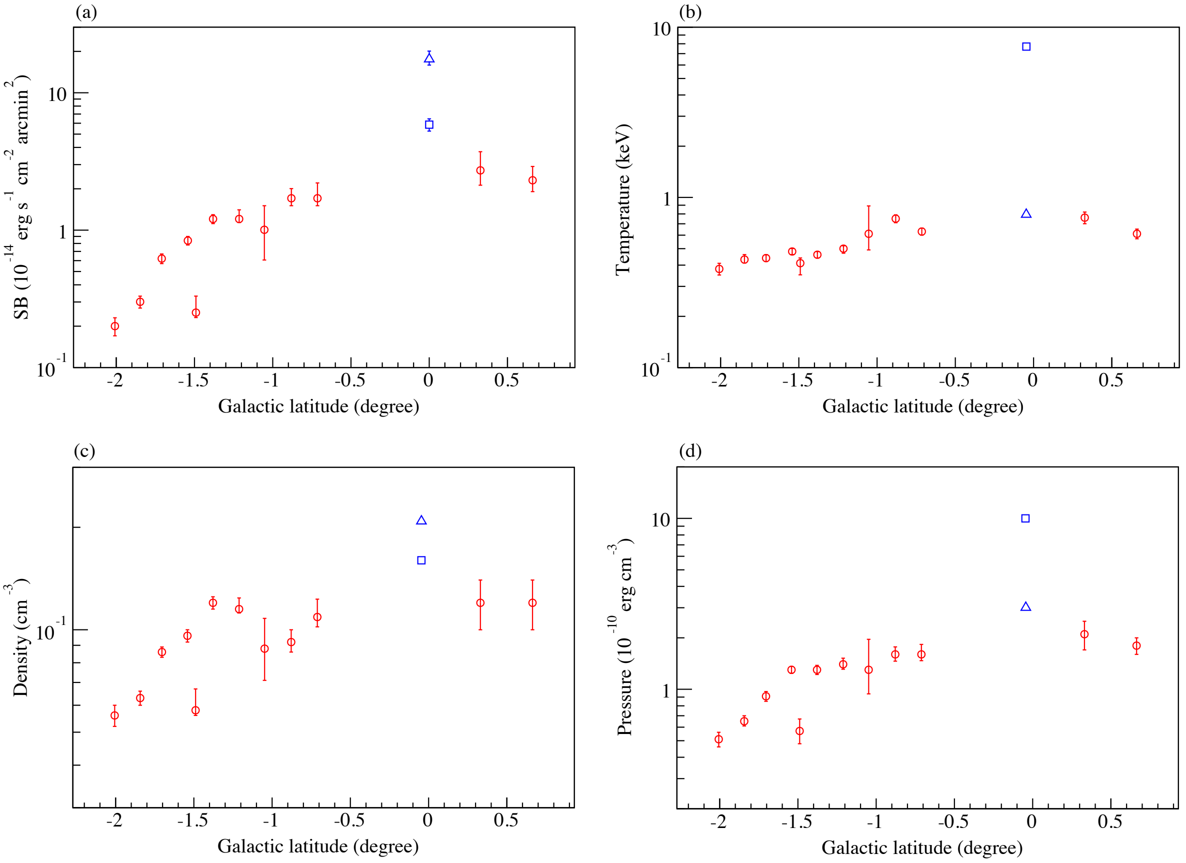

Figure 7.2. Spatial profiles of (a) surface brightness, (b) electron temperature, (c) electron density, and (d) thermal pressure along the Galactic latitude. The red circles indicates the parameters of GC South and GC North. The blue triangles and squares are the parameters of LP and HP in the GCDX, respectively (Uchiyama et al. 2013; Muno et al. 2004).

temperature and density of GC South are higher than those of typical Galactic superbubbles ($kT < 0.3$ keV and $n \sim 0.01$ cm^{-3}). Therefore, the superbubble origin is not favored for GC South.

Remaining energy sources are GC activities. We found that the recombining timescale of GC South is ~3×10^5 yr, and is consistent with the dynamical timescale (see Table 7.1). Therefore, required energy-injection rate is estimated as 8×10^{51} ergs/3×10^5 yr $= 9 \times 10^{38}$ erg s^{-1}. We examine whether GC activities can provide this energy in the following section.

GC activities at present

The current SN rate in the nuclear region ($r < 50$ pc) is estimated to be only one per 10^4 yr, corresponding to 10^{38} erg s^{-1} (assumed 10% efficiency). It is not sufficient to form GC South. Moreover, the current Sgr A* luminosity of 10^{33}–10^{35} erg s^{-1} in the X-ray band is also 4–6 orders of magnitude lower than the required energy. Therefore, the GC activities at present are not able to form GC South.

Past starburst

One possible energy source is a past nuclear starburst activity. In starburst galaxies, we usually see outflows of plasmas with temperature of 0.3–2.0 keV, the so-called superwinds. The superwind in NGC 253 has the size and the energy of $\sim$1 kpc and $\sim 10^{53}$ erg, respectively (Strickland et al. 2000). Although they are about one orders of magnitude higher than those of GC South, other physical features (temperature, density, and morphology) are similar.

Yusef-Zadeh et al. (2009) claimed that the GC SFR 10^5–10^7 yr ago is one order of magnitude higher than that at present. The past starburst scenario is also proposed as the origin of the *Fermi* bubbles, although their timesscale of 10^7 yr is different from that of GC South (10^5 yr). If the nuclear SN rate was one order of magnitude higher than the current rate 10^5 yr ago, the energy of $\sim 10^{39}$ erg s^{-1} was provided and GC South was formed like a superwind.

We then check the consistency between the superwind origin and the obtained plasma parameters. In order to blow out the plasma from the GC, the pressure of the ISM in the Galactic bulge should be lower than that of the plasma. According to an model of the ISM distribution (Ferrière et al. 2007), we found that the density of H I and H^+ in the GC South region are < 5 cm^{-3} and ~ 0.15 cm^{-3}, respectively. The contribution of H_2 clouds is negligible in this region (see Figure 2.3). Then, the thermal pressure of H I ($\sim 10^3$ K) and H^+ ($\sim 10^4$ K) is $< 10^{-12}$ erg s^{-1} and $\sim 10^{-13}$ erg s^{-1}, respectively. They are two orders of magnitude lower than the thermal pressure of GC South, and hence plasma can be blown out from the GC. In Figure 7.2(d), we can also see that the thermal pressure decreases from the GC to the southern edge of GC South. These facts support the superwind origin.

Past Sgr A* jet

Another possible energy source is a jet from the central SMBH. Some AGNs exhibit thermal plasma emissions, which are produced by jet-cloud interactions (e.g., NGC 4258 and NGC 4151). These plasmas have the size of a few kpc and the temperature of $\sim$0.5 keV, and resemble GC South.

As reviewed in the Section 2.3.3, Sgr A* was active 10^2–10^3 yr ago with the luminosity of 10^{39} erg s^{-1} (Ryu et al. 2013). If Sgr A* was more active 10^5 yr ago, it probably emitted a jet whose energy is comparable to the luminosity of the central engine. Then, the jet possibly generated a shock-heated hot plasma in the GC South region. Such a jet-like activity 10^6 yr ago is also proposed as the origin of the *Fermi* bubbles although it is still controversial. Thus, the past Sgr A* jet origin is not ruled out.

7.2.2 Mechanism to form the recombining plasma

We discovered the RP in GC South (S-Src 4–10), which is not explained in the standard evolution of a shock-heated plasma; a shock-heated low-density ($\sim$1 cm^{-3}) plasma is in an ionizing phase for a long period because the time scale of electron heating ($\sim$100 yr) is much shorter than that of collisional ionization ($\sim 10^4$ yr). Therefore, to realize an RP, some specific events should occur: either a rapid decrease in electron temperature or an enhancement of only the ionization. We discuss possible scenarios in the following.

Adiabatic expansion scenario

In Galactic RP SNRs , two mechanisms for a decrease in electron temperature have been proposed (e.g., Sawada & Koyama 2012; Uchida et al. 2012), and supported by numerical simulations (e.g., Zhou et al. 2011; Shimizu et al. 2012). We attempt to apply these scenarios to GC south. One is thermal conduction via interactions with ambient cold molecular clouds. However, no such molecular clouds have been found in this region. Moreover, electron temperature is lower in the higher Galactic latitude, where cold gas density become lower (Ferrière et al. 2007). Therefore this scenario is unlikely.

The other scenario is adiabatic expansion of the plasma. In this scenario, the CIE plasma was formed in a dense circumstellar medium at the starburst site. Then, the plasma were blown out rapidly to a thin circumstellar space, and the electron temperature rapidly decrased as a result of adiabatic expansion. The electron temperature is expected to decrease with distance away from the GC, and the ionization state should be CIE near the GC while it becomes an over-ionized state at the far side of the GC. The observational results are consistent with this pictures (see Figure 5.8). In adiabatic condition, $T \propto n^{\gamma-1}$ is also expected. For ideal monatomic gas ($\gamma = 5/3$), the index of the above equation is 2/3. Figure 7.3(a) shows the correlation between the observed kT_e and n_e. We can see a positive correlation between them, and fitting with a power-law function gave us the best-fit index of 0.4 ± 0.3. It is consistent with the adiabatic equation within the 90% confidence interval as shown in the red bow tie in Figure 7.3(a). Although kT_e and n_e (or emission measure) are coupled with each other in the spectral fitting, their correlation is negative as shown in

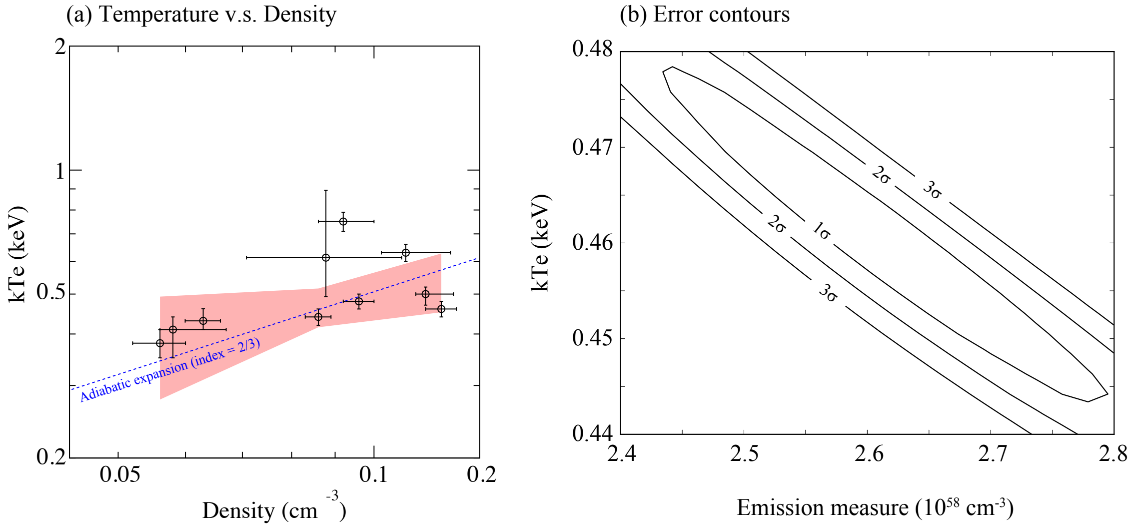

Figure 7.3. (a) Correlation between the temperature and density of GC South derived from the spatially resolved fitting. A red bot tie shows the best-fit power-law function. A dotted blue line indicates the adiabatic process of $T \propto n^{2/3}$ (see text). (b) Typical error contours between the temperature and the emission measure in the spectral fitting. The contours show 1σ, 2σ, and 3σ levels.

Figure 7.3(b). Therefore, the positive correlation between $kT_{\rm e}$ and $n_{\rm e}$ is reliable. Then, the adiabatic expansion scenario is favored for GC South.

We further examine whether plasmas located in the current GC region satisfy the initial condition of GC South. The initial plasma should have the temperature of 1.6 keV (see Section 4.3.1). From a simple extrapolation of the adiabatic equation obtained from the $kT_{\rm e}$–$n_{\rm e}$ relation (Figure 6.3), we obtained the initial plasma density of 0.6 cm^{-3}. The density of the GCDX, both the LP and the HP, is smaller than the expected value by a factor of 3–4. Mori et al. (2009) discovered the GC superbubble, which has $kT_{\rm e} = 0.91$ keV and $n_{\rm e} = 0.26$ cm^{-3}, but they does not agree with the initial plasma parameters of GC South. The Sgr A East SNR is only a possible candidate. It consists of the low temperature ($kT_{\rm e} = 1.2$ keV, $n_{\rm e} = 4.6$ cm^{-3}) and high temperature ($kT_{\rm e} = 6$ keV, $n_{\rm e} = 0.6$ cm^{-3}) plasma (Koyama et al. 2007a). These parameters are close to or larger than the required parameters. The past starburst activity might form a large amount of plasmas like the Sgr A East SNR.

Sgr A* photoionization scenario

Not rapid electron cooling but selective ionization also forms an RP. One possibility is photoionization; a plasma is illuminated by a strong X-ray source and is initially over-ionized. After the termination of photoionization, the plasma enters a recombining phase. The balance between photoionization and recombination is described by a single parameter, $\xi = L/(nR^2)$, where L, n, and R are the luminosity of the source, the gas density, and the distance between the irradiating source and the plasma, respectively. To achieve nearly the same ionization state as the 1.6 keV CIE plasma, ξ should be $\sim$1000 (Kallman & Bautista 2001). Then, the required luminosity is estimated as

$$L = 3.6 \times 10^{43} \left(\frac{R}{200\ \mathrm{pc}}\right)^2 \left(\frac{n}{0.1\ \mathrm{cm}^{-3}}\right)\ \mathrm{erg\ s^{-1}}, \tag{7.1}$$

where R is assumed to be the size of GC South. Only a past Sgr A* flare with the nearly Eddington luminosity ($\sim 10^{44}$ erg s^{-1}) can achieve such a extremely high luminosity. The flare should not be isotropic radiation, because the GCDX, which is in the vicinity of Sgr A*, is not an RP but a CIE plasma (Koyama et al. 2007b). Therefore, GC south must be illuminated by collimated radiation like a jet, if the photoionization scenario is the case.

We discussed a Sgr A* jet as the possible energy source of GC South in the previous section. Assuming this jet also emitted collimated X-rays such as a blazar activity, the plasma was formed and photoionized simultaneously. In this scenario, entire GC South region should became an RP. Moreover, a higher ionization state is expected as the plasma is closer to Sgr A*, because the radiation field is stronger near Sgr A*. However, the observed spatial variation of the ionization states is opposite to this prediction. As shown in Figure 5.8(d), the plasmas in S-Src 1–3 are not RPs but CIE plasmas, and there is no significant variation of the ionization states in the S-Src 4–10 region. Therefore this scenario is not favored.

Alternatively, we consider another scenario, where a plasma was generated by a nuclear starburst activity and was then photoionized by a Sgr A* jet in the course of an outflow. Rapid electron cooling due to adiabatic expansion is not necessary in this scenario. Assuming the starburst-region size of 50 pc, required luminosity is estimated to be $\sim 10^{42}$ erg s^{-1} from Eq.7.1. If Sgr A* became quiescent in the middle of the starburst period, no more RP was formed. Thus, this scenario is able to explain the composite ionization state of GC South; plasmas generated in early phase (S-Src 4-10) were photoionized by a Sgr A* jet, but Sgr A* became quiescent after photoionizing the S-Src 4 plasma. Then, the plasma formed later (S-Src 1-3) were no more photionized and kept the CIE states. Since the boundary between S-Src 3 and S-Src 4 is 150 pc south of Sgr A*, phase transition of Sgr A* should be occur 3×10^5 year ago when the outflow speed is 510 km s^{-1}. It is consistent with the recombining timescale of S-Src 4 within a factor of 2. Therefore, this scenario is cannot be excluded.

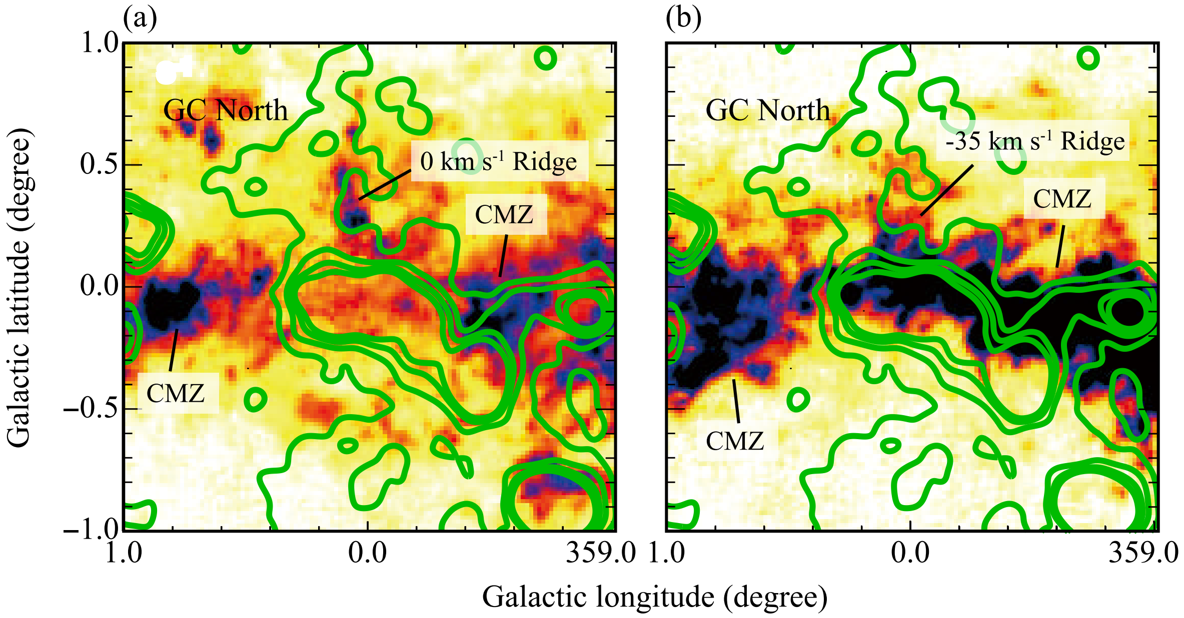

Figure 7.4. Images of CO (J=2–1) emission in the velocity range of (a) −3–0 km s^{-1} and (b) −39–−31 km s^{-1} (Enokiya et al. 2013). The overlaid green contours are the X-ray emission derived from the *ASCA* image in the 1.5–3.0 keV band (Figure 4.3).

7.3 Origin of GC North

The thermal energy of GC North is about one order of magnitude higher than that of typical SNRs. In addition, star forming region is not found near GC North. Therefore, a single or a multiple SN origin is unlikely.

The most plausible energy source is a GC activity as proposed for GC South. Since the required energy-injection rate estimated from the dynamical timescale is 3×10^{38} erg s^{-1}, which is comparable to that of GC South, the current GC activities cannot provide sufficient energy as discussed in Section 7.2.1. Therefore, a past starburst or a jet from Sgr A* are possible origins for GC North.

7.4 Connection between GC South and GC North

We show that both GC South and GC North were formed by past GC activities $\sim 10^5$ yr ago. Since they have nearly the same timescales, we suspect that the identical past activity formed both GC South and North. Indeed, parameters of kT_{e}, n_{e}, abundance, E_{th}, and M are similar between GC South and GC North as shown in Table 7.1, and the identical origin is supported. If this is the case, a past nuclear starburst is the energy source of GC Sout/North from the discussion of Section 7.2.1. However, morphology and ionization states are different from each other. We consider the cause of these differences, although spatial variation of plasma parameters for GC North is poorly constrained,

The emission of GC South extends to $b = -2\overset{\circ}{.}0$ along $l = 0\overset{\circ}{.}0$, while that of GC North extends to only $b = 1\overset{\circ}{.}2$ and shifted to the east ($l \sim 0\overset{\circ}{.}25$). One possible cause of the morphological difference is asymmetrical distribution of the ISM. Enokiya et al. (2013) discovered the molecular ridges (the 0 km s^{-1} ridge and the -35 km s^{-1} ridge) to the north of the GC, which have the mass of $\sim 10^5\ M_\odot$. Figure 7.4 shows the images of CO (J=2–1) overlaid with *ASCA* X-ray contours. We found that the X-ray emission of GC North shows anticorrelation with the molecular ridges. Assuming the its density of $\sim 10^3$ cm^{-3} (critical density of CO J=2–1) and the temperature of $\sim$70 K (typical value of the CMZ), the thermal pressure of the molecular ridge is $\sim 10^{10}$ erg cm^{-3} and comparable to that of GC North. Therefore, we consider that both or either molecular ridge has prevented the plasma from outflowing and distorted the plasma shape.

We found no RP in GC North contrary to in GC South. One simple explanation is that the *Suzaku* observations have not covered the RP region in GC North. Since we discovered the RP in $b < -1\overset{\circ}{.}0$, the plasma in $b > 1\overset{\circ}{.}0$ could be an RP. Another explanation is that an RP was not formed in GC North. As shown in Figure 7.4, the GC North plasma may be prevented from expanding by the molecular ridges. If adiabatic expansion scenario is the case for GC South (see Section 7.2.2), the GC North plasma was not able to expand adiabatically and therefore did not become an RP. In any case, feature *Suzaku* observations of the GC North region will reveal the true. We finally summarized the activity history on Figure 7.5.

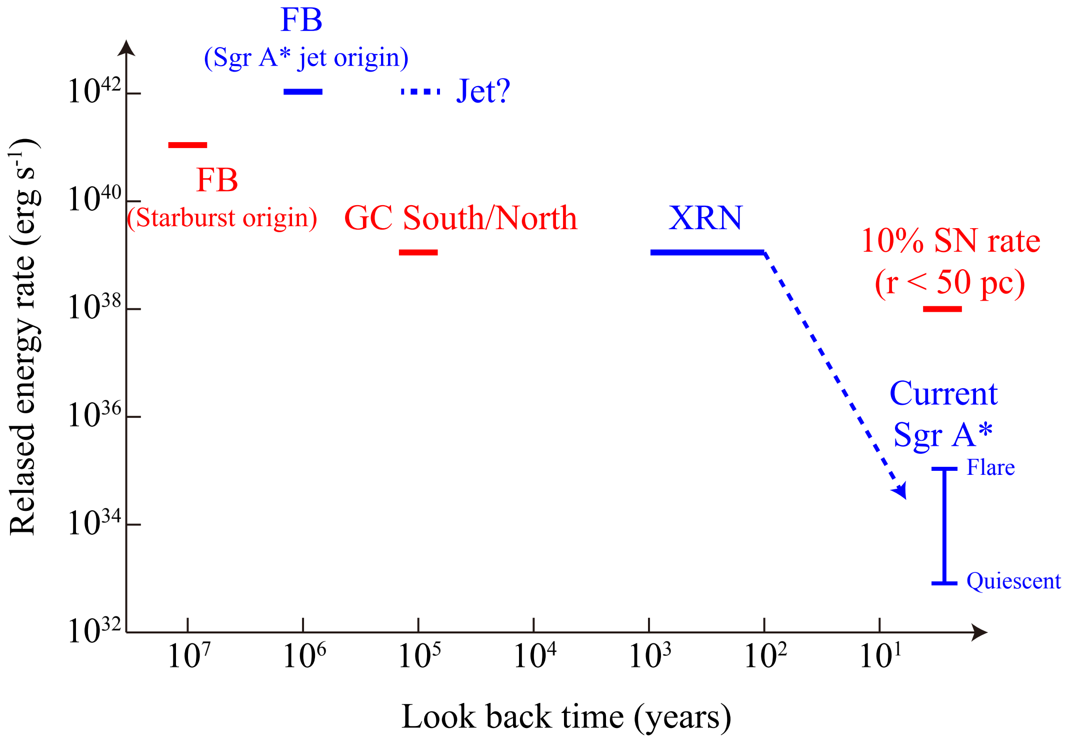

Figure 7.5. Schematic diagram of the revealed GC activities.

Chapter 8

Conclusion

In this thesis, we performed the survey of the south and north of the GC with *Suzaku*, and derived the following results.

- We found the large diffuse plasmas extending south and north perpendicular to the Galactic plane: GC South and GC North.
- GC South is a thin thermal plasma in a recombining phase, and is located at the GC distance. This is the first sample of an RP in the GC region. Fitting with a simple RP model gave us the plasma parameters of $kT_{\rm e} = 0.5$ keV, $kT_{\rm init} = 1.6$ keV, and $n_{\rm e}t = 5 \times 10^{11}$ s cm^{-3}. The size of GC South is about 200 pc. Then, the density, total thermal energy and mass are 0.1 cm^{-3}, 8×10^{51} erg and 3000 $M_\odot$, respectively.
- The electron temperature, density, and pressure of GC South smoothly decline with increasing the distance from the GC. The plasma near GC is in a CIE state while that of far side is in a recombining phase.
- GC North is also located at the GC distance, but its ionization state is different from that of GC South: an CIE plasma with $kT_{\rm e} = 0.8$ keV. The size of GC North is about 100 pc, and the its density is found to be 0.1 cm^{-3}. The total thermal energy and mass reach 3×10^{51} erg and 900 $M_\odot$, respectively. The dynamical timescale of the plasma is $\sim 10^5$ yr.
- Both GC South and North is not a single SNR or a superbubble. The mini-superwind due to nuclear starburst activity $\sim 10^5$ is a possible scenario. An RP in GC South is likely to be formed by the rapid electron cooling due to adiabatic expansion of the outflowing plasma.

Appendix A

Emission from a Thermal Plasma

A.1 Ionization State in a Plasma

A thermal plasma is one in which free-electrons distributed in the Maxwell-Boltzman distribution:

$$f(v_e) = 4\pi v_e^2 \left(\frac{m_e}{2\pi k T_\mathrm{e}}\right)^{3/2} \exp\left(-\frac{m_e v_e^2}{2kT_\mathrm{e}}\right), \tag{A.1}$$

where v_e, m_e, k, and T_e are electron mass, electron velocity, the Boltzman constant, and electron temperature, respectively. In this chapter, we focus on the plasma under the condition of high electron temperature ($kT_e \approx 1$ keV) and low electron density ($n_e < 1$ cm^{-3}), which is typical for the X-ray emitting plasma in the universe.

In a thermal plasma, collisional ionization occur when a free electron has a kinetic energy higher than binding energy and collides with an ion. It is also possible for a free electron to be captured by an ion into a bound state. This process is called recombination. Ionization degree of ions are deterred by the competition between ionization and recombination rates; the plasma becomes ionization equilibrium state when an ionization rate is equal to a recombination rate.

Since density of hot plasmas is low, non-ionization equilibrium state is usual in the universe. If the ionization degree is low compared with the electron temperature (under-ionized state), the plasma is dominated by an ionization process and is referred to as an "ionizing plasma". Such a plasma is widely observed in young SNRs, where the plasmas were recently shock-heated. In the opposite condition (over-ionized state), a recombining process is enhanced, and thus the plasma is referred to as an "recombining plasma". Such a condition can be seen in several mixed-morphology SNRs or photoionized plasmas around bright X-ray sources.

A.2 Radiation Process in a Thermal pPasma

Bremsstrahlung

When a free electron is scattered by an ion, photon is emitted, the so-called bremsstrahlung or free-free emission. An emissivity of bremsstrahlung produced by the interaction between thermal electrons and ion is represented by

$$\frac{dW}{dVdtd\nu} = \frac{32\pi e^6}{3m_e c^2}\left(\frac{2\pi}{3km_e}\right)^{1/2} T^{-1/2} Z^2 n_e n_i \exp\left(-\frac{h\nu}{kT_e}\right)\overline{g_{ff}}(T_e,\nu), \tag{A.2}$$

where c, Z, n_i, h, are $\overline{g_{ff}}$ the speed of light, the atomic number of a target ion, ion density, the Planck constant, and the velocity averaged Gaunt factor. For a typical thermal plasma emitting X-rays, the velocity averaged Gaunt factor is approximated as

$$\overline{g_{ff}}(T_e,\nu) = \left(\frac{3kT_e}{\pi h\nu}\right)^{-1/2}. \tag{A.3}$$

Taking the solar abundance of elements into account, hydrogen is the major element leading to the bremsstrahlung in a plasma.

Line emission

A bounded electron is excited by a collision of free electrons in a thermal plasma. Subsequently, de-excitation of the electron often leads to photon emission called line emission or bound-bound emission. In the low density regime, the so-called coronal limit, an excited electron immediately de-excited. Therefore, line flux is determined by a collisional excitation rate and is proportional to $n_e n_i$.

Since flux of the bremsstrahlung is almost proportional to $n_e n_H$, we can derive the relative abundance of a heavy element to hydrogen (n_i/n_H) from the ratio of the line flux and the bremsstrahlung flux. Line emission is useful for plasma diagnostics. We are also able to obtain the ion population in an element by using the flux ratio of two lines which come from an identical element but different ionization states.

Radiative recombination continuum

Photon emission associated with recombination is called radiative recombination continuum or free-bound emission. The energy of the photon equals the kinetic energy of the electron plus the binding energy where the electron recombines. Therefore, the major feature of RRC spectrum is a edge, which corresponds to the binding energy. The emissivity of the RRC with a thermal electron distribution is given by

$$\frac{dW}{dVdtdE} = 4n_e n_i E \left(\frac{E-I}{kT_e}\right)\left(\frac{1}{2\pi m_e kT_e}\right)^{1/2} \exp\left(-\frac{E-I}{kT_e}\right)\sigma_n^{\mathrm{rec}}, \tag{A.4}$$

where E, I, and σ_n^{rec} are emitted photon energy, binding energy, and the cross section of recombination. According to Nakayama & Masai (2001), σ_n^{rec} for an H-like ion is approximated as

$$\sigma_n^{\mathrm{rec}} \propto \frac{1}{n^3}\left(\frac{3kT_e}{2I} + \frac{1}{n^2}\right)^{-1} \tag{A.5}$$

Therefore, recombination to the lowest levels is the major process. If a free electron recombines to excited state, de-excitation of the electron subsequently occurs. The line emission emitted by this process is especially called the cascade line.

A.3 Spectrum of a Recombining Plasma

In an ionization-equilibrium plasma with high electron temperature ($kT_e > 0.1$ keV), RRC is weaker than the bremsstrahlung, and thus there is no apparent RRC features in an X-ray spectrum. However, in a recombining plasma, a spectrum shows strong RRC features since the majority of the ions are recombining (Figure A.1).

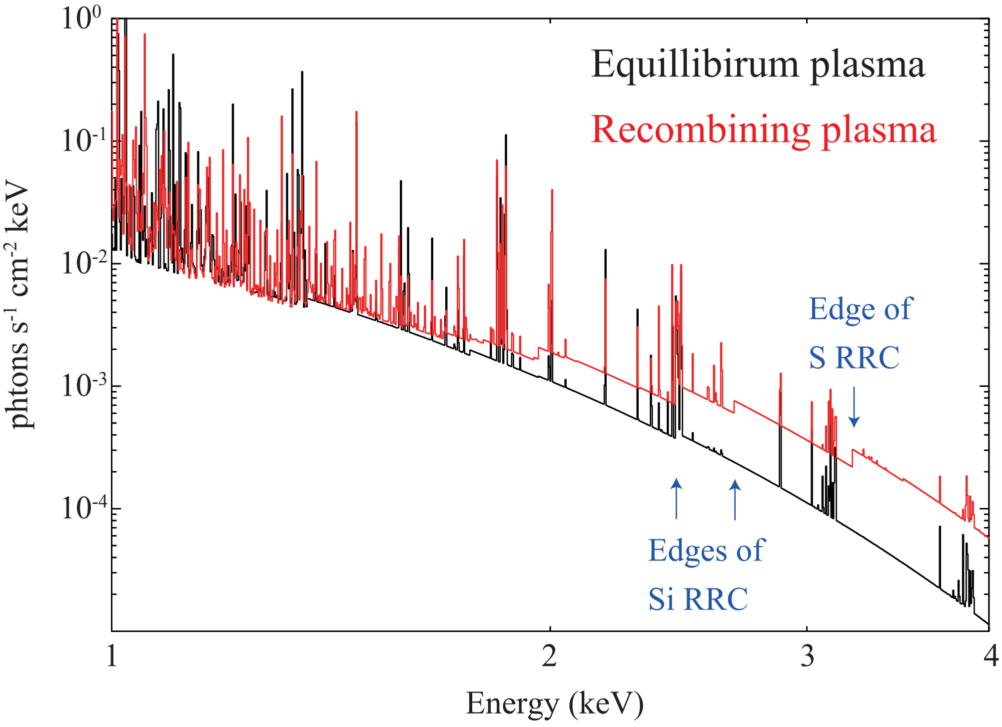

Figure A.1. Spectrum models of thermal plasmas with $kT_e = 0.5$ keV. The ionization equilibrium and recombining plasmas are shown in black and red, respectively.

Bibliography

Anders, E., & Grevesse, N. 1989, Geochim. Cosmochim. Acta, 53, 197

Audard, M., Behar, E., Güdel, M., et al. 2001, A&A, 365, L329

Baganoff, F. K., Maeda, Y., Morris, M., et al. 2003, ApJ, 591, 891

Balick, B., & Brown, R. L. 1974, ApJ, 194, 265

Bower, G. C., Goss, W. M., Falcke, H., Backer, D. C., & Lithwick, Y. 2006, ApJ, 648, L127

Brickhouse, N. S., Dupree, A. K., Edgar, R. J., et al. 2000, ApJ, 530, 387

Brown, R. L. 1982, ApJ, 262, 110

Brown, R. L., & Lo, K. Y. 1982, ApJ, 253, 108

Burke, B. E., Gregory, J. A., Loomis, A. H., et al. 2004, IEEE Transactions on Nuclear Science, 51, 2322

Carretti, E., Crocker, R. M., Staveley-Smith, L., et al. 2013, Nature, 493, 66

Coker, R., Melia, F., & Falcke, H. 1999, ApJ, 523, 642

Cotera, A., Morris, M., Ghez, A. M., et al. 1999, in Astronomical Society of the Pacific Conference Series, Vol. 186, The Central Parsecs of the Galaxy, ed. H. Falcke, A. Cotera, W. J. Duschl, F. Melia, & M. J. Rieke, 240

Crocker, R. M., Jones, D. I., Melia, F., Ott, J., & Protheroe, R. J. 2010, Nature, 463, 65

Dame, T. M. 1993, in American Institute of Physics Conference Series, Vol. 278, Back to the Galaxy, ed. S. S. Holt & F. Verter, 267–278

Dame, T. M., Hartmann, D., & Thaddeus, P. 2001, ApJ, 547, 792

Doeleman, S. S., Weintroub, J., Rogers, A. E. E., et al. 2008, Nature, 455, 78

Duschl, W. J., & Lesch, H. 1994, A&A, 286, 431

Enokiya, R., Torii, K., Schultheis, M., et al. 2013, ArXiv e-prints

Falcke, H., Goss, W. M., Matsuo, H., et al. 1998, ApJ, 499, 731

Ferrière, K., Gillard, W., & Jean, P. 2007, A&A, 467, 611

Figer, D. F., Rich, R. M., Kim, S. S., Morris, M., & Serabyn, E. 2004, ApJ, 601, 319

Garmire, G. P., Bautz, M. W., Ford, P. G., Nousek, J. A., & Ricker, Jr., G. R. 2003, in Society of Photo-Optical Instrumentation Engineers (SPIE) Conference Series, Vol. 4851, Society of Photo-Optical Instrumentation Engineers (SPIE) Conference Series, 28–44

Gaustad, J. E., McCullough, P. R., Rosing, W., & Van Buren, D. 2001, PASP, 113, 1326

Genzel, R., Eisenhauer, F., & Gillessen, S. 2010, Reviews of Modern Physics, 82, 3121

Ghez, A. M., Salim, S., Hornstein, S. D., et al. 2005, ApJ, 620, 744

Ghez, A. M., Wright, S. A., Matthews, K., et al. 2004, ApJ, 601, L159

Ghez, A. M., Salim, S., Weinberg, N. N., et al. 2008, ApJ, 689, 1044

Gonzalez, O. A., Rejkuba, M., Zoccali, M., et al. 2012, A&A, 543, A13

Gu, M. F., Chen, H., Brown, G. V., Beiersdorfer, P., & Kahn, S. M. 2007, ApJ, 670, 1504

Güver, T., & Özel, F. 2009, MNRAS, 400, 2050

Haffner, L. M., Dettmar, R.-J., Beckman, J. E., et al. 2009, Reviews of Modern Physics, 81, 969

Immer, K., Schuller, F., Omont, A., & Menten, K. M. 2012, A&A, 537, A121

Inui, T., Koyama, K., Matsumoto, H., & Tsuru, T. G. 2009, PASJ, 61, S241

Kaastra, J. S., Mewe, R., & Nieuwenhuijzen, H. 1996, in UV and X-ray Spectroscopy of Astrophysical and Laboratory Plasmas, ed. K. Yamashita & T. Watanabe, 411–414

Kallman, T., & Bautista, M. 2001, ApJS, 133, 221

Kataoka, J., Tahara, M., Totani, T., et al. 2013, ArXiv e-prints

Koyama, K., Awaki, H., Kunieda, H., Takano, S., & Tawara, Y. 1989, Nature, 339, 603

Koyama, K., Maeda, Y., Sonobe, T., et al. 1996, PASJ, 48, 249

Koyama, K., Makishima, K., Tanaka, Y., & Tsunemi, H. 1986, PASJ, 38, 121

Koyama, K., Uchiyama, H., Hyodo, Y., et al. 2007a, PASJ, 59, 237

Koyama, K., Hyodo, Y., Inui, T., et al. 2007b, PASJ, 59, S245

Koyama, K., Tsunemi, H., Dotani, T., et al. 2007c, PASJ, 59, S23

Krabbe, A., Genzel, R., Drapatz, S., & Rotaciuc, V. 1991, ApJ, 382, L19

Krabbe, A., Genzel, R., Eckart, A., et al. 1995, ApJ, 447, L95

Kushino, A., Ishisaki, Y., Morita, U., et al. 2002, PASJ, 54, 327

LaRosa, T. N., Brogan, C. L., Shore, S. N., et al. 2005, ApJ, 626, L23

LaRosa, T. N., Kassim, N. E., Lazio, T. J. W., & Hyman, S. D. 2000, AJ, 119, 207

Longmore, S. N., Bally, J., Testi, L., et al. 2013, MNRAS, 429, 987

Lynden-Bell, D. 1969, Nature, 223, 690

Lynden-Bell, D., & Rees, M. J. 1971, MNRAS, 152, 461

Markoff, S. 2010, Proceedings of the National Academy of Science, 107, 7196

Martins, F., Genzel, R., Hillier, D. J., et al. 2007, A&A, 468, 233

Melia, F., & Falcke, H. 2001, ARA&A, 39, 309

Mitsuda, K., Bautz, M., Inoue, H., et al. 2007, PASJ, 59, S1

Mori, H., Hyodo, Y., Tsuru, T. G., Nobukawa, M., & Koyama, K. 2009, PASJ, 61, 687

Mori, H., Iizuka, R., Shibata, R., et al. 2005, PASJ, 57, 245

Morris, M. 2007, ArXiv Astrophysics e-prints

Morris, M., & Serabyn, E. 1996, ARA&A, 34, 645

Muno, M. P., Baganoff, F. K., Bautz, M. W., et al. 2004, ApJ, 613, 326

Najarro, F., Hillier, D. J., Kudritzki, R. P., et al. 1994, A&A, 285, 573

Nakashima, S., Nobukawa, M., Tsuru, T. G., Koyama, K., & Uchiyama, H. 2010, PASJ, 62, 971

Nakayama, M., & Masai, K. 2001, A&A, 375, 328

Narayan, R., & McClintock, J. E. 2008, New A Rev., 51, 733

Narayan, R., Yi, I., & Mahadevan, R. 1995, Nature, 374, 623

Neilsen, J., Nowak, M. A., Gammie, C., et al. 2013, ApJ, 774, 42

Nishiyama, S., Hatano, H., Tamura, M., et al. 2010, ApJ, 722, L23

Nishiyama, S., Yasui, K., Nagata, T., et al. 2013, ApJ, 769, L28

Nobukawa, M., Koyama, K., Tsuru, T. G., Ryu, S. G., & Tatischeff, V. 2010, PASJ, 62, 423

Nobukawa, M., Ryu, S. G., Tsuru, T. G., & Koyama, K. 2011, ApJ, 739, L52

Nobukawa, M., Tsuru, T. G., Takikawa, Y., et al. 2008, PASJ, 60, 191

Novak, G., Chuss, D. T., Renbarger, T., et al. 2003, ApJ, 583, L83

Nowak, M. A., Neilsen, J., Markoff, S. B., et al. 2012, ApJ, 759, 95

Ohnishi, T., Koyama, K., Tsuru, T. G., et al. 2011, PASJ, 63, 527

Oka, T., Hasegawa, T., Hayashi, M., Handa, T., & Sakamoto, S. 1998, ApJ, 493, 730

Pedlar, A., Anantharamaiah, K. R., Ekers, R. D., et al. 1989, ApJ, 342, 769

Porquet, D., Predehl, P., Aschenbach, B., et al. 2003, A&A, 407, L17

Predehl, P., & Truemper, J. 1994, A&A, 290, L29

Revnivtsev, M., Sazonov, S., Churazov, E., et al. 2009, Nature, 458, 1142

Robitaille, T. P., & Whitney, B. A. 2010, ApJ, 710, L11

Rohlfs, K., & Kreitschmann, J. 1987, A&A, 178, 95

Roy, S. 2013, ApJ, 773, 67

Ruffert, M., & Melia, F. 1994, A&A, 288, L29

Ryu, S. G. 2013, PhD thesis, Kyoto University

Ryu, S. G., Koyama, K., Nobukawa, M., Fukuoka, R., & Tsuru, T. G. 2009, PASJ, 61, 751

Ryu, S. G., Nobukawa, M., Nakashima, S., et al. 2013, PASJ, 65, 33

Sakano, M., Koyama, K., Murakami, H., Maeda, Y., & Yamauchi, S. 2002, ApJS, 138, 19

Sawada, M., & Koyama, K. 2012, PASJ, 64, 81

Sawada, M., Nakashima, S., Nobukawa, M., Uchiyama, H., & XIS Team. 2012, in American Institute of Physics Conference Series, Vol. 1427, American Institute of Physics Conference Series, ed. R. Petre, K. Mitsuda, & L. Angelini, 245–246

Sawada, M., Tsujimoto, M., Koyama, K., et al. 2009, PASJ, 61, 209

Schödel, R., Ott, T., Genzel, R., et al. 2002, Nature, 419, 694

Serabyn, E., Carlstrom, J., Lay, O., et al. 1997, ApJ, 490, L77

Serlemitsos, P. J., Jalota, L., Soong, Y., et al. 1995, PASJ, 47, 105

Serlemitsos, P. J., Soong, Y., Chan, K.-W., et al. 2007, PASJ, 59, S9

Shimizu, T., Masai, K., & Koyama, K. 2012, PASJ, 64, 24

Snowden, S. L., Egger, R., Freyberg, M. J., et al. 1997, ApJ, 485, 125

Strickland, D. K., Heckman, T. M., Weaver, K. A., & Dahlem, M. 2000, AJ, 120, 2965

Su, M., Slatyer, T. R., & Finkbeiner, D. P. 2010, ApJ, 724, 1044

Takahashi, T., Abe, K., Endo, M., et al. 2007, PASJ, 59, 35

Tanaka, Y., Inoue, H., & Holt, S. S. 1994, PASJ, 46, L37

Tanaka, Y., Koyama, K., Maeda, Y., & Sonobe, T. 2000, PASJ, 52, L25

Toor, A., & Seward, F. D. 1974, AJ, 79, 995

Tsuboi, M., Handa, T., & Ukita, N. 1999, ApJS, 120, 1

Tsuru, T. G., Nobukawa, M., Nakajima, H., et al. 2009, PASJ, 61, 219

Turner, M. J. L., Abbey, A., Arnaud, M., et al. 2001, AA, 365, L27

Uchida, H., Koyama, K., Yamaguchi, H., et al. 2012, PASJ, 64, 141

Uchiyama, H., Nobukawa, M., Tsuru, T., Koyama, K., & Matsumoto, H. 2011, PASJ, 63, S903

Uchiyama, H., Nobukawa, M., Tsuru, T. G., & Koyama, K. 2013, PASJ, 65, 19

Uchiyama, H., Ozawa, M., Matsumoto, H., et al. 2009, PASJ, 61, S9

Uchiyama, Y., Maeda, Y., Ebara, M., et al. 2008, PASJ, 60, 35 van den Berg, M., Hong, J. S., & Grindlay, J. E. 2009, ApJ, 700, 1702

Wang, Q. D. 2002, arXiv:astro-ph/0202317

Warwick, R. S., Turner, M. J. L., Watson, M. G., & Willingale, R. 1985, Nature, 317, 218

Watson, M. G., Willingale, R., Hertz, P., & Grindlay, J. E. 1981, ApJ, 250, 142

Yamashita, A., Dotani, T., Bautz, M., et al. 1997, IEEE Transactions on Nuclear Science, 44, 847

Yamauchi, S., Nobukawa, M., Koyama, K., & Yonemori, M. 2013, PASJ, 65, 6

Yasuda, A., Nakagawa, T., Spaans, M., Okada, Y., & Kaneda, H. 2008, A&A, 480, 157

Yuan, F., Quataert, E., & Narayan, R. 2003, ApJ, 598, 301

Yusef-Zadeh, F., Hewitt, J. W., & Cotton, W. 2004, ApJS, 155, 421

Yusef-Zadeh, F., & Morris, M. 1987, AJ, 94, 1178

Yusef-Zadeh, F., Hewitt, J. W., Arendt, R. G., et al. 2009, ApJ, 702, 178

Zhou, X., Miceli, M., Bocchino, F., Orlando, S., & Chen, Y. 2011, MNRAS, 415, 244

Zubovas, K., King, A. R., & Nayakshin, S. 2011, MNRAS, 415, L21

Acknownledgments

My cordial gratitude goes to my supervisors Prof. Takeshi Go Tsuru and Prof. Katsuji Koyama who gave me the precious opportunity to conduct this interesting study and has been encouraging me throughout my graduate course.

I am also appreciate to Dr. Masayoshi Nobukawa, Dr. Takaaki Tanaka, Dr. Hiroyuki Uchida, and Dr. Hideki Uchiyama who gave me a number of invaluable comments to my study, including English proofreading.

I would like to thank the members of the Cosmic-ray laboratory in Kyoto University for enjoying the academic life together.

Finally, I express supreme thanks to all of my family and friends for their warm support and encouragements.